

**Two-Probe Techniques to Measure
Wavenumber-Frequency Spectrum of VTF
Plasma**

by

Ryan James Riddolls

Submitted to the Department of Electrical Engineering and
Computer Science

in partial fulfillment of the requirements for the degree of
Master of Engineering in Electrical Engineering and Computer
Science

at the

MASSACHUSETTS INSTITUTE OF TECHNOLOGY

February 1999

© Ryan James Riddolls, MCMXCIX. All rights reserved.

The author hereby grants to MIT permission to reproduce and
distribute publicly paper and electronic copies of this thesis and to
grant others the right to do so.

ENG

Author

Department of Electrical Engineering and Computer Science

February 3, 1999

Certified by

ang Lee

ervisor

Accepted by

. Smith

Chairman, Department Committee on Graduate Theses

Two-Probe Techniques to Measure Wavenumber-Frequency Spectrum of VTF Plasma

by

Ryan James Riddolls

Submitted to the Department of Electrical Engineering and Computer Science
on February 3, 1999, in partial fulfillment of the
requirements for the degree of
Master of Engineering in Electrical Engineering and Computer Science

Abstract

Two-probe techniques have been implemented to measure the wavenumber-frequency spectrum of plasma turbulence in a laboratory plasma. The turbulence is driven by injected waves from an in-plasma crossed-dipole antenna. The methods find application in examining a number of theories relevant to the generation of lower hybrid waves in the earth's ionosphere. These waves play a key role in the bandwidth expansion of VLF waves traversing the ionosphere and in the source mechanism producing frequency-upshifted plasma lines (HFPLs).

Thesis Supervisor: Prof. Min-Chang Lee

Title: Leader, Ionospheric Plasma Research Group, Plasma Science and Fusion Center

Acknowledgments

I am grateful to have had the opportunity to pursue graduate studies at MIT. Prof. Min-Chang Lee has assumed a central role in my work of the last five years, first as my UROP supervisor and later as a thesis supervisor. He has been generous in his personal commitment to my progress, offering advice on every facet of life in an effort to further my professional development. He has strived to set an example of perseverance and diligence from which I have certainly learned a great deal. I extend my heartfelt thanks to him. It is most fortunate that I will be able to continue on with work towards the Ph.D. degree under his supervision.

I am indebted to Nathan Dalrymple for letting me use his low-pass filters and the programs he has written for controlling the high-speed digitizers and crunching the phase-lag data. It saved me enough time to allow me to include the phase-lag measurements in this thesis.

Contents

1	Background and Motivation	9
1.1	Plasma waves	9
1.1.1	Elementary description	9
1.1.2	The Appleton-Hartree relation	12
1.1.3	The electrostatic approximation	14
1.2	Whistler interactions with the ionosphere	17
1.3	Role of lower hybrid waves in heating experiments	24
1.3.1	The Arecibo Radar	24
1.3.2	Heating experiments	26
2	Experimental Apparatus	34
2.1	Overview of facility	34
2.1.1	Vessel and vacuum system	34
2.1.2	Magnet system	37
2.1.3	Plasma sources	38
2.1.4	Diagnostics	43
2.1.5	Data acquisition and control	43
2.2	Wave launcher	44
2.2.1	Antenna design	44
2.2.2	Hardware Construction	46
2.2.3	Electrical connections	54
2.3	Diagnostic	67
2.3.1	Probe characteristic	68

2.3.2	Decisions on probe deployment	72
2.3.3	Hardware construction	73
3	Diagnostic Measurements	88
3.1	Single-probe measurements	90
3.1.1	Excitation of modes at the pump wave frequency	90
3.1.2	Excitation of modes at zero-frequency	93
3.2	Double-probe measurements	93
3.2.1	Method of interferometry	98
3.2.2	Statistical phase-lag measurements	104
4	Conclusions	113
A	Source mechanism of field-aligned irregularities	116
A.1	Steady-state drifts	116
A.1.1	Ion Pedersen drift	116
A.1.2	Field-aligned current	117
A.1.3	Gravity and equivalent gravity drifts	118
A.2	Consequences of a plasma density gradient	118
A.2.1	Analysis of instability	118
B	Whistler Ducting	126
B.1	Theory	126
B.2	Experimental observations	130

List of Figures

1-1	Dispersion relation for high frequency modes propagating at small angles to the magnetic field. X and O denote extraordinary and ordinary mode.	13
1-2	The electrostatic dispersion relation.	16
1-3	The Arecibo Radar Telescope.	25
1-4	The wavenumber and frequency matching relations for Langmuir wave scattering Arecibo. “1” represents the source Langmuir wave, “0”, the frequency-upshifted Langmuir wave, “2”, the frequency-downshifted Langmuir wave, and “3”, the lower hybrid wave.	29
1-5	Spectrum of O-mode pump wave-excited Langmuir waves as detected by the Arecibo radar.	30
1-6	Spectrum of O-mode pump wave-excited Langmuir waves in the VTF machine.	31
1-7	Spectrum of lower hybrid waves seen in the VTF machine.	32
2-1	The VTF machine.	35
2-2	An electron-emitting filament. This is an early version featuring carbon backshields. The machine-mounted emitters have stainless steel backshields.	39
2-3	Schematic of antenna (not to scale).	48
2-4	Schematic of homemade feedthroughs (not to scale).	51
2-5	The crossed-dipole antenna, as seen from inside the chamber.	55
2-6	The external feedthroughs for the machine-mounted antenna.	56

2-7	Crude realization of a network analyzer. “S12” boxes are power splitters, “LIR” boxes are mixers, and all resistors are 50 Ω	58
2-8	A method for measuring the voltage standing wave.	59
2-9	Magnitude of gamma of antenna A as a function of toroidal field strength.	61
2-10	Magnitude of gamma of antenna B as a function of toroidal field strength.	62
2-11	Voltage standing wave pattern in cable.	64
2-12	Magnitude of gamma of parallel combination of antennas A and B, as a function of toroidal field strength.	66
2-13	Power received at high and low input impedance. Third trace on right shows low impedance trace corrected for plasma impedance effects. .	71
2-14	Schematic of top probe.	75
2-15	Top probe mounted on the machine.	80
2-16	Schematic of side probe.	81
2-17	The rotating arm.	85
2-18	The side probe.	86
2-19	Deployment of the two probe tips.	87
3-1	Damage to side probe ceramic after arc.	89
3-2	Spectrum of plasma voltage fluctuations around the pump wave frequency.	91
3-3	Spectrum of plasma voltage fluctuations around the pump wave frequency in the absence of the pump.	92
3-4	Spectrum of low frequency plasma voltage fluctuations with and without the presence of the pump wave.	94
3-5	Time series of voltage fluctuations during RF pulsing.	95
3-6	Interferometer setup in the VTF machine. “SIQ” is a power splitter featuring 0 and 90 degree outputs.	99
3-7	Pump wave patterns. On the left, the probes scan for 14 seconds. On the right, the scanning is stopped after 6 seconds.	102

3-8	Comparison of low frequency power spectra for moving and stationary probes.	103
3-9	Phase lag measurement setup.	104
3-10	Low frequency spectrum, probes spaced perpendicular to the field, in presence of pump wave. Frequency axis is true frequency.	106
3-11	Low frequency spectrum, probes spaced perpendicular to the field, with no pump wave. Frequency axis is true frequency.	107
3-12	Low frequency spectrum, probes spaced parallel to the field, in presence of pump wave. Frequency axis is true frequency.	108
3-13	Low frequency spectrum, probes spaced parallel to the field, with no pump wave. Frequency axis is true frequency.	109
3-14	Spectrum around pump wave, probes spaced perpendicular to the field. Frequency axis 0-1 MHz corresponds to frequency range 35.89 MHz to 36.89 MHz before mixing, so that pump is at 250 KHz. Graph has been turned to show downshifted spectrum.	110
3-15	Spectrum around pump wave, probes spaced parallel to the field. Frequency axis 0-1 MHz corresponds to frequency range 35.89 MHz to 36.89 MHz before mixing, so that pump is at 250 KHz. Graph has been turned to show downshifted spectrum.	111
A-1	Instability Mechanism	119
B-1	Region where one solution exists	128
B-2	Probe observations of whistler wave cutoff in the VTF machine. . . .	131

Chapter 1

Background and Motivation

1.1 Plasma waves

1.1.1 Elementary description

Consider a cold, non-drifting, homogeneous plasma in a uniform magnetic field. Maxwell's equations and the fluid equations lead to an appropriate description of the modes of this medium.

Maxwell's equations lead to a wave equation:

$$\nabla \times (\nabla \times \mathbf{E}) + \frac{1}{c^2} \frac{\partial^2 \mathbf{E}}{\partial t^2} + \mu_0 \frac{\partial \mathbf{J}}{\partial t} = -\mu_0 \frac{\partial \mathbf{J}_{ext}}{\partial t} \quad (1.1)$$

where \mathbf{J}_{ext} is the current due to sources external to the plasma.

The fluid equations allow one to express the current \mathbf{J} in terms of an electric field \mathbf{E} , allowing us to solve the wave equation. The *linearized* fluid equations allow us to go one step further—we can express the vector current as a linear transformation (i.e., a matrix multiplication) of the electric field vector. This assumption requires that the current and electric field be of small amplitude, which we will denote with a “1” subscript.

Since linear operations commute with the operation of finding the real part of

some field quantity \mathbf{A}

$$\Re[L(\mathbf{A}(\mathbf{r}, t))] = L[\Re(\mathbf{A}(\mathbf{r}, t))] \quad (1.2)$$

where L is a linear operation, it is useful to express all quantities in terms of their Fourier components, so that $\mathbf{A}(\mathbf{r}, t) = \Re[\mathbf{A}(\mathbf{k}, \omega) \exp(i(\mathbf{k} \cdot \mathbf{r} - \omega t))]$. Under these assumptions, the linearized current \mathbf{J}_1 can be expressed as

$$\mathbf{J}_1 = -i\omega\epsilon_0\boldsymbol{\chi} \cdot \mathbf{E}_1 \quad (1.3)$$

where $\boldsymbol{\chi}$ is the susceptibility tensor. For convenience, we set the magnetic field in the direction of $\hat{\mathbf{z}}$, so that $\boldsymbol{\chi}$ takes the following form:

$$\boldsymbol{\chi} = \begin{pmatrix} \chi_{\perp} & -i\chi_{\times} & 0 \\ i\chi_{\times} & \chi_{\perp} & 0 \\ 0 & 0 & \chi_{\parallel} \end{pmatrix} \quad (1.4)$$

where the elements have contributions from both the electron and ion species:

$$\chi_{\perp} = - \sum_{s=e,i} \frac{\omega_{ps}^2}{(\omega^2 - \Omega_s^2)} \quad (1.5)$$

$$\chi_{\times} = \sum_{s=e,i} \frac{\Omega_s}{\omega} \frac{\omega_{ps}^2}{(\omega^2 - \Omega_s^2)} \quad (1.6)$$

$$\chi_{\parallel} = - \sum_{s=e,i} \frac{\omega_{ps}^2}{\omega^2}. \quad (1.7)$$

Here, ω_{ps} is the plasma frequency of a species, defined as $(e^2 n_s / \epsilon_0 m_s)^{1/2}$, where n_s is the density of the species and m_s is its mass. Ω_s is the cyclotron frequency, defined as $(q_s B_0 / m_s)$, where q_s is the signed species charge and B_0 is the background magnetic field strength. Note that Ω_e is a negative quantity. We will use the symbol ω_{cs} when we want to denote the unsigned cyclotron frequency of a species.

The wave equation can then be written

$$\mathbf{n} \times (\mathbf{n} \times \mathbf{E}_1) + \mathbf{K} \cdot \mathbf{E}_1 = (\mathbf{E}_{ext})_1 \quad (1.8)$$

where \mathbf{n} is a complex index of refraction vector,

$$\mathbf{n} = \frac{c\mathbf{k}}{\omega}, \quad (1.9)$$

\mathbf{K} is the permittivity tensor,

$$\mathbf{K} = \mathbf{I} + \boldsymbol{\chi}, \quad (1.10)$$

and $(\mathbf{E}_{ext})_1$ is an effective externally applied electric field,

$$(\mathbf{E}_{ext})_1 = \frac{(\mathbf{J}_{ext})_1}{i\omega\epsilon_0}. \quad (1.11)$$

We can solve for the electric field \mathbf{E}_1 by rewriting the wave equation as

$$\mathbf{D} \cdot \mathbf{E}_1 = (\mathbf{E}_{ext})_1 \quad (1.12)$$

where

$$\mathbf{D} \equiv \mathbf{nn} - n^2\mathbf{I} + \mathbf{K}. \quad (1.13)$$

The solution of the linear set of equations (1.12) consists of a particular solution plus the general homogeneous solution. A particular solution (i.e., the *driven fields*) is found by matrix inversion

$$\mathbf{E}_1 = \frac{\mathbf{D}_{adj} \cdot (\mathbf{E}_{ext})_1}{\det \mathbf{D}} \quad (1.14)$$

where \mathbf{D}_{adj} is the adjoint of \mathbf{D} . The homogeneous solution, or the *natural modes*, are the non-zero solutions of \mathbf{E}_1 when $(\mathbf{E}_{ext})_1$ is zero. We recall that these can exist only when the determinant of \mathbf{D} is zero. Therefore the dispersion relation is

$$\det \mathbf{D} = 0 \quad (1.15)$$

This expression can be satisfied by numerous families of frequencies and wavenumbers. We will deal with two particularly useful approximate solutions: the Appleton-Hartree relation and the electrostatic approximation.

1.1.2 The Appleton-Hartree relation

First, we will assume that \mathbf{n} lies in the x-z plane at an angle θ with respect to $\hat{\mathbf{z}}$. The dyad \mathbf{nn} is then

$$\mathbf{nn} = \begin{pmatrix} n^2 \sin^2 \theta & 0 & n^2 \sin \theta \cos \theta \\ 0 & 0 & 0 \\ n^2 \sin \theta \cos \theta & 0 & n^2 \cos^2 \theta \end{pmatrix}. \quad (1.16)$$

The Appleton-Hartree relation follows from neglecting slow time-scale ion dynamics. The elements of the susceptibility tensor are approximated as

$$\chi_{\perp} \approx -\frac{\omega_{pe}^2}{(\omega^2 - \Omega_e^2)} \quad (1.17)$$

$$\chi_{\times} \approx \frac{\Omega_e}{\omega} \frac{\omega_{pe}^2}{(\omega^2 - \Omega_e^2)} \quad (1.18)$$

$$\chi_{\parallel} \approx -\frac{\omega_{pe}^2}{\omega^2}. \quad (1.19)$$

Moving to unsigned cyclotron frequencies, the solution of (1.15) is simple:

$$n^2 = 1 - \frac{2\omega_{pe}^2(\omega^2 - \omega_{pe}^2)/w^2}{2(\omega^2 - \omega_{pe}^2) - \omega_{ce}^2 \sin^2 \theta \pm \omega_{ce}[\omega_{ce}^2 \sin^4 \theta + 4\omega^{-2}(\omega^2 - \omega_{pe}^2)^2 \cos^2 \theta]^{1/2}}, \quad (1.20)$$

which is the Appleton-Hartree relation. This expression is particularly suited to ray-tracing in inhomogeneous media because both \mathbf{k} and the group velocity can be easily computed locally from the relation as a wave packet propagates through the medium.

The Appleton-Hartree relation is useful for describing many of the electromagnetic waves that are encountered in the ionosphere and in laboratory experiments. Particular attention should be paid to the \pm sign in the denominator of the expression, as it alerts us that propagation is possible in two separate modes—the so-called ordinary and extraordinary modes.

We will have particular interest in the case when the waves are propagating nearly along the magnetic field (i.e., θ is small). In this case, the following approximations

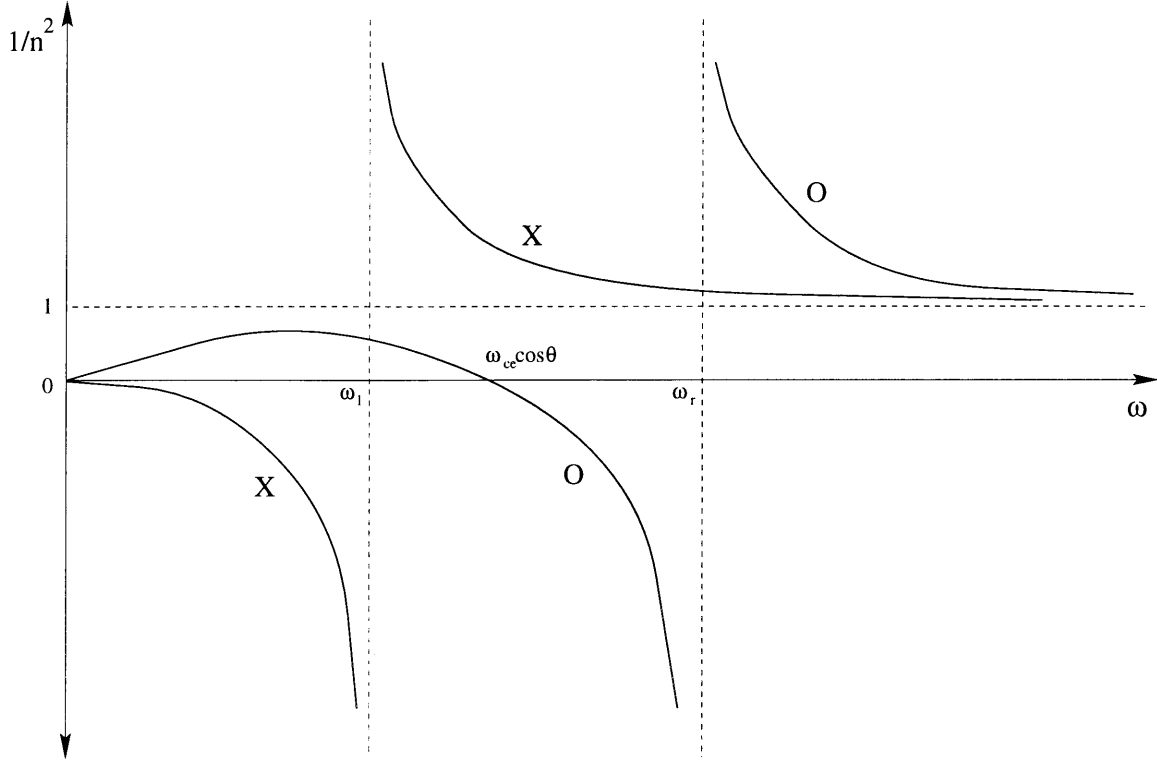


Figure 1-1: Dispersion relation for high frequency modes propagating at small angles to the magnetic field. X and O denote extraordinary and ordinary mode.

can be made:

$$\omega_{ce}^2 \sin^4 \theta \ll 4\omega^{-2}(\omega^2 - \omega_{pe}^2)^2 \cos^2 \theta \quad (1.21)$$

$$\omega_{ce}^2 \sin^2 \theta \ll |2(\omega^2 - \omega_{pe}^2)|, \quad (1.22)$$

leaving us with

$$n^2 = 1 - \frac{\omega_{pe}^2}{\omega(\omega \mp \omega_{ce} \cos \theta)}. \quad (1.23)$$

This relation is plotted in figure 1-1 as a function of ω .

Note that at low frequencies ($\omega \ll \omega_{ce}, \omega_{pe}$), propagation is only possible in the ordinary mode, corresponding to a negative sign in (1.23). This mode is often excited in the natural ionosphere as broadband emissions associated with lightning strokes. The dispersion of these waves is such that the group delays associated with higher frequencies is smaller than those associated with lower frequencies. As a result, if these signals are received by an observer distant from the source of the tone bursts, and modulated down to audio range, descending “whistle-like” tones can be heard.

For this reason, these bursts are known as *whistlers*. They are suspected as an element in ionospheric wave interactions, which will be discussed in section 1.2 of this chapter.

1.1.3 The electrostatic approximation

Let us decompose \mathbf{E}_1 into components perpendicular and parallel to \mathbf{k} . We will call these the transverse and longitudinal components of \mathbf{E}_1 , respectively:

$$\mathbf{E}_1 = \mathbf{E}_T + \mathbf{E}_L. \quad (1.24)$$

With this definition, the wave equation becomes

$$(n^2\mathbf{I} - \mathbf{K}) \cdot \mathbf{E}_T - \mathbf{K} \cdot \mathbf{E}_L = 0 \quad (1.25)$$

If we approximate that the square of the index of refraction is much larger than any of the elements of the permittivity tensor:

$$n^2 \gg |\mathbf{K}_{ij}|, \quad (1.26)$$

then the wave equation becomes

$$n^2\mathbf{E}_T - \mathbf{K} \cdot \mathbf{E}_L \approx 0. \quad (1.27)$$

Taking the dot-product of this equation with $\hat{\mathbf{n}} \equiv \mathbf{n}/n$ gives us a scalar wave equation

$$\hat{\mathbf{n}} \cdot \mathbf{K} \cdot \hat{\mathbf{n}} E_L = 0. \quad (1.28)$$

In order for $E_L \neq 0$ we see that the dispersion relation must be

$$\hat{\mathbf{n}} \cdot \mathbf{K} \cdot \hat{\mathbf{n}} = 0. \quad (1.29)$$

We assume that \mathbf{k} has x and z components, so the dispersion relation can be written as

$$\tan^2 \theta = -\frac{1 + \chi_{\parallel}}{1 + \chi_{\perp}} \quad (1.30)$$

If we allow the approximation $\omega_{pe}^2 \Omega_i^2 \ll \omega_{pi}^2 \Omega_e^2$, then upon substitution of the susceptibility elements, we arrive at

$$\cot^2 \theta = -\frac{\omega^2(\omega^2 - \omega_{lh}^2)(\omega^2 - \omega_{uh}^2)}{(\omega^2 - \Omega_i^2)(\omega^2 - \Omega_e^2)(\omega^2 - \omega_{pe}^2)} \quad (1.31)$$

where ω_{lh} and ω_{uh} are the lower and upper hybrid frequencies:

$$\omega_{lh}^2 = \frac{\omega_{pi}^2}{1 + \omega_{pe}^2/\Omega_e^2} \quad (1.32)$$

$$\omega_{uh}^2 = \omega_{pe}^2 + \Omega_e^2. \quad (1.33)$$

A plot of this relation is in figure 1-2 for the case $\omega_{pe} > \omega_{ce}$.

Note that there is a mode just above the lower hybrid frequency. This is the lower hybrid mode. In the ionosphere, it is located in a frequency range populated by whistler emissions, and the vicinity of the two modes in frequency allows for coupling of the whistler mode to the lower hybrid mode. This coupling will be discussed in Section 1.2.

Once the lower hybrid mode has been excited, there is the potential for further interactions. Consider the upper branch of the electrostatic dispersion relation plotted in figure 1-2. The upper branch is the electron plasma wave mode, often referred to as *Langmuir* waves. These high-frequency waves are produced during the ionospheric heating experiments at Arecibo, Puerto Rico. Observations using the 430 MHz radar at Arecibo have shown that they can be scattered by background lower hybrid waves. This interaction will be discussed in section 1.3.

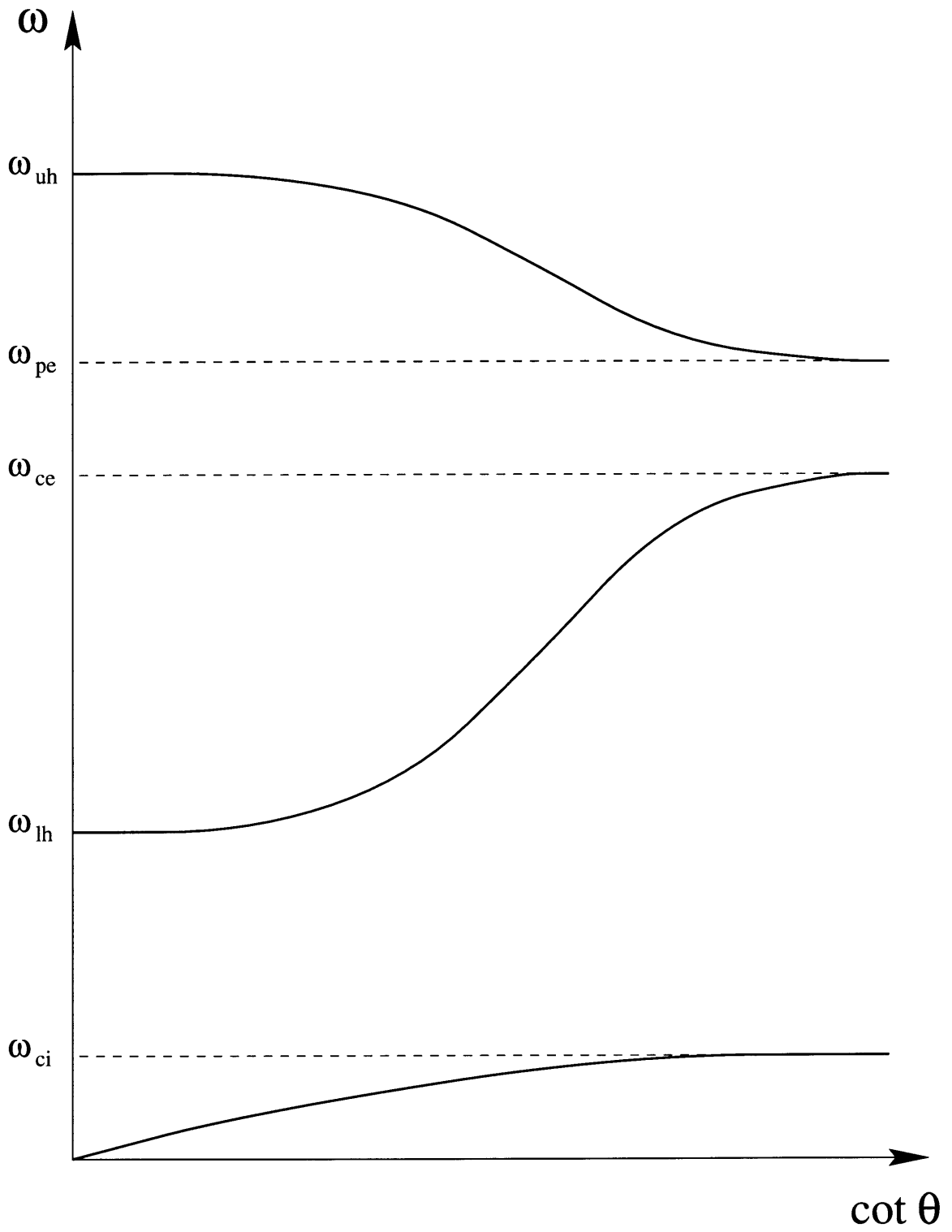


Figure 1-2: The electrostatic dispersion relation.

1.2 Whistler interactions with the ionosphere

Satellites have observed the bandwidth expansion suffered by VLF waves as they traverse the ionosphere from ground-based transmitters [Bell *et al.*, 1983; Tanaka *et al.*, 1987; Chmyrev *et al.*, 1989]. Since VLF waves mode-convert to whistlers when they enter the ionosphere, theories have been developed to explain this broadening in terms of whistler interactions with the ionosphere. If the background plasma is structured, the long-wavelength whistlers could be scattered into short-wavelength lower hybrid waves, which produce a double-humped shape in the measured VLF spectrum due to the doppler shifts of these waves as seen by the moving satellite [Bell and Ngo, 1988; Groves *et al.*, 1988]. Alternatively, in the absence of naturally-occurring scatterers, the whistlers could excite instabilities leading to the production of lower hybrid waves [Riggin and Kelley, 1982; Lee *et al.*, 1984].

The onus is on the author to find evidence for particular theories, namely Groves *et al.* [1988] and Lee *et al.* [1984]. Therefore these two theories will be briefly overviewed.

Groves *et al.* [1988] describes the situation of a whistler mode propagating in the direction of \hat{z} (along the magnetic field) in the presence of plasma containing plasma density irregularities:

$$n_e = N_e + \delta n_e \exp(ik_1 x) \quad (1.34)$$

where n_e is the total electron density, N_e is the background electron density, δn_e is the amplitude of a density perturbation, and $\mathbf{k}_1 = k_1 \hat{x}$ is the wavenumber of the density irregularity. This type of irregularity is known as *field-aligned* because the wavefronts are parallel to the magnetic field lines. Also note that in the case under consideration, the frequency of the irregularity ω_1 is zero, so no time dependence appears in the argument of the exponential.

The total electric field \mathbf{E} of a whistler propagating in this structure is the sum of the fields of the whistler in the absence of irregularities,

$$\mathbf{E}_0 = E_0(\hat{x} + i\hat{y}) \exp[i(k_0 z - \omega_0 t)], \quad (1.35)$$

and the perturbation due to the scattering by the irregularities, \mathbf{E}_s . We can also divide up the plasma current \mathbf{J} into the usual whistler current,

$$\mathbf{J}_0 = -i\omega\epsilon_0\boldsymbol{\chi} \cdot \mathbf{E}_0 = \frac{ie^2N_e\mathbf{E}_0}{m(\omega_0 - \omega_{ce})}, \quad (1.36)$$

and the perturbation due to the irregularities, \mathbf{J}_s . We then substitute these total quantities into the wave equation (in the absence of current \mathbf{J}_{ext} due to external sources):

$$\nabla \times (\nabla \times (\mathbf{E}_0 + \mathbf{E}_s)) + \frac{1}{c^2} \frac{\partial^2}{\partial t^2} (\mathbf{E}_0 + \mathbf{E}_s) + \mu_0 \frac{\partial}{\partial t} (\mathbf{J}_0 + \mathbf{J}_s) = 0. \quad (1.37)$$

Since \mathbf{E}_0 and \mathbf{J}_0 are exact solutions to the wave equation, by the assumption that they are unperturbed whistler fields, and because of the fact that the differential operators in the wave equation are linear operators, we can drop the subscript “0” terms from (1.37). Thus we are left with an equation for the scattered fields,

$$\nabla \times (\nabla \times \mathbf{E}_s) + \frac{1}{c^2} \frac{\partial^2 \mathbf{E}_s}{\partial t^2} + \mu_0 \frac{\partial \mathbf{J}_s}{\partial t} = 0. \quad (1.38)$$

Neglecting ion dynamics, this equation can be solved [Groves *et al.*, 1988] for \mathbf{E}_s :

$$\mathbf{E}_s = E_0 \exp(ik_1x)(\delta n_e/N_e) \exp[i(k_0z - \omega_0t)][\hat{\mathbf{x}} + (\hat{\mathbf{x}} + i\hat{\mathbf{y}})(\lambda^2/\lambda_c^2)] \quad (1.39)$$

where

$$\lambda = 2\pi/k_1 \quad (1.40)$$

$$\lambda_c = \sqrt{2\pi}(c/\omega_{pe})(\omega_{ce}/\omega_0)^{1/2}. \quad (1.41)$$

By assumption, $|\mathbf{k}_1| \gg |\mathbf{k}_0|$, which leads to $\lambda^2 \ll \lambda_c^2$. Thus

$$\mathbf{E}_s \approx E_0 \exp(ik_1x)(\delta n_e/N_e) \exp[i(k_0z - \omega_0t)]\hat{\mathbf{x}}. \quad (1.42)$$

There are three items to immediately note about \mathbf{E}_s .

First, the amplitude of the scattered wave is nonlinear. In other words, it depends

on the *product* of the scattering irregularity amplitude $\delta n_e/N_e$ and the amplitude of the incident whistler \mathbf{E}_0 . This is a characteristic feature of many nonlinear processes, of which this mechanism is one.

Second, the scattering process has led to the following relations between the wavenumbers and frequencies of the scattered fields and the source fields:

$$\mathbf{k}_s = \mathbf{k}_0 + \mathbf{k}_1 \tag{1.43}$$

$$\omega_s = \omega_0 + \omega_1. \tag{1.44}$$

These frequency- and wavenumber-matching conditions are another characteristic feature of nonlinear processes. Note again that ω_0 is zero in the special case of non-propagating density irregularities considered here.

Third, the polarization of the scattered wave is longitudinal. In other words, \mathbf{E}_s is approximately parallel to the direction of propagation $\mathbf{k} + \mathbf{k}_0$ ($\approx \mathbf{k}$). Accordingly, the scattered field \mathbf{E}_s is dominated by its longitudinal component \mathbf{E}_L rather than its transverse component \mathbf{E}_T , suggesting a similarity to the nature of the solutions to the electrostatic approximation of the susceptibility tensor.

Assuming that the background field of density irregularities is spread in wavenumber, it is certainly possible for the wavenumber and frequency of the scattered fields to match the dispersion relation of the lower hybrid mode, and thus the scattered fields can freely propagate as lower hybrid waves. Again, it is these short-wavelength lower hybrid waves that give rise to a double-humped spectrum around the frequency ω_0 as seen by the observing satellite flying through the plasma medium.

One critical requirement of the above description of bandwidth expansion is the presence of field-aligned structure. Fortunately, there are numerous naturally occurring field-aligned irregularities in the ionosphere [e.g., *Fejer and Kelley, 1980*] and therefore plenty of opportunity to excite lower hybrid waves via this mechanism. Furthermore, it is also possible to generate field-aligned irregularities in laboratory plasmas, allowing one to test this scattering mechanism by launching whistlers from an antenna, as is described in this thesis. Alternatively, one can use natural emissions

of the plasma as a source whistler wave [Lee *et al.*, 1998]. A detailed theory explaining how field-aligned structures could arise in a laboratory device is given in appendix A.

However, it is sometimes the case that such irregularities do not exist, and then one must turn to other ways to explain the generation of lower hybrid waves. Lee *et al.* [1984] argue that nonlinearities in the fluid equations can lead to the parametric excitation of lower hybrid waves by large amplitude whistlers.

Parametric instabilities can be illustrated by means of a simple one-dimensional example. Let us consider the dynamic equations for two quantities involved in two different wave modes of a plasma, $n_1(t)$ and $n_2(t)$. These could represent, for example, fluctuating plasma densities. Let us say that the quantities follow second-order behavior over the frequency ranges where they respond to stimuli (in the vicinity of their natural frequencies ω_{n1} and ω_{n2}) and that they exhibit damping ratios ζ_1 and ζ_2 . In the absence of excitation, these systems can be described by

$$\left(\frac{d^2}{dt^2} + 2\omega_{n1}\zeta_1 \frac{d}{dt} + \omega_{n1}^2 \right) n_1(t) = 0 \quad (1.45)$$

$$\left(\frac{d^2}{dt^2} + 2\omega_{n2}\zeta_2 \frac{d}{dt} + \omega_{n2}^2 \right) n_2(t) = 0. \quad (1.46)$$

Now let us consider a situation where the two systems are coupled in the following manner. Let us suppose that the first system is driven by a force which is proportional to the product of the amplitude of n_2 and a background oscillating *pump* electric field E_0 . Furthermore, suppose the second system is driven by the product of n_1 and the pump field E_0 . This represents a situation often encountered in the elementary analysis of nonlinearities in interacting wave fields. Under these conditions, the dynamic equations for the two systems are:

$$\left(\frac{d^2}{dt^2} + 2\omega_{n1}\zeta_1 \frac{d}{dt} + \omega_{n1}^2 \right) n_1(t) = a_1 n_2(t) E_0(t) \quad (1.47)$$

$$\left(\frac{d^2}{dt^2} + 2\omega_{n2}\zeta_2 \frac{d}{dt} + \omega_{n2}^2 \right) n_2(t) = a_2 n_1(t) E_0(t) \quad (1.48)$$

where a_1 and a_2 represent the degree of coupling between the two modes. Now let

us say that the pump is an electric field oscillating as $\hat{E}_0 \cos(\omega_0 t)$ and that random thermal motion produces a component of $n_2(t)$ with frequency ω . The pump wave will beat with the fluctuation in $n_2(t)$ to produce excitation of the first system at the sum and difference frequencies $\omega_0 \pm \omega$. Let us say that the first system cannot respond at the sum frequency $\omega_0 + \omega$, but is indeed able to respond at $\omega_0 - \omega$. Therefore $n_1(t)$ will start to oscillate at a frequency $\omega_1 = \omega_0 - \omega$. Looking at the second system, $n_1(t)$ will beat with $E_0(t)$ to produce excitation of the second system at frequencies of $2\omega_0 - \omega$ and ω . Suppose the second system responds at ω , but not at $2\omega_0 - \omega$. Then $n_2(t)$ will start to oscillate at a frequency $\omega_2 = \omega$.

This relationship between the response frequencies of systems n_1 and n_2 and the frequency of the pump field E_0 is another example of frequency matching conditions:

$$\omega_1 + \omega_2 = \omega_0. \quad (1.49)$$

If the process also had spatial dependence, we would be faced with wavenumber matching conditions as well. As in the case of *Groves et al.* [1988], these matching conditions arise from the nonlinear nature of the driving terms for the modes of the plasma.

If we keep E_0 real, however, a little reflection will reveal that we are still able to use the method of complex exponentials for n_1 and n_2 , leaving us with:

$$(\omega_1^2 - (\omega - \omega_0)^2 - 2i\omega_1(\omega - \omega_0)\zeta_1)\hat{n}_1 = c_1\hat{n}_2\hat{E}_0/2 \quad (1.50)$$

$$(\omega_2^2 - \omega^2 - 2i\omega_2\omega\zeta_2)\hat{n}_2 = c_2\hat{n}_1\hat{E}_0/2 \quad (1.51)$$

where \hat{n}_1 and \hat{n}_2 are the complex amplitudes of the field quantities n_1 and n_2 , and E_0 is a real amplitude. Note the factor of 1/2 that arises because the sum frequencies are not included in the driving forces. The equations can be written as a matrix:

$$\begin{pmatrix} \omega_1^2 - (\omega - \omega_0)^2 - 2i\omega_1(\omega - \omega_0)\zeta_1 & -c_1\hat{E}_0/2 \\ -c_2\hat{E}_0/2 & \omega_2^2 - \omega^2 - 2i\omega_2\omega\zeta_2 \end{pmatrix} \begin{pmatrix} \hat{n}_1 \\ \hat{n}_2 \end{pmatrix} = 0. \quad (1.52)$$

Clearly, the right side can only be zero if the determinant is zero.

$$(\omega_1 - (\omega - \omega_0)^2 - 2i\omega_1(\omega - \omega_0)\zeta_1)(\omega_2^2 - \omega^2 - 2i\omega_2\omega\zeta_2) = c_1c_2\hat{E}_0^2/4 \quad (1.53)$$

This is the dispersion relation. The only quantity in this equation which has not been constrained is the imaginary part of ω . This quantity represents the exponential growth rate of oscillations proportional to $\exp(-i\omega t)$. Therefore the dispersion relation will solve to give us the size of $\Im(\omega)$ as function of the pump field amplitude \hat{E}_0 . An interesting value of \hat{E}_0 is the one which will result in marginal stability, or in other words, a growth rate of $\Im(\omega) = 0$. Let us call it \hat{E}_{thres} to denote that it represents the threshold of instability.

We can see from (1.53) that the threshold field \hat{E}_{thres} is smallest when the frequencies of the driving functions are tuned to the natural frequencies of the second order systems. This occurs when $\omega_0 - \omega = \omega_{n1}$ and $\omega = \omega_{n2}$. While these are not the same as the frequency matching conditions mentioned earlier, the fact that the threshold is minimized leads to favorable excitation of modes around the natural (resonant) frequencies. A vivid example of this tuning will be seen later in the discussion of Stokes/anti-Stokes waves in section 1.3.

Let us consider the case of favorable tuning, and eliminate \hat{x}_1 and \hat{x}_2 to find the minimum threshold field to excite the parametric instability:

$$\hat{E}_{thres} = 4\omega_1\omega_2\sqrt{\frac{\zeta_1\zeta_2}{c_1c_2}} \quad (1.54)$$

Note that the threshold goes to zero as the damping goes to zero.

After this simple example, we return to the discussion of *Lee et al.* [1984]. The argument of the paper is that a large amplitude whistler wave can act as a pump field for a parametric instability involving several daughter waves. While the above example was a three-wave parametric instability, *Lee et al.* [1984] argues a four-wave instability—three modes of the system become excited in the presence of the pump. Two of the modes in this instability are lower hybrid waves, which are natural modes

of the system, and the third mode is a so-called purely growing mode—a wave with zero real frequency, but finite imaginary frequency. The reason for the four-wave process is that it has a much lower threshold than the three-wave process of *Riggin and Kelley* [1982] and can also easily explain the observed double-humped broadened VLF spectrum in terms of oppositely directed lower hybrid waves. For parametric excitation of the modes, the following wavenumber and frequency matching conditions are observed:

$$\omega_0 = \omega_+ - \omega_s = \omega_- + \omega_s^* \quad (1.55)$$

$$k_0 \hat{\mathbf{z}} = \mathbf{k}_+ - \mathbf{k}_s = \mathbf{k}_- + \mathbf{k}_s \quad (1.56)$$

where * denotes complex conjugation, “0” denotes the whistler wave, “+” and “-” denote the lower hybrid waves, and “s” denotes the purely growing mode. Since the purely growing mode is not a natural mode of the plasma, the effects of detuning, as well as collisional damping between the plasma species, impose a threshold on the instability, as was also seen in the simple parametric instability example given earlier.

Lee et al. [1984] propose instabilities in two frequency regimes:

$$\omega_{lh} \left(1 + \frac{M}{m} \frac{v_{te}^2}{c^2} \frac{\omega_{pe}^2}{\Omega_e^2} \right)^{1/2} < \omega_0 < \omega_{pi} \quad (1.57)$$

and

$$\omega_{pi} < \omega_0 \quad (1.58)$$

where v_{te} is the thermal velocity of electrons, $\sqrt{2KT_e/m_e}$. K is Boltzmann’s constant, and T_e is the temperature of the electron species. The electric field thresholds in these two respective regimes are:

$$\hat{E}_{thres} = 1.2(m/e)\nu_e v_{te} |\eta|^{1/2} \quad (1.59)$$

and

$$\hat{E}_{thres} = 0.86(k_s^2 v_{te}^3 / \Omega_e)(m/e)[1 + (1 + 4\Omega_e^2 \nu_e^2 \eta^2 / k_s^4 v_{te}^4)^{1/2}]^{1/2} / |\eta|^{1/2} \quad (1.60)$$

where ν_e is the frequency of collisions between electron and ion species and η is given by

$$\eta = [1 + (M/m)(k_0/k_s)^2]/[1 - (M/m)(k_0/k_s)^2(\Omega_e/\omega_{pe})^2] \quad (1.61)$$

In this thesis, the aim is to test predictions of the parametric generation of lower hybrid waves and zero-frequency modes as described above. A quick check of the above thresholds shows that in a laboratory machine, with $\nu_e = 10^6 \text{ s}^{-1}$ and $v_{te} = 2 \times 10^6 \text{ m/s}$ for example, the threshold for the first regime could be as small as tens of volts per meter, which is obtainable from a modest 100 W transmitter located inside the machine.

1.3 Role of lower hybrid waves in heating experiments

1.3.1 The Arecibo Radar

The Arecibo observatory is a large radio telescope/radar located in western Puerto Rico. A picture of the facility is shown in figure 1-3.

It consists of a spherical dish 305 m in diameter, with a 245 m radius of curvature, built over a large limestone sink-hole. The dish consists of a network of cables suspending a patchwork of aluminum reflecting panels over the bowl. A platform is suspended 140 m above the dish. The platform contains feeds for the various receiving and transmitting frequencies. Since the primary reflector is spherical, the line of sight of the radar can be steered by moving the feed. The feed is mounted on a bow-shaped track hanging from a turntable. This mechanism can rotate the feed 360 degrees in azimuth and point the feed up to 20 degrees from zenith. The steering capability is critical for tracking astronomical radio sources, although only marginally relevant for ionospheric observations. The drawback to the spherical reflecting surface is that the focus of the dish is a line rather than a point (in the case of a parabolic dish). A 29-meter long waveguide with large openings on the sides (known as a *linefeed*) is

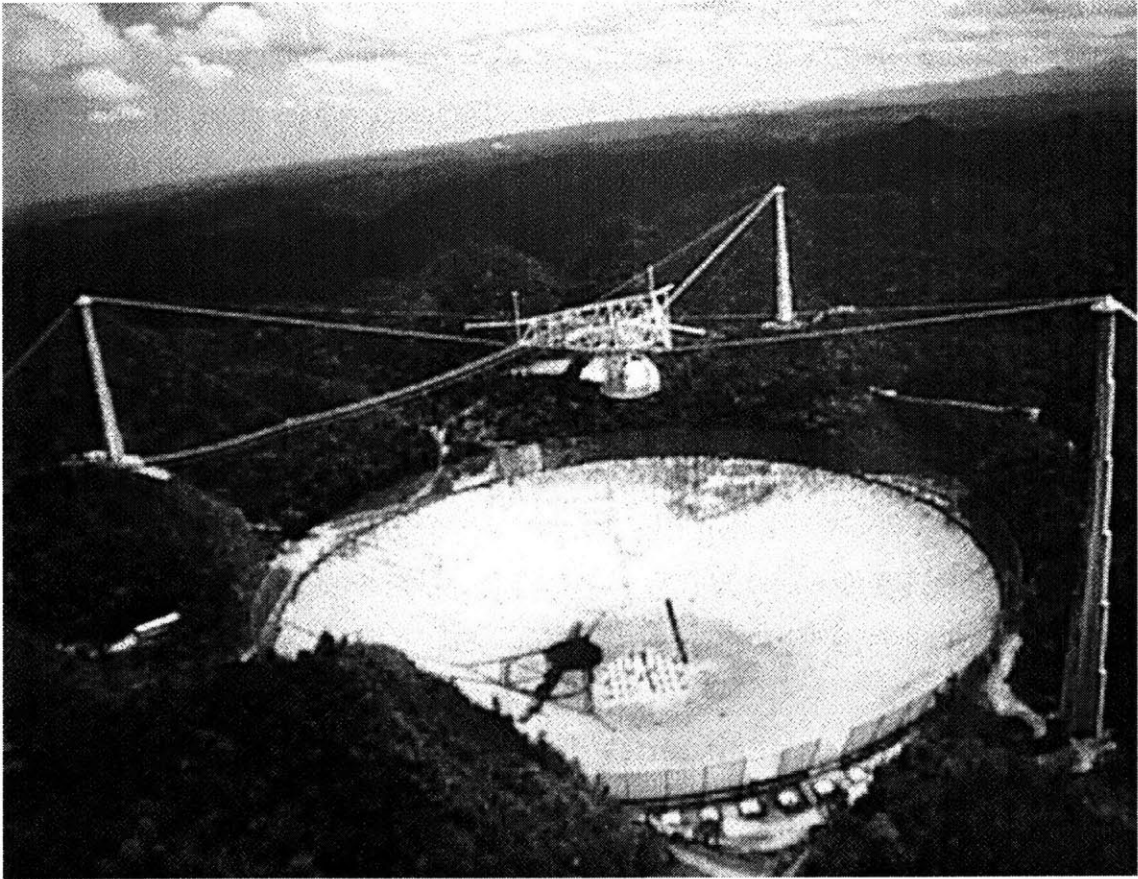


Figure 1-3: The Arecibo Radar Telescope.

used to collect the signals, although the apparatus is inefficient. Recently, a Gregorian dome has been mounted on the platform, whereby secondary and tertiary reflectors converge the rays to a point focus.

When the observatory is operated as a radar, 430 MHz transmitter pulses are generated on the ground by a pair of klystrons and sent up to the platform through a waveguide. The pulses are then launched into the ionosphere via the primary reflector. Typically, the mode of operation is tailored so that one can monitor Thomson scatter from the ionosphere over a range of 50 km to about 1000 km, although much larger ranges are obtainable by special request. Thomson scatter arises from the radar signals propagating through index of refraction variations due to random thermal motions of the electrons and ions. The return signals have (nearly) random phase, which has given rise to the popular term Incoherent Scatter (IS). Thomson (or incoherent) scattering should be distinguished from Bragg (or coherent) scattering, whereby radar signals are scattered by half-radar-wavelength index of refraction fluctuations due to modes propagating in the plasma. This Bragg scatter is orders of magnitude larger than the Thomson scatter, and can be detected with portable radar systems. At Arecibo the data acquisition system is set up to accommodate observations of both Bragg and Thomson scattering.

1.3.2 Heating experiments

The ionospheric heating experiments at Arecibo started in the early 1970s. The experiments involve actively perturbing the ionosphere with high power HF waves and monitoring the plasma mode responses using the Arecibo radar.

Currently, the HF waves are generated by a field of vertically aimed wideband log-periodic antennas located about 17 km to the northeast of the radar. Up to 800 kW can be launched at one of four frequencies: 3.175, 5.1, 7.4, or 8.175 MHz. The waves are typically launched in right- or left-hand circular polarization, which convert respectively into ordinary and extraordinary polarizations in the ionospheric plasma (i.e., the \pm cases of the Appleton-Hartree relation [1.20]). During entry into the plasma, the O-mode ray tends to diverge from the X-mode ray, until the O-mode is

propagating across the field and the X-mode almost along the field [*Budden, 1985*]. Interest here will be in the perpendicular-propagating O-mode, which will follow the Appleton-Hartree relation for the (+) case when $\theta \approx \pi/2$, so that

$$n^2 \approx 1 - \frac{\omega_{pe}^2}{\omega^2} \quad (1.62)$$

The ordinary mode propagates upward until it is cut-off (at zero index of refraction), which is the point where the local plasma frequency equals the heater wave frequency. The wave then reflects and returns down the same ray path. The upward- and downward-going waves form a standing wave (Airy function) interference pattern which can result in large electric field strengths near the reflection height. The pattern can be deduced from assuming that the wave sees a locally linearly increasing plasma density with height as it approaches the reflection height.

Near the reflection height, the electric fields of the heater wave can exceed the threshold for certain parametric instabilities. One particular instability, the parametric decay instability (PDI), has been observed during the heating experiments. In the PDI, the incident O-mode heater wave excites two natural modes of the plasma—Langmuir waves and ion acoustic waves. Although Langmuir waves have been mentioned earlier, the ion acoustic waves only arise from finite-temperature considerations of the plasma, and follow the dispersion relation:

$$\omega = k \sqrt{\frac{T_e}{m_i}}. \quad (1.63)$$

The coupling to these two natural modes only occurs above a threshold field strength which is determined by the collisional damping of the wave modes in question. When coupling does occur, it follows the wavenumber and frequency matching conditions

$$\mathbf{k}_O = \mathbf{k}_L + \mathbf{k}_{IA} \quad (1.64)$$

$$\omega_O = \omega_L + \omega_{IA} \quad (1.65)$$

where “O”, “L” and “IA” refer to electromagnetic ordinary mode, Langmuir and ion acoustic waves, respectively. A second nonlinear interaction is then thought to occur, whereby the PDI-excited Langmuir waves impinge on background lower hybrid wave fields. This second interaction is not a parametric instability, but is rather a scattering mechanism similar in nature to *Groves et al.* [1988]. Langmuir waves propagating at small angles θ to the magnetic field interact with lower hybrid waves, resulting in scattered Langmuir waves at larger angles. The wavenumber and frequency matching conditions for the scattering are shown in figure 1-4. The wavenumber picture has been drawn out as vectors to show how the radar detects the oblique scattered waves via Bragg (back)scattering. Since the Arecibo radar is monostatic and nearly vertically elevated, only Bragg scatter from near vertical-propagating plasma modes can be observed.

Attention should be paid to the fact that obliquely propagating waves at the sum frequencies (anti-Stokes waves) can satisfy the upper branch of the electrostatic dispersion relation, since they are above the plasma frequency. However, the oblique waves at the difference frequencies (Stokes waves) are not natural modes, and are therefore damped.

Coherent backscatter radar data is shown in figure 1-5 [*Vilece, 1992*]. Notice the anti-Stokes wave, frequency upshifted from the pump wave frequency (at 0 Hz) by the frequency of an unseen lower hybrid mode wave, and the lack of a Stokes wave, presumably due to damping. It is unfortunate that the perpendicular-propagating lower hybrid waves are unobservable with the Arecibo radar. To detect them monostatically would require an oblique-pointing radar. Fortunately, coherent radar returns would be fairly strong and likely detectable using portable radar systems.

The key to proving the above interaction involves showing the role of lower hybrid waves in this second process. While they cannot be observed with the radar, they certainly can be probed in a laboratory plasma. In figures 1-6 and 1-7, anti-Stokes Langmuir waves and their associated lower hybrid wave scatterers are shown in frequency spectra taken in a laboratory plasma [*Lee et al., 1997; Lee et al., 1998*]. Note the frequency shift of the anti-Stokes waves (~ 60 MHz) is comparable to the fre-

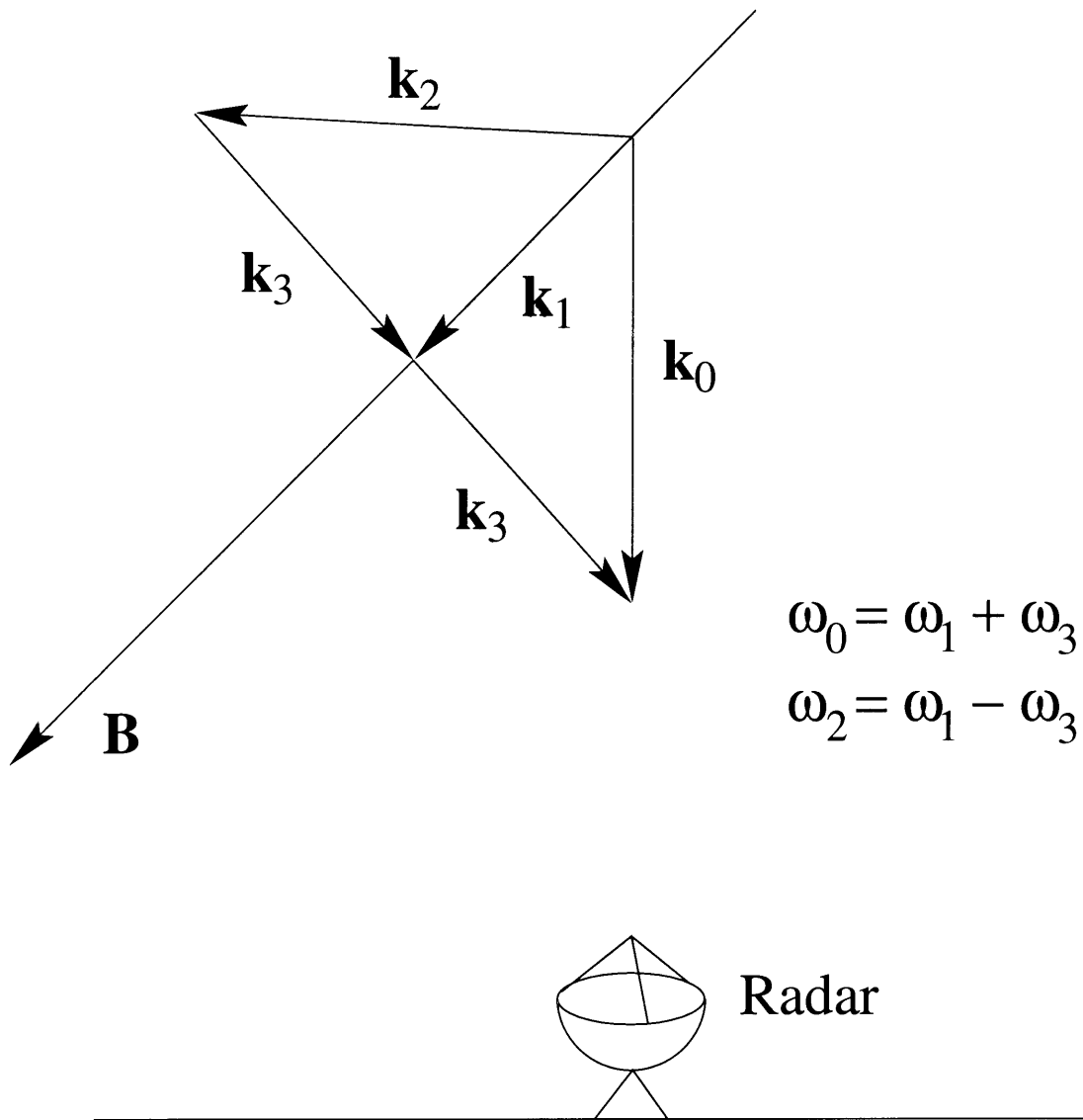


Figure 1-4: The wavenumber and frequency matching relations for Langmuir wave scattering at Arecibo. "1" represents the source Langmuir wave, "0", the frequency-upshifted Langmuir wave, "2", the frequency-downshifted Langmuir wave, and "3", the lower hybrid wave.

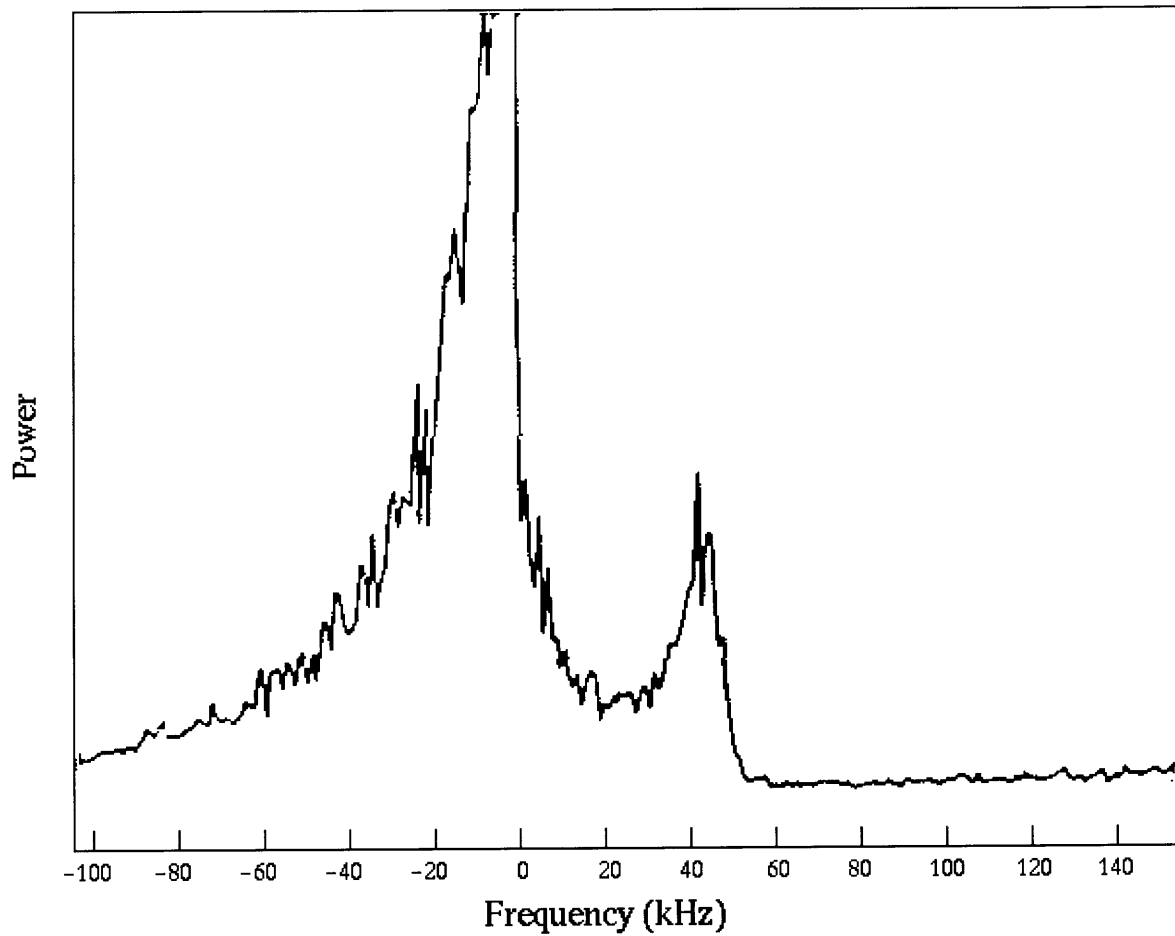


Figure 1-5: Spectrum of O-mode pump wave-excited Langmuir waves as detected by the Arecibo radar.

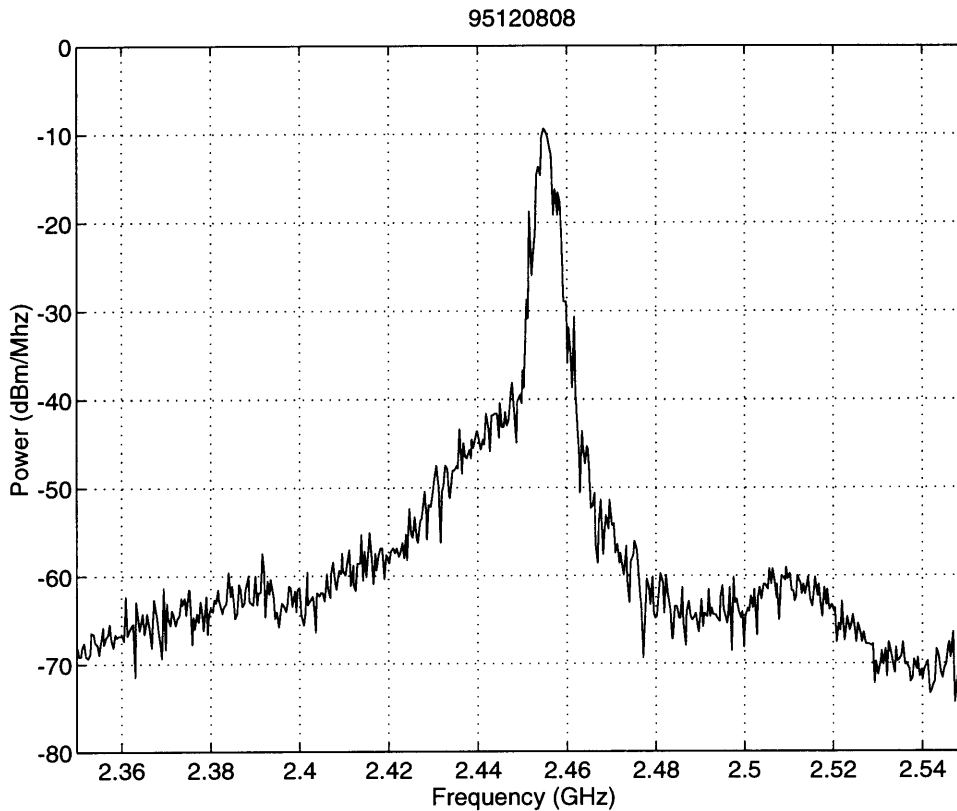


Figure 1-6: Spectrum of O-mode pump wave-excited Langmuir waves in the VTF machine.

quency of the bump representing lower hybrid waves (marked f_{lh}) in the low-frequency spectrum.

While the laboratory picture gives some evidence in favor of the scattering mechanism, the outstanding question in both the ionosphere and in the laboratory is: what is the mechanism for exciting the lower hybrid wave scatterers? In the ionosphere, lightning-produced whistlers are thought to give rise to lower hybrid waves via the mechanisms proposed earlier. In the laboratory, it is thought that whistlers are emitted as bremsstrahlung radiation and excite lower hybrid waves via similar means.

In summary, two phenomena have been presented: the observations of spectral broadening of VLF from ground-based transmitters and the excitation of frequency-upshifted waves during the heating experiments. Both are thought to be due to

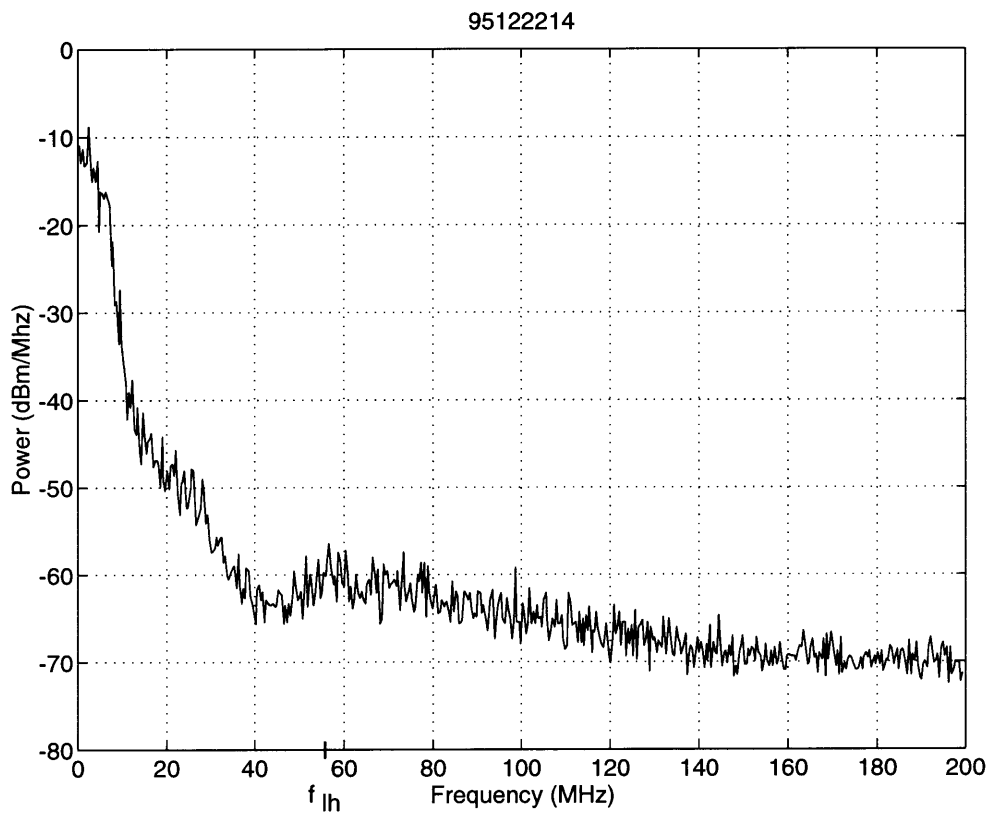


Figure 1-7: Spectrum of lower hybrid waves seen in the VTF machine.

the effect of lower hybrid waves, and therefore an understanding of both phenomena would benefit from a controlled laboratory experiment designed to determine when, where and why whistlers can excite the lower hybrid mode. The need for experimental methods to retrieve this information provides the motivation for the development and evaluation of the techniques described in this thesis.

Chapter 2

Experimental Apparatus

2.1 Overview of facility

The Versatile Toroidal Facility (VTF) is a large plasma device located in the west (TARA) cell of the MIT Plasma Science and Fusion Center. It consists of a toroidal vacuum chamber, 94 cm in major radius. The chamber is wound with electromagnets which generate a toroidal magnetic field for plasma confinement. To produce plasma, small amounts of hydrogen are leaked into the chamber and ionized by applied electromagnetic fields and/or energetic particles. Once the plasma is produced, perturbations and diagnoses can be made by antennas and probes inserted through ports in the outer chamber wall.

2.1.1 Vessel and vacuum system

A photograph of the machine is shown in figure 2-1. The chamber consists of a rectangular cross-section toroidal structure, with a volume of 5.4 m^3 . It is built from stainless steel with a wall thickness of 19.1 mm (0.75") everywhere except for the inside wall, which is 12.7 mm (0.5") thick. In terms of the in-vessel measurements, the inner wall is located at a major radius of 61.6 cm (24.25") and the outer wall is at 126.4 cm (49.75"). The interior height of the chamber is 106.7 cm (42").

The chamber is built in two halves, with the halves being connected by an insu-

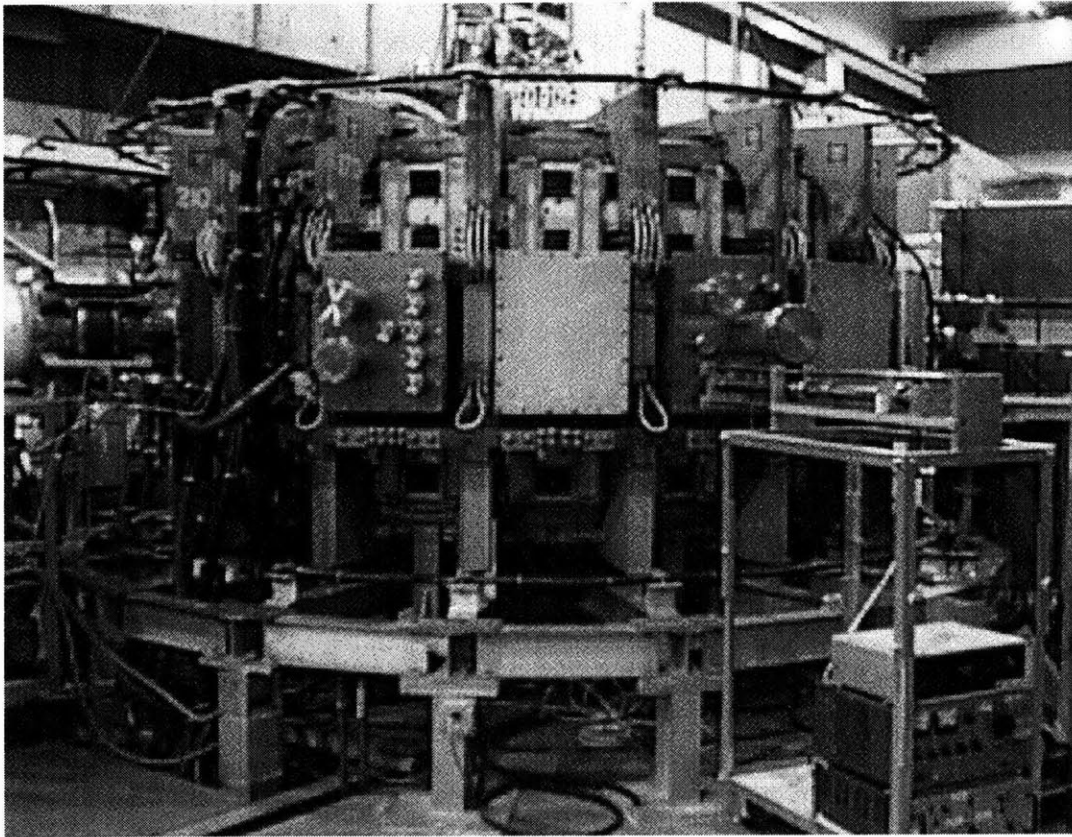


Figure 2-1: The VTF machine.

lating flange to prevent toroidal current flow in the chamber walls. 48 ports allow for the mounting of diagnostics on the top, side and bottom of the machine. The side ports extend out 50.8 cm (20") beyond the outer wall in order to allow one to retract probes out of the plasma. The top and bottom ports extend 4.4 cm (1.75") from the top and bottom walls, mainly to allow for the drilling of threaded bolt holes for attaching the port covers. The 48 ports are sealed with rubber o-rings. All of the smaller half nipples mounted on the ports, and almost all probe flanges, are sealed with copper gasket knife-edge seals. The port covers are made of either stainless steel (appropriate for welding on standard vacuum components) or aluminum (for ease of machining and lifting on and off the chamber). Port locations are referred to by the angular position with respect to due north. For example, ports would be named 20 degrees, 40 degrees, and so on.

The chamber is evacuated by a Leybold 450 L/s turbomolecular "turbo" pump in series with a General Electric 15 L/s trivac roughing pump. During pumpdown from atmospheric pressure, the roughing pump is attached directly to the chamber in order to lower the pressure to around 100 mtorr. After that pressure is achieved, the turbopump is switched on and the roughing pump proceeds to pump on the exhaust of the turbo pump. Normally a base pressure of 3×10^{-7} torr is achievable. The major limiting factor on the base pressure is the diffusion associated with the rubber o-ring seals on the port covers.

During plasma operation, small amounts of hydrogen are leaked into the chamber using a controlled leak apparatus regulated by a PID feedback loop. The pressure is observed using an ion gauge meter. Typical operating pressures are $1-2 \times 10^4$ torr of H₂. Argon is also available via an unregulated leak valve. A camera monitors the pressure level of the gauge and the level is displayed on a monitor in the control room. An electrical input is available for external control of the feedback loop input voltage, but it is not currently being used.

2.1.2 Magnet system

Around the chamber are wound 18 Westinghouse 4-turn electromagnets, each 1.35 m wide and 1.68 m tall. They are designed for operation at up to 1.2 T, but are not currently used above 0.2 T. The magnets are designed to be water-cooled, although they are not run as such during typical operation. The magnetic field resulting from the TF coils is approximately 144 gauss per kA of coil current at 1 meter major radius. Two 6-pulse 240 V, 7000 A phase-controlled power supplies feed the magnet coils in parallel. A set of two water-cooled free-wheeling diodes are placed across the bus to maintain unipolar voltage across the magnets, and to carry the TF current in the case of power supply failure. The supplies are run open-loop, in other words, a reference signal determines the average DC output voltage of the supply, and the resistance of the leads and TF coil determine the current. The resistance of the TF coil does not noticeably change during typical shots, so feedback control has not been necessary.

In addition to the toroidal field, a vertical field (parail) coil system is available as one pair of Helmholtz coils of 2 turns each, equally spaced above and below the midplane. The coils are 1.92 m in radius and are spaced 1.64 m apart. The on-axis field generated by these coils is approximately 10.2 gauss/kA. The coils are fed by a single 6-pulse 16 V, 2500 A phase-controlled power supply. The output of the supply is fed through a large inductance to ensure small ripple on the output current.

Additional poloidal field coils (two pairs of null and trim coils of four turns each) and inner divertor coils (one pair, 12 turns each) are available but are not currently attached to any power supply. A central solenoid exists and is wound in five sections of 25, 8, 8, 2 and 2 turns. It is presently being run at high frequency (around 1 KHz), as described in the next section.

2.1.3 Plasma sources

ECRH

Of the three available methods of plasma production, the simplest is Electron Cyclotron Resonance Heating (ECRH). A 3 kW magnetron generates microwaves at 2.45 GHz, which are sent along a waveguide, through a ceramic vacuum microwave feedthrough on the 40-degree side port, and out a launching horn. To achieve low reflected power, the horn was designed to be as large as possible and still fit within the port extension. To future reduce the reflected power returning to the magnetron, a circulator is placed near the mouth of the magnetron, and return power is dumped into a water-cooled dummy load. In addition, a bidirectional coupler (-55.6 dB coupling) is placed between the circulator and the magnetron to allow monitoring of the forward and reflected power.

The magnetron is generally run CW, although it can be pulsed up to approximately 5 KHz. The plasmas that are produced depend on the magnetic field employed. A pure toroidal magnetic field results in a broad parabola-shaped profile with a peak density of approximately $3 \times 10^{16} \text{ m}^{-3}$ when the microwave is injected in ordinary mode. With application of the vertical (parail) field, the peak density can rise by a factor of 1 to 1.5, depending on the size of the applied field.

Electron Emission

The second plasma source involves two hot-cathode electron emitters mounted on the bottom of the chamber, 180 degrees apart. A photograph of one of the emitters is shown in figure 2-2. Each emitter consists of a horizontal carbon rod about 15 cm long, threaded with rings of LaB_6 with a total surface area of 90 cm^2 . The rod is held between two vertical carbon blocks to which the rod is electrically attached via a tapered peg-hole connection. The carbon vertical blocks are each mounted on a horizontal copper plate, which in turn is connected to a vertical copper post. The copper posts travel through a bottom port cover to electrical hookups outside the chamber. The legs are electrically isolated from the port cover. This isolation is

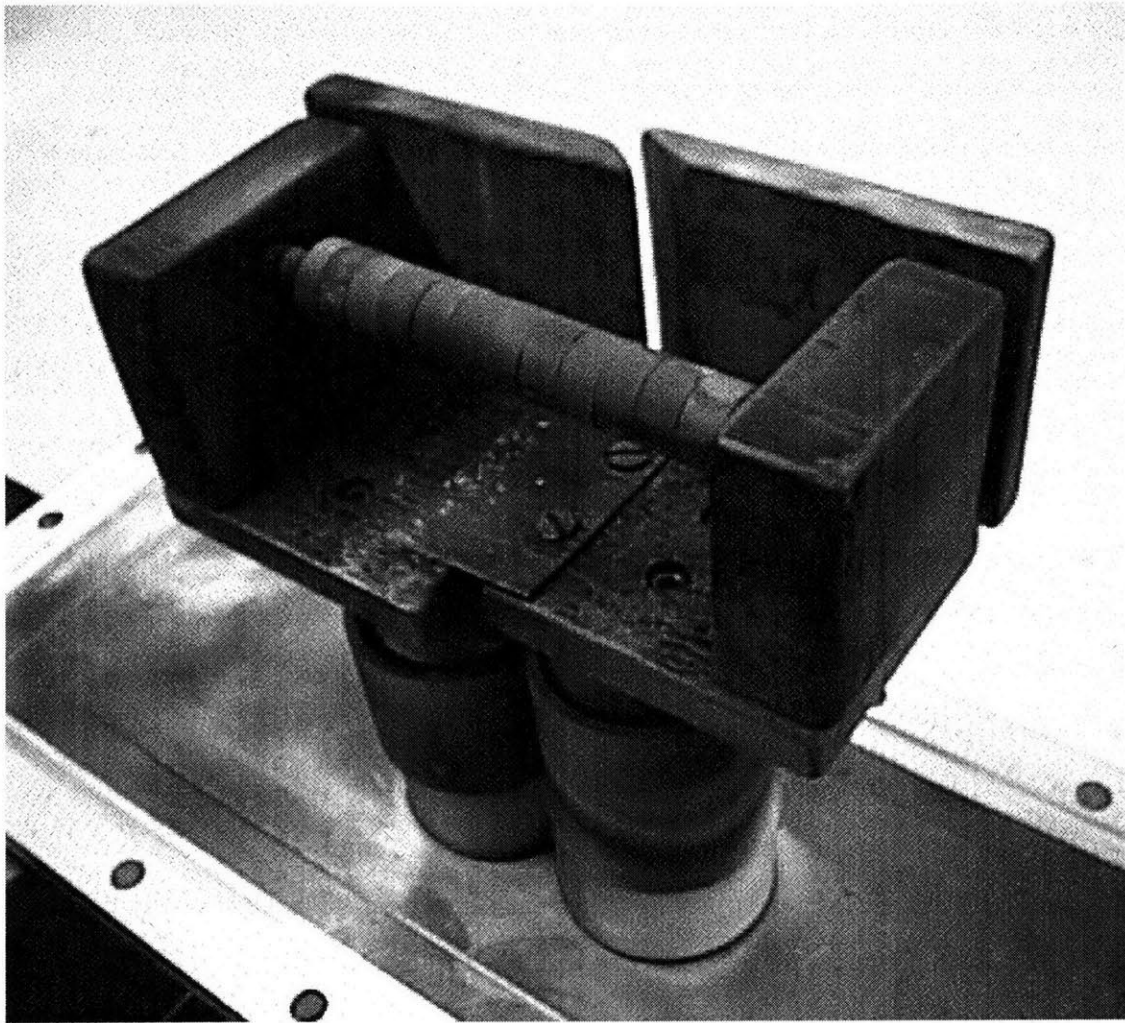


Figure 2-2: An electron-emitting filament. This is an early version featuring carbon backshields. The machine-mounted emitters have stainless steel backshields.

accomplished by tapering the copper legs as they pass through the port cover, and inserting a delrin shield between the posts and the edges of the holes in the port cover. This shield is held in place by a downward force on the copper legs. The copper post is threaded on the outside of the port cover, to allow a large delrin nut to be screwed onto the copper post. The nut (1) applies the downwards force necessary to hold the shield in place and (2) allows one to compress o-rings between the post and shield and between the shield and the port cover. To keep the copper legs from melting during operation of the emitter, the legs have been bored out and fitted with a coaxial water circuit.

The emitter is operated by passing current through the carbon filament. Typically, an applied voltage of 12 V will cause the filament to draw between 350 and 400 A. After 60 seconds, the lanthanum rings reach a temperature of approximately 1600 degrees (as determined by a window-based pyrometer). At this point, both legs of the filament are biased to -360 volts with respect to the chamber wall. The hot, biased LaB_6 then emits electrons, which propagate along the field lines of the machine. Normally, the vertical field is operated in tandem with the toroidal field so that the electrons spread throughout the machine via a helical trajectory. The pitch angle of the helix is typically 1-2 degrees. When the beams reach the top of the machine, they are collected by a vertically oriented stainless steel plate just below the ceiling of the machine. The plate is 45.7 cm wide (18") and 17.8 cm high (8").

Stainless steel shields are placed at the rear of each emitter, electrically connected to the copper horizontal plates, in order to force the electrons to travel in the correct direction along the helix. Stainless steel was chosen after it was discovered that carbon backshields sputtered when grazed by the electron beam fired forward from the filament on the other side of the machine. This sputtering would result in the surface of the emitter being coated with a fine carbon residue. The carbon residue would reduce performance and cause unpredictable behavior.

The power supplies feeding the filaments during the heating phase are similar to the vertical field supply: 6-pulse, 16 V, 2500 A, with a large output inductance. The power supplies feeding the filaments during the bias phase are quite different.

The supplies are 12-pulse phase-controlled, rated at 180 V, 600 A. The phase-control is performed on the primary side and the power is fed through Y/Y- and Δ /Y-connected transformers. The two secondaries are fed to two diode bridges coupled by an interphase transformer. Early in the operation of VTF it was realized that higher bias voltages are desirable, so the interphase transformer was disconnected and the two bridges were wired in series. Furthermore, it was found that faster regulation was necessary than was attainable with the primary-side firing circuit. A network of switchable resistors on the output of the supply was devised to allow the output current to be controlled on a 10 μ s time scale. Each supply has 5, 500 W, 3 Ω resistors in parallel on the output. Each resistor is in series with a 600 V, 300 A, Darlington-connected bipolar junction transistor (BJT). Since the current emitted from the filaments varies with the applied bias voltage, the current can be regulated by individually turning on and off each BJT and effectively varying the output resistance of the supply on a much shorter time scale than the plasma confinement time (which is around 1 ms).

Normally, the desire is to have as much emitted current as possible, so all the BJTs are on. However, since the plasma conditions can vary, there is need for overcurrent protection on the supply. When the output current reaches a set point, such as 250 A, the fiber optic-linked firing module starts selectively turning on and off the BJTs in an attempt to regulate the current. The regulator works quite well, as it is only limited by the bandwidth of the fiber optic transmitters (300 KHz) and the turn-on time of the BJTs (10 μ s). There is also undervoltage protection. If the output voltage of the supply drops below 50 V as measured at the emitter (due to an arc, for example) the BJT controller turns all the switches off for a period of 30 ms to allow the arc to extinguish.

During successful emission of electrons, a fairly dense plasma, approaching 5×10^{17} m⁻³ in density and 10 eV in temperature, can be created with approximately 100 A total emitted current from two filaments.

To reach higher densities, as was desired for a sizeable value of ω_{pe}/ω_{ce} , the author decided that some modifications to the power supplies could be done to increase the

power of the electron beams. As described above, 2 power supplies are currently being used to apply -360 V bias to each filament. However, there exist two additional 360 V supplies that were at one point being used to power two additional filaments. It had been discovered at that time that the four filaments, mounted at roughly 90 degree spacing inside the machine, were not able to launch the helical electron beams in a reliable manner, because the emitters interfered with each other's operation. The idea was that these two additional supplies could now be used in series with the two original supplies. Leads were run between the two pairs of supplies, so that the two original supplies would operate between a voltage of -360 V and -720 V with respect to ground, and the two additional supplies would be used to bias the positive side of the original supplies down to -360 V. Some discussion of operation under these conditions is given in chapter 3.

Ohmic heating

The third method of generating plasma involves driving current through the plasma using a transformer coil placed in the aperture of the torus. Power supply capability limits one to operation at high frequency (~ 1 KHz) as opposed to the unipolar ramp operation used for ohmic heating in most tokamaks. A power supply for this coil was designed and built by the author in 1995 and achieved plasma pulses comparable to those produced by the 3 kW magnetron. The current is driven by a full bridge inverter attached to a 360 V, 300 A DC power supply. The switches are Darlington 600 V, 300 A BJTs borrowed from the current regulation switching boards inside the beam supplies. The output of the bridge is attached to the ohmic coil in series with a large capacitor. The coil and the capacitor serve as an LC filter for a stair-step output of the inverter. The stair-step pattern has been chosen because it can be timed so that it contains no third harmonic, and thus most energy is delivered to the fundamental mode of the LC. It should be noted that the high frequency of the LC resonator required that the BJT switches be snubbed for both turn on and turn off to prevent the switching losses from overheating the transistors.

2.1.4 Diagnostics

A radially scanning Langmuir probe is available to take plasma profiles. The tip can be swept in potential using a Kepco bipolar amplifier module connected to a triangle function generator. The probe is driven by a chain-connected stepper motor which can drive the probe at about 20 cm/s. Thus a 3 second shot is long enough to gather a complete radial density profile. A box has been built to analyze the voltage-current characteristic and send signals to a digitizer via an optical-isolated amplifier.

A gridded energy analyzer was recently added [*Meredith, 1997*]. The analyzer consists of a number of grids biased to various potentials in order to allow one to determine the energy distribution of the ions and the electrons in the plasma. The energy analyzer can be placed manually to a particular radial location, allowing one to crudely deduce energy distribution as a function of radial location.

In addition to the two plasma diagnostics mentioned above, a Rogowski coil has been wound and has been wrapped around the exterior of the chamber to allow one to measure plasma current. Furthermore, several loops of coax cable have been wound around the chamber to diagnose the ohmic coil-produced dipole magnetic field.

2.1.5 Data acquisition and control

Data acquisition and control are handled by two computers in the control room. One computer controls several CAMAC crates in the cell. The crates contain several digitizers—a 200 Hz digitizer for logging power supply voltage and current values, a 10 KHz digitizer for digitizing slow time-scale probe signals, and a pair of 4 MHz digitizers for the fast time-scale signals. The CAMAC crates are addressed via a GPIB interface consisting of a module in the rightmost slot of the crates. This module is connected to a card in the control room computer via a fiber optic link.

The experiment is controlled by a Programmable Logic Controller (PLC) residing in the cell. The PLC features some 96 digital outputs, 32 digital inputs, and 16 analog 12-bit outputs. The PLC contains an onboard program which can be modified using a terminal in the control room. In addition to being a programming console, the

terminal can display machine status information (such as interlocks) gathered by the PLC digital input terminals. During machine operation, the PLC environment is hidden behind a GUI user interface, allowing one to set up parameters for a plasma shot in a matter of seconds.

2.2 Wave launcher

The experiment that is described in this thesis involves two basic components: a high-power whistler wave launcher and a two-probe plasma diagnostic. The antenna acts as a source of whistlers, and the probes will diagnose the effects of the whistlers on the plasma (e.g., generation of lower hybrid waves and or other plasma modes). These components will be described, starting with the wave launching antenna.

Note that beginning at this point, and until the end of chapter 3, all construction, commissioning and experimental work was carried out by the author, unless otherwise noted.

2.2.1 Antenna design

An antenna was needed to launch waves along the field of the VTF machine. The simplest way to launch along the field is to place an antenna inside the plasma and aim it toroidally. However, such an in-situ antenna has to be designed with a small cross-sectional area so that the electron beam system can operate in a normal manner.

In choosing antennas, it was necessary to weigh issues of small cross-sectional area, high gain, favorable radiation impedance in a plasma, controllability of launching polarization, simplicity of construction, sturdiness in the beam plasma, and so forth. There was also the consideration that a bounded plasma, such as found in the laboratory experiment, would tend to increase the gain of an antenna because of its ability to duct whistler radiation. This property is discussed at length in appendix B.

A simple pair of crossed dipoles appeared to be the best compromise in face of meeting the requirements in the time available. A significant factor in choosing a dipole over a higher gain, more complicated antenna, had to do with the fact that

dipole radiation impedance behavior in plasma has been well-studied [*Balmain*, 1962; *Balmain*, 1969; *Bhat and Rao*, 1973]. The high-gain properties of a complicated antenna may not hold in plasma media, and nor would the radiation impedance necessarily be well-behaved.

A pair of crossed-dipoles were needed in order to launch into the whistler mode. Phasing the antennas 90 degrees from each other allows one to launch strictly right-hand circularly polarized waves. One could also launch linearly polarized waves with a single dipole and allow the left-hand circularly polarized component to attenuate in the plasma. However, this does not make good use of the available amplifier power.

Consider the radiation impedance a dipole oriented perpendicular to the magnetic field [*Balmain*, 1962]:

$$Z = \frac{a}{i\omega 2\pi\epsilon_0(1 + \chi_{\perp})L} \left(\log \frac{L}{\rho} - 1 - \log \frac{a+1}{2} \right) \quad (2.1)$$

where $2L$ is the length of the dipole, 2ρ is the thickness of the dipole wires and

$$a = \pm \sqrt{\frac{1 + \chi_{\perp}}{1 + \chi_{\parallel}}} \quad (2.2)$$

where the sign is taken such that the real part of a is positive.

After some inspection, it becomes clear that for the parameters of this experiment:

$$\frac{\omega_{pe}}{2\pi} \sim 2 - 8 \text{ GHz} \quad (2.3)$$

$$\frac{\omega_{ce}}{2\pi} \sim 2 - 3 \text{ GHz} \quad (2.4)$$

$$\frac{\omega}{2\pi} \sim 30 - 60 \text{ MHz} \quad (2.5)$$

that the real part of the impedance for reasonable values of L and ρ would be rather small. Thus the motivation was to make the ratio of L/ρ as large as possible, without sacrificing sturdiness. Second, it was desirable to make L as large as possible while still allowing the antenna to fit inside the machine.

Finally, it was also desirable that the metal antenna arms be DC-isolated from

the plasma to prevent them from drawing current from the plasma due to particle flux impinging on the metal antenna arms.

These problems were dealt with in the following manner. First, it was decided to enclose the dipole arms inside rigid ceramic tubes. This would serve to keep the arms steady and straight and provide electrical isolation between the metals arms of the antenna and the plasma. The four arms needed to be attached together, along with a ceramic tube containing coax lines feeding the antenna. This was accomplished using a small octagonal aluminum box, which was also isolated from the conductors joining the antenna arms.

Second, the wires forming the dipole arms did not have to be thick, as they were supported by the ceramic tubes. The wires only had to be thick enough to stay reasonably straight inside the ceramic tubes, and carry 1-2 amps of RF current during high power operation. 18 gauge (1.02 mm diameter) copper wire was chosen for this purpose. While 18-gauge had more than enough current-carrying capacity (25 m Ω /meter), it was discovered that smaller wire gauges tended to bend, tangle and break during the construction process.

Third, a practical limitation on the size of the antenna was imposed by the collection plate for the beams and the need to scan diagnostic probes in the midplane of the machine without falling into the toroidally projected plasma “shadow” of the antenna. Since the collection plate stuck downward from the roof of the chamber by 8” it was necessary that the entire antenna be less than 13” tall so that it could fit entirely in the plasma between the bottom of the collection plate and the midplane probes. The size of the antenna was maximized by rotating it so that it appeared as an “X”. In this orientation, the maximum length of the antenna arms was 9”.

2.2.2 Hardware Construction

The details of construction will now be described. Note that the procedure outlined in this section and in later sections does necessarily reflect the actually process used to arrive at the built system. Details of repeated assembling and disassembling, failed ideas, various machining techniques, vacuum cleaning preparation, and so on, have

been omitted.

The first item in the construction of any in-machine component is the mounting mechanism. For the purposes of the experiment, it was not necessary to retract the antenna since it was the only experiment in progress at the time. It was decided that a fixed support would be sufficient. A top port with a total of six half nipples was used for the support. A section of 1" pipe welded to a 2.75" diameter double-sided flange was located. Several holes were drilled between the outside circumference of the weld on the flange and the knife edge in order to allow for the circulation of air across the flange after being sealed with gaskets. The pipe was cut so to be long enough to extend 5" into the machine when mounted on the half-nipples. This meant that the pipe could hide behind the collection plate and thus it was acceptable to electrically attach the pipe to the grounded chamber as it would not be exposed to any plasma.

Please refer to figure 2-3 for the following discussion. A length of 0.375" outer diameter ceramic tubing was cut to connect the mounting pipe and the in-plasma octagonal antenna arm coupler. Since the ceramic was significantly smaller than the pipe, two collars were machined out of aluminum to fill the coaxial space between the ceramic tube and the metal mounting pipe. The collars were held in place on the ceramic tube by notching the ceramic with a diamond saw, and drilling and tapping holes for set screws on the collars. The set screws had to be ground down until they were flush with the outer surface of the collar, so that they would slide into the metal pipe. The metal pipe was then drilled and tapped at four points and set screws were inserted to fasten the aluminum collars in place. The entire pipe and ceramic was then inserted through one of the half nipples. The remaining part of the construction could be carried out with the double sided flange mounted on the port cover's half nipple.

The aluminum octagonal coupling box was machined out of a single piece of aluminum. First, a block of aluminum was cut to the smallest size that would ultimately allow the fastening of five 0.375" ceramic arms. The corners of the block were milled off until the block had the shape of a regular octagon. The octagonal block was then

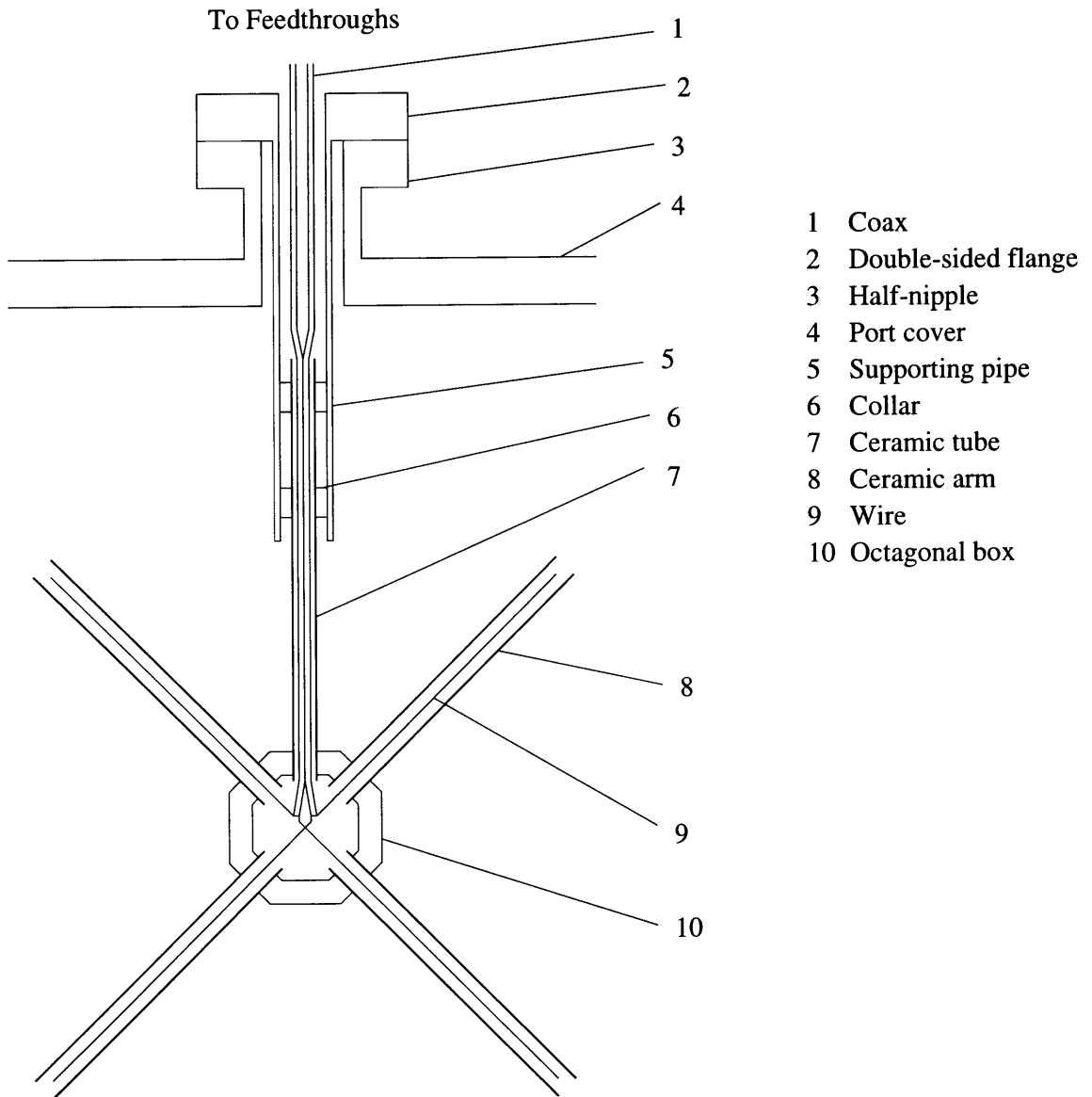


Figure 2-3: Schematic of antenna (not to scale).

hollowed out on the mill until the wall thickness was about 0.25". 0.375" holes were drilled in the center of the 45, 135, 225, and 315 degree sides to accommodate the ceramic pipe shields for the dipole arms. A fifth hole was drilled at 0 degrees in which to insert the ceramic tube which extended up to the supporting pipe. Smaller holes were drilled from the face of the octagon into the large holes for the ceramic arms. These holes were then tapped for set screws. Small notches were cut in each of the five ceramic arms at the appropriate locations to accept the set screws. The ceramic arms also had to be ground slightly on the diamond wheel because the holes at 315, 0 and 45 degrees brought the arms slightly closer together than was originally intended.

Since the box needed to be inserted into the plasma, a cover was needed to protect the coax/wire solder connections that would be inside the box. Furthermore, a cover would be needed for the aluminum faces of the box, as aluminum is unlikely to survive inside the plasma. Two octagonal covers were cut out of stainless steel. Holes were drilled in the covers and screw holes were drilled and tapped on both faces of the octagonal box.

For the electrical connections, 0.085" diameter copper semirigid coax was fed down through the main ceramic tube and into the octagonal coupling box. Once inside the box, the outer conductor of the coax was trimmed back using a Dremel tool and the teflon dielectric cut away with a razor blade, exposing the inner conductor. A length of 18-gauge wire was pushed through from one end of the ceramic arms and soldered onto the inner conductor. Another piece was inserted through the 180 degree opposite arm and soldered onto the outer conductor. The same process was repeated using the other coax for the other two arms. The wire arms were trimmed so that they were recessed about 1 cm from the end of the ceramic arms and would not be able to come into DC electrical contact with the plasma. Finally, to protect the box from accidentally making electrical contact with the coax, small pieces of mica were inserted between the solder connections and the octagonal aluminum face inside the hollowed-out region. Finally, the steel box cover was screwed in place using round head bolts. Two small washers were threaded on the bolts between the aluminum box and the steel cover, in order to space the cover and box, and minimize the thermal

conductivity between the two. The back cover was also attached in the same manner.

The construction then moved to the top of the port. Please refer to figure 2-4 for the following discussion. Some way was needed to feed the coax out of the vacuum. Normally, one would put SMA connectors on the coax and feed them out through an electrical vacuum feedthrough. Indeed, two such feedthroughs were available, but were earmarked for the receiving probes. Instead of investing \$500-\$1000 in new feedthroughs it was decided to try building some homemade feedthroughs. Some N-type instrument panel feedthroughs were taken from old equipment and adapted to work as vacuum electrical feedthroughs. The key feature was that the N-types had a collar for mounting on a instrument panel. Using a metal grinding wheel, this collar was cut down and smoothed in order to accept a small o-ring. A 0.75" hole was cut into a blank single-sided 2.75" flange. The adapter was inserted into this hole, with an o-ring pressed against the collar. It was found that the o-ring could be compressed by screwing on a nut to the threaded portion of the adapter. Unfortunately, at full compression, the nut was not threaded far enough to allow attachment of N-type cables or BNC adapters on the same threaded portion of the adapter. The solution was to put the single-sided flange on the lathe and bore out the flange to about half the original thickness of the flange and a diameter of just smaller than the knife edge. Now, when the nut was threaded on, it could thread on far enough so threads remained for the cable adapter. Finally, it was found after some trial and error that the o-ring compression could be made more uniform by placing a large washer at the base of the bored-out section, around the feedthrough, allowing the force from the nut to be applied evenly on the flange.

The feedthrough design was then vacuum tested. Even though the dielectric seal between the inner and outer conductors was not designed for vacuum, it was presumed that it would hold a reasonable vacuum. The feedthrough was extensively cleaned with Scotchbrite and the assembled electrical feedthrough was mounted on a hand valve attached to the machine. The handvalve was opened to the chamber and the vacuum pumps were left pumping on the feedthrough for several days. The equilibrium chamber pressure with the feedthrough in place was 2×10^{-5} torr, which

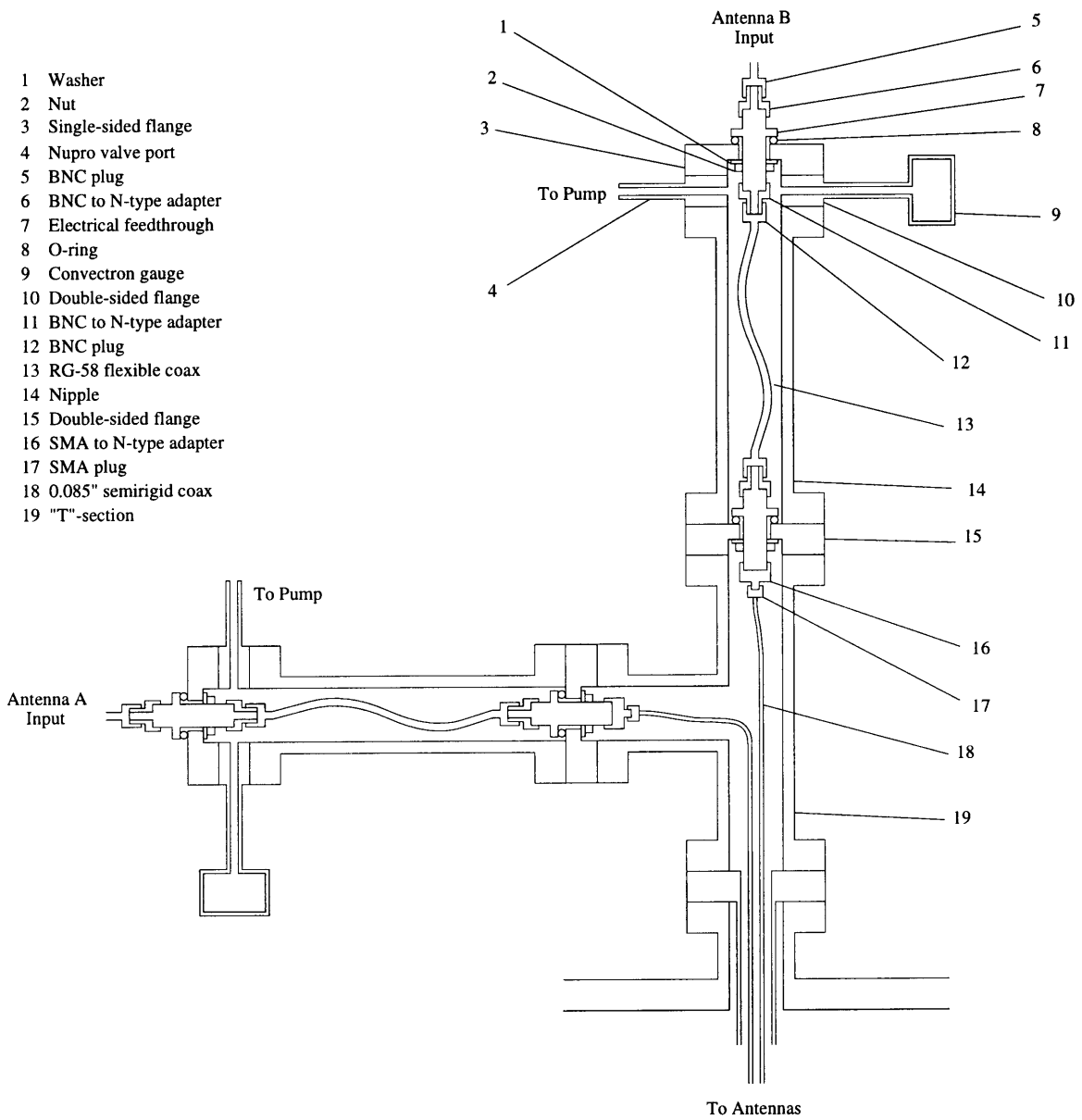


Figure 2-4: Schematic of homemade feedthroughs (not to scale).

is about two orders of magnitude above nominal base pressure. It was decided that to improve the performance of the seals, one needed to put two of them in series, as shown in figure 2-4 and then pump on the volume between the feedthroughs. The idea is that the leak rate through an interface is proportional to the pressure difference across the interface. If two seals are placed in series between the atmospheric pressure and the chamber vacuum, and the intermediate volume is pumped, the leak rate of the outer seal is only as small as the leak rate of a single seal on the machine. However, the inner seal sees a much smaller pressure difference—basically the difference of 2×10^{-5} torr and base pressure inside the chamber, and as a result has a far smaller leak rate than the outer seal.

This concept was used for the antenna vacuum seal. Since only one feedthrough would fit on a 2.75" flange, a vacuum "T" section was placed on top of the double-sided flange (to which the metal support pipe was welded). The individual coax sections were bent to travel out each of the two apertures of the "T". The SMA connectors were soldered onto the semirigid coax and female SMA to male N-type adapters were attached. One more feedthrough assembly was built on a single-sided flange for the second coax, and then two more feedthroughs were built on double-sided flanges to serve as the inner feedthroughs as shown in figure 2-4. The four feedthroughs were attached as shown, with 5" nipples separating the in-series flanges.

A 7" section of RG-174 was prepared with BNC connectors crimped on either end. The rubber shield on the outside of the coax was stripped off because it would otherwise outgas when the volume between the feedthroughs was being pumped. RG-174 was chosen because the section of coax between the feedthroughs had to be very flexible. The reason is that the cable had to have compliance during the attachment of the two feedthroughs to the 5" nipples, as there was no way to screw this cable on to the feedthroughs after the feedthroughs had been bolted onto the nipple.

It was later found that the RG-174 was not sufficient to carry 75 W at 60 MHz. The RG-174 was subsequently replaced with RG-58. Since the semirigid coax on the inside of the inner feedthrough had virtually no linear compliance, a rather roundabout method had to be devised for removing the 5" nipple without unsealing the gasket

connection between the “T” and the inner feedthrough. If one did not pursue this method, then it would otherwise be necessary to take apart the entire antenna to replace the copper gasket making this particular seal.

The double-sided flange on the outer end of the half nipple contained two welded-on components. One was a hand-operated Nupro valve port, which would allow the intermediate volume to be pumped. The other was a convectron gauge, which could be attached to gauges on the vacuum stand to monitor the pressure of the intermediate volume.

The antenna was now complete and ready for insertion into the machine. The location of 220 degrees was chosen for the antenna because it was well out of the way of existing diagnostics. However, during the vacuum break to insert the antenna, it was discovered that with the antenna mounted on the port cover, it was not possible to maneuver the port cover into place on the top of the machine. The reason was that the TF arms converge, so that normally port covers have to be angled downward toward the center of the torus during insertion. Unfortunately, with the antenna in place, this could not be done.

The solution was to remove the 2 outer ceramic arms of the crossed-dipole antenna and bend the 18 gauge wire inward. This required disassembly of the octagonal box, and subsequent reassembly inside the chamber. This was performed at the risk of disturbing the solder electrical connections inside the octagonal box during the bending of the 18-gauge. A electrical check of the conductor was necessary once the antenna was inside the machine.

During pumpdown following the vacuum break, outside connections could be made. The first connection was rubber hose to pump out the intermediate volumes between the feedthroughs. Rubber hose was hoseclamped onto the Nupro valves and run down to a small roughing pump located on the vacuum stand. A T-connector was used at the location of the port cover so that both intermediate volumes could be pumped with the same pump. Pressure of the intermediate volume was monitored using the convectron gauge. The pressure after a couple minutes was 100 mtorr and then 10 mtorr after several hours. This intermediate volume pressure was easily

low enough to render the feedthrough leak rate negligible. However, the rather high steady state pressure resulted in the intermediate volume vacuum pump evaporating a fair amount of oil—the oil needed to be refilled every 2 weeks.

Photographs of the completed antenna are shown from inside the chamber in figure 2-5, and outside the chamber in figure 2-6.

2.2.3 Electrical connections

A large capacitor was placed in series with both antennas for safety reasons. Even though the arms of the dipoles are insulated from the plasma by ceramic arms, it is still a good idea to put some DC electrical isolation between the transmitters and the antennas in order to protect the transmitters on the occasion that the ceramic arms were to break and the antenna arms come into contact with the plasma. The value of these capacitors were chosen so that they appeared as a short within the operating range of the antennas (typically 30-60 MHz).

RG-58 cable was used to extend the cables down to the transmitters. RG-58 was used because it is power rated at around 100 W at 100 MHz, which well-exceeds the capabilities of the power amplifiers that were going to be used. Since the antennas were not tuned to 50Ω , it was necessary to install some sort of tuning mechanism on the ends of the antenna leads. For ease of adjustment it was decided to put the tuning mechanisms at the location of the power amplifiers, as opposed to the location of the antennas, as is usually done. The reason is that it would be difficult and exasperating to repeatedly access the tuners if they were located at the port cover on top of the machine. The one item of concern was that the cables running from the antennas be of the same length, so that 90-degree phasing of the antennas can be easily implemented to launch circularly polarized waves.

It was decided that the easiest and most flexible way to tune the antennas would be to place a stub tuner some distance from the antenna. The distance of the stub from the antenna and the length of the stub would provide the two degrees of freedom necessary to match the complex impedance of the antenna. In fact, this is the method that is used in megawatt-level ICRH schemes for tokamak experiments. There are

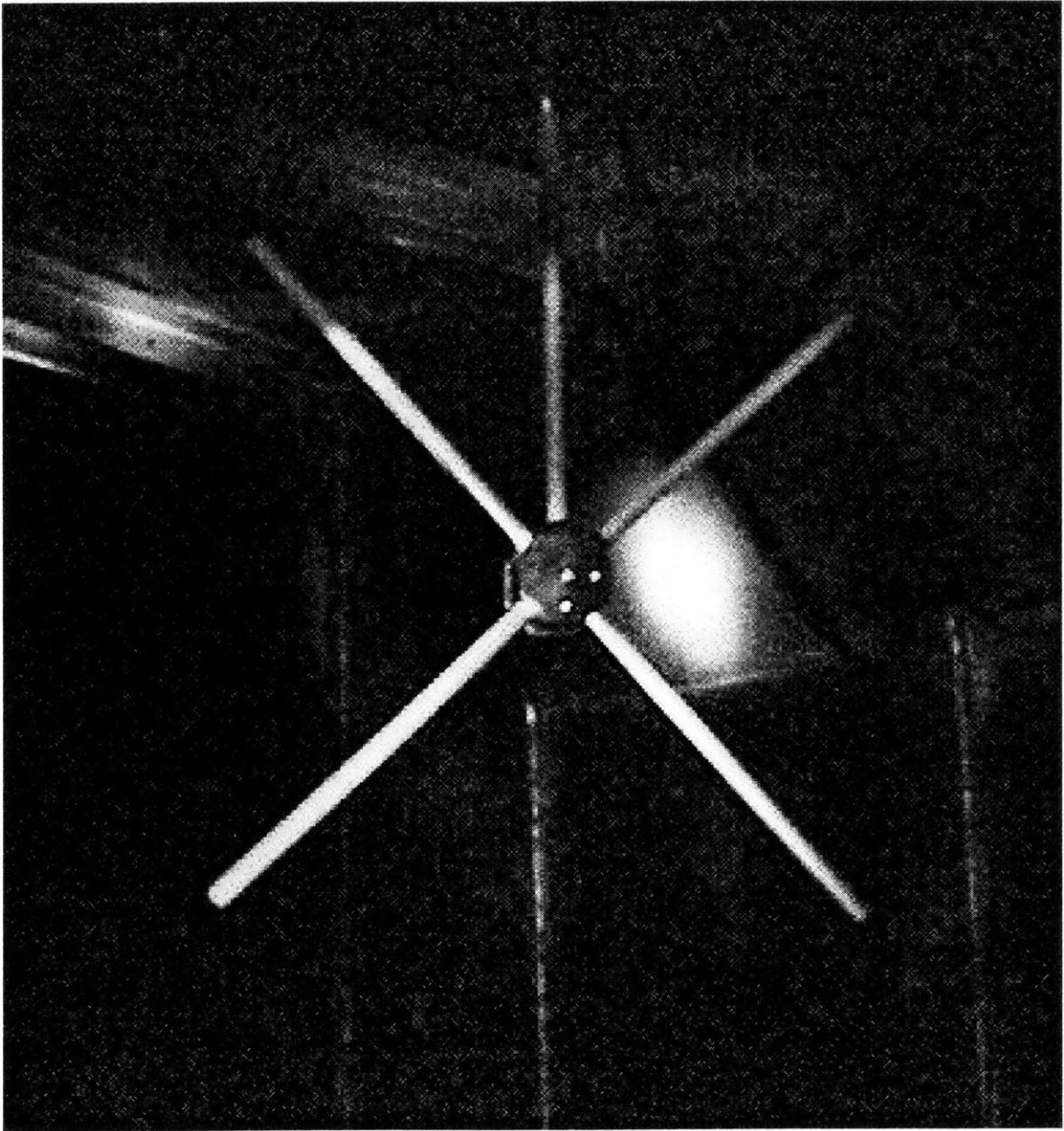


Figure 2-5: The crossed-dipole antenna, as seen from inside the chamber.

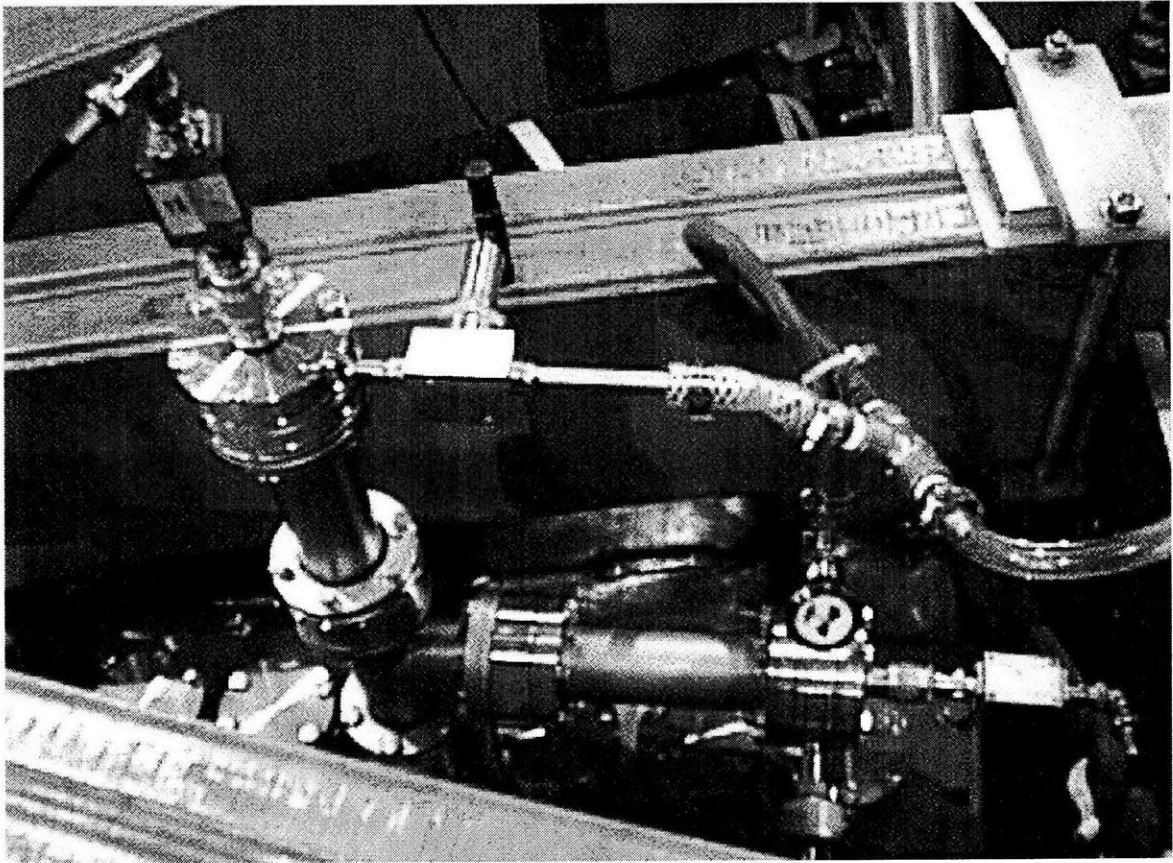


Figure 2-6: The external feedthroughs for the machine-mounted antenna.

several ways to determine the appropriate lengths of the stubs:

1) One can attach an RF network analyzer to the impedance to be measured and select the complex reflection coefficient to be plotted on the Γ -plane. One then adds length of cable to the transmission line between the analyzer and the antenna until the real part of the antenna admittance (conductance) is $1/(50 \Omega)$. Then one places a stub (terminated by a short) in parallel with the line, to eliminate the imaginary part (susceptance) of the admittance. This is a systematic procedure, which is most easily done with the network analyzer set to display admittance co-ordinates. The problem with this method is that it could not be carried out with the plasma in place because the provider of the network analyzer would not permit it. Therefore one is somewhat forced to tune the antennas for vacuum and then see if the tuning works in plasma using some other method.

2) In lieu of an RF network analyzer, one can devise an equivalent to an analyzer using power splitter and mixer modules. Such a device is shown in figure 2-7. The magnitude of the reflection coefficient Γ is displayed at port A and the phase of Γ is displayed at port B. This device is useful for checking whether the vacuum tuning produced by using the network analyzer is good in a plasma. One can attach the outputs A or B into a digitizer whose data acquisition window is synchronized to the plasma pulse and record the changes in the magnitude and phase of Γ as the plasma is formed and/or moved around with respect to the antennas.

3) A completely different way to measure Γ during the plasma pulse is to attempt to measure the voltage standing pattern on the transmission line. A method for doing this is shown in figure 2-8. The size of the voltage standing wave is read as the voltage across the large-valued resistor in the circuit diagram. This output can be digitized during the plasma pulse and recorded on a computer. Further plasma pulses can be made with additional lengths of cable placed on the transmission line in order to sample the standing wave at multiple points. The basic problem with this method is that it is time consuming. One must run a lot of plasma shots in order to collect the data.

All three methods were considered. First, the RF network analyzer was borrowed

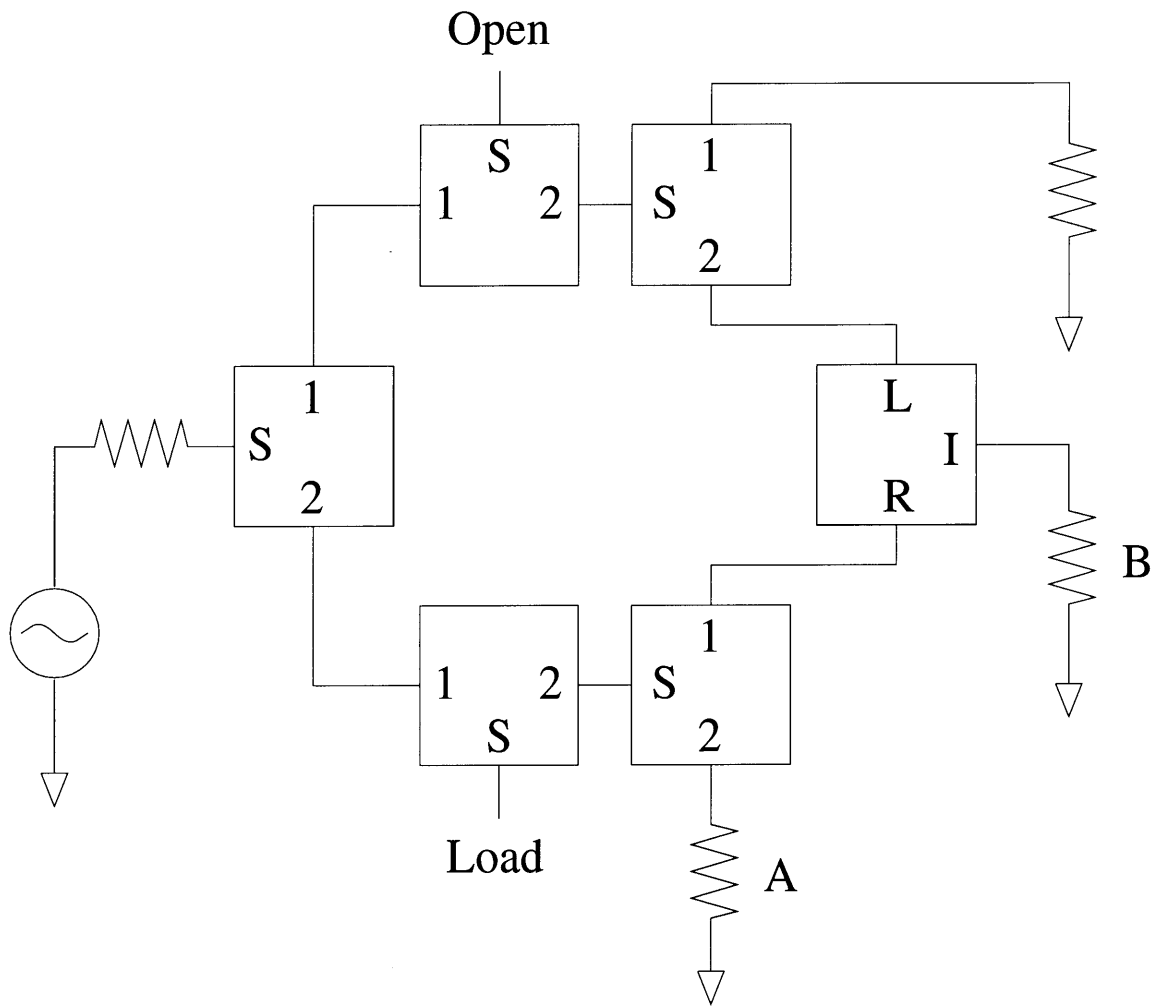


Figure 2-7: Crude realization of a network analyzer. “S12” boxes are power splitters, “LIR” boxes are mixers, and all resistors are 50 Ω .

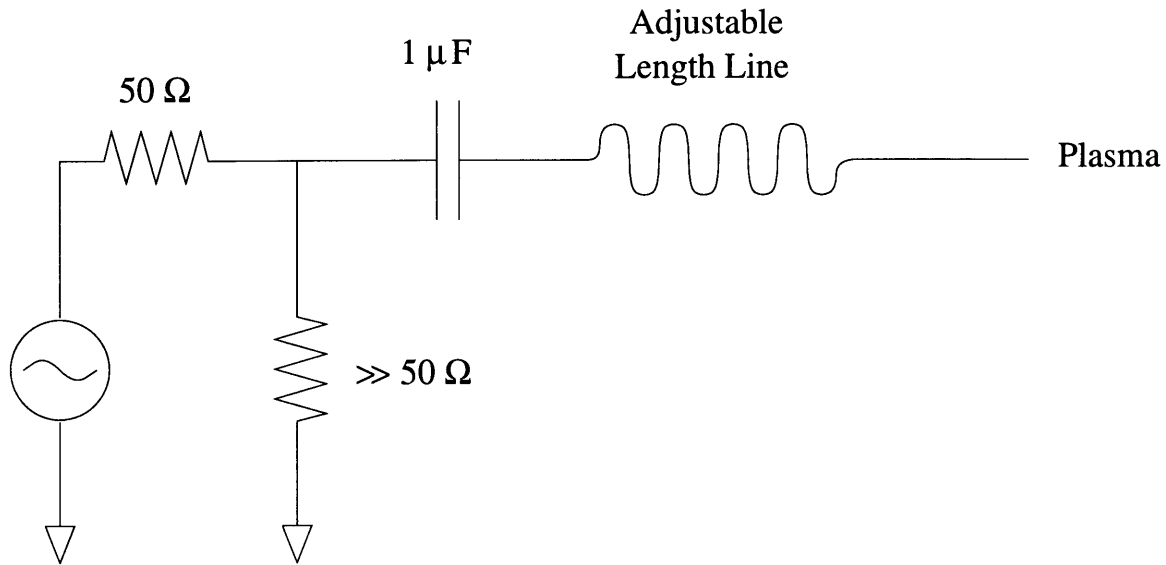


Figure 2-8: A method for measuring the voltage standing wave.

from a fellow experimentalist and used to tune the antennas in vacuum. The vacuum impedances were $5.0+48i \Omega$ for antenna A and $4.5+47i \Omega$ for antenna B. Lengths of RG-58 cable were then added to the line between the antennas and the amplifier until the conductance was $1/(50 \Omega)$ at 60 MHz. The tuning is actually fairly sensitive to the lengths of the cables, so for a couple small length adjustments it was necessary to add gender conversion adapters to get the correct length. This tuning is sensitive because the antenna radiation resistances are very small in vacuum. As the radiation resistance gets lower it is hard to accurately set the conductance at exactly $1/(50 \Omega)$, because the lines of constant conductance rapidly converge on the Smith chart at the point of infinite admittance. Next, a short stub was assembled to eliminate the susceptance of the antenna line. In practice, the stub was quite short, so again the technique of connecting together gender conversion adapters was used. A wire was soldered from the center to outer conductor on the final connector, terminating the stub with a short. This procedure was applied for both antennas and impedances after tuning were $66+1.0i \Omega$ for antenna A and $68+11i \Omega$ for antenna B, which translate to reflection coefficients of $0.14\exp(-0.05i)$ and $0.18\exp(0.44i)$, respectively. While the tunings are certainly not exactly matched to 50Ω , they do represent a vast improvement over the untuned antennas, using a fairly crude tuning apparatus.

The next step was to verify that this tuning was good in a plasma. Since the size of the dipole was somewhat smaller than desirable, even in plasma media, it was not known how good the tuning would be once the plasma was turned on. To test the tuning, an experiment was devised following method (2), since method (1) could not be used for plasma measurements. The plan was to sweep a plasma pass the antenna and measure the properties of Γ as the sweep progressed. A function generator was attached to the current level control on the toroidal field power supply and a slow sine wave was fed in. The field was swept over a range of approximately 4–9 kA. This effectively swept the RF resonance over the major radius of the machine and served to move the bulk of the plasma through the major radius location of the antennas. During this sweeping the reflection coefficient was recorded by running the outputs of the apparatus in figure 2-7 into a 10 kHz digitizer.

Since the goal was to maximize the fraction of power transmitted, which scales as $1 - |\Gamma|^2$, the primary item of interest here is the magnitude of Γ . Figures 2-9 and 2-10 show $|\Gamma|$ for the antennas A and B, respectively, as a function of toroidal field current.

Note that the plasma is located near the inside wall of the chamber at around 4 kA toroidal field current, and the plasma moves out into the port extensions above 8 kA.

The following features appear and are expected in each of the data sets:

1. When the plasma resonance vanishes through the inside wall of the machine, the measured reflection coefficient agrees with the vacuum value.
2. When the magnetic field is very high, and the plasma resonance is placed out in the port extensions, the tuning approaches its vacuum value.
3. When the plasma is in the location of the antennas, the tuning experiences irregular changes.

The important observation in these figures is that $|\Gamma|$ never exceeds a value of 0.4. This means that the fraction of power transmitted is in excess of about 85% for both antennas.

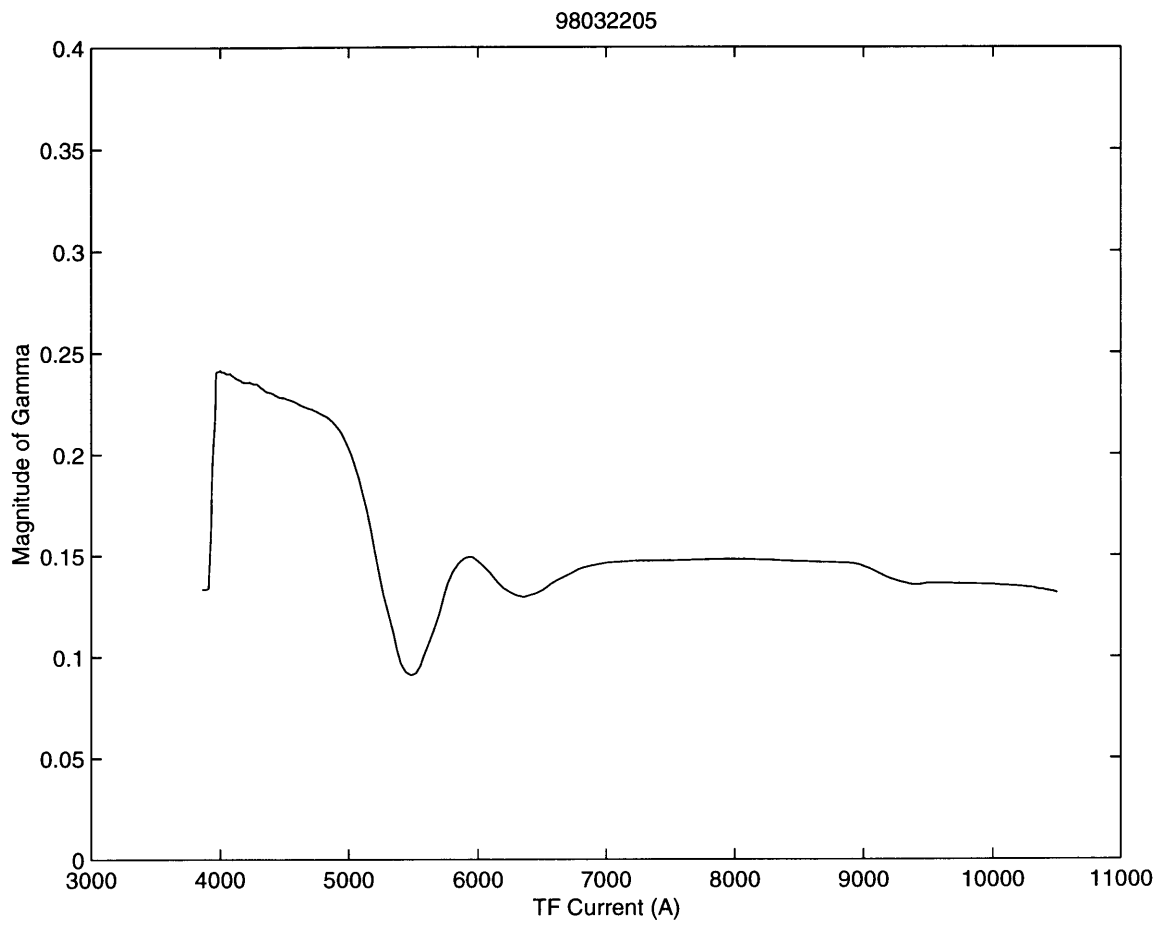


Figure 2-9: Magnitude of gamma of antenna A as a function of toroidal field strength.

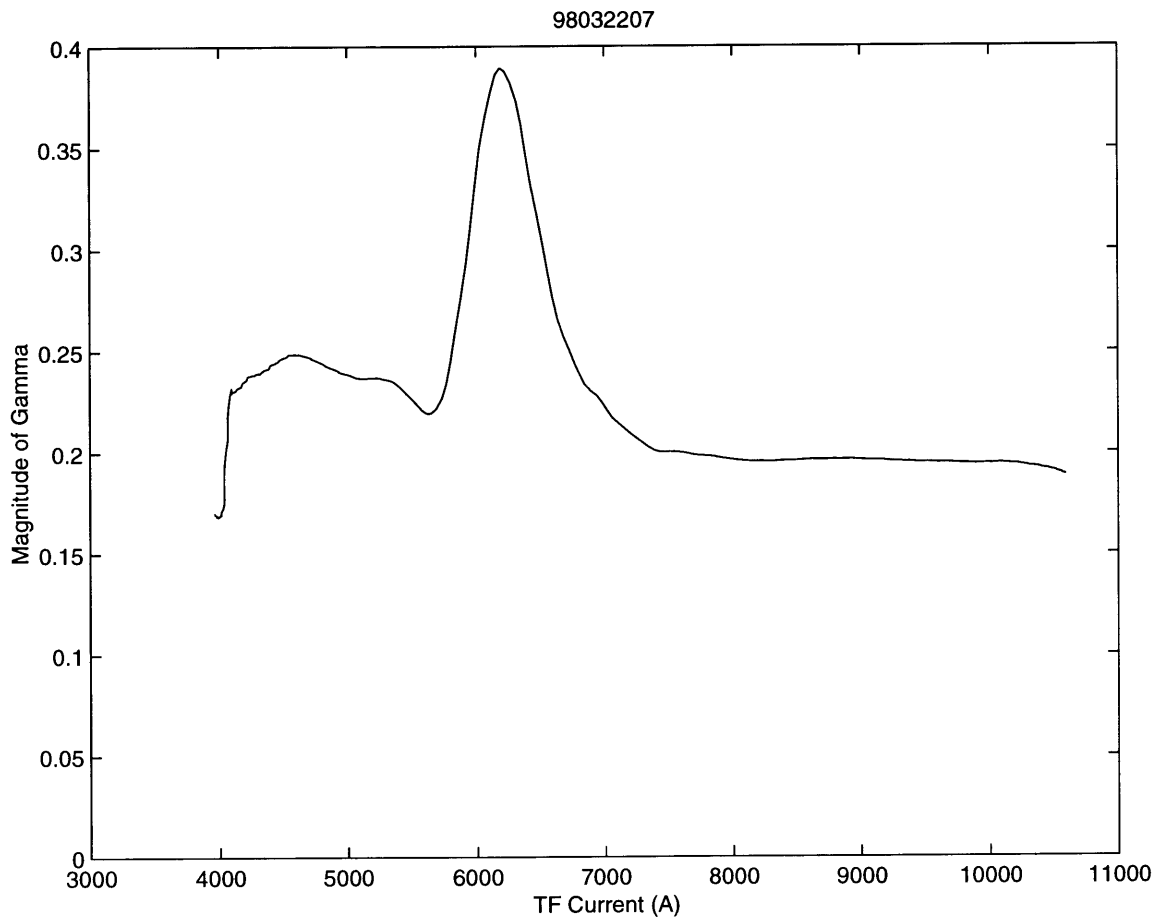


Figure 2-10: Magnitude of gamma of antenna B as a function of toroidal field strength.

Method (3) could have also been used in lieu of method (2). However, method (3) tends to be time consuming because one must make a cable length change after every measurement, and if one is doing a measurement in plasma, then the tuning must stay the same from shot to shot. However, an example will be presented here of a voltage standing wave pattern that was measured at 30 MHz. Antenna A was hooked up to the voltage standing wave-measuring device shown in figure 2-8. A total of 24 different lengths of cables were substituted in order to sample the voltage standing wave ratio at a distance increments of 9". These lengths of cables were put together by assembling 5 cables of lengths 9", 18", 3', 6' and 6' in various ways.

Measurements of the voltage standing wave pattern on the antenna A line were made in vacuum and in plasma at these 24 locations, and the deduced standing wave patterns are shown in figure 2-11. Note that the minima in the patterns are critical to determining the size of the voltage standing wave ratio (VSWR), and the patterns as sampled do not accurately give a value for these minima. Therefore, there was a need to continuously sweep the length of the transmission line through these minima in order to correctly deduce this minimum value. A section of "trombone" line was borrowed, namely a sliding U-section which would allow the length of the transmission line to be varied continuously. A section of this trombone line was inserted into the line and clamped to a table. A string was tied to the sliding section and then passed through a hole in the interlock fence, allowing one to pull the section out during a shot and yet have the string-puller reside outside the interlock fence. This procedure was carried out during a shot to assess the size of the minima suggested (but not accurately represented) in figure 2-11. The resulting minima was found and the VSWR was read to be 22 in vacuum and 15 in a plasma. The phase of Γ could be deduced from looking at the distance of the first minimum in the pattern l_{min} to the load being measured using the well known relation,

$$\Gamma = -|\Gamma|e^{j2kl_{min}} \quad (2.6)$$

where k is the wavenumber in the transmission line. The quantity kl_{min} can be

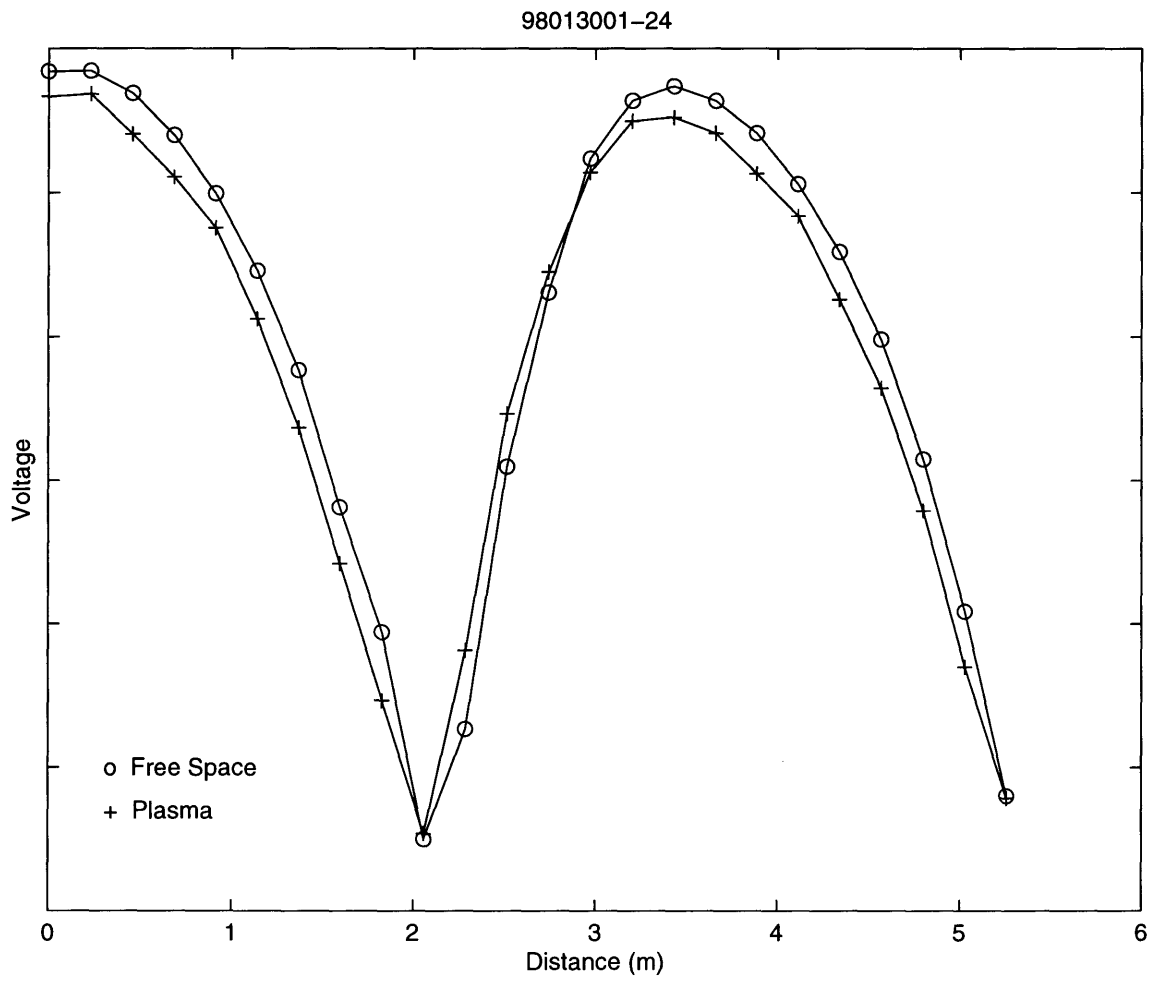


Figure 2-11: Voltage standing wave pattern in cable.

deduced if one knows the frequency of the carrier wave and the amount of time it takes for the waves to travel the distance l_{min} inside the cable. This time can be measured using a pulse generator and looking at the time for reflection from the load (a pulse can be used since the cable is dispersionless at normal RF frequencies).

Once the tuning for the individual antennas was carried out, the antennas could be hooked to the amplifiers. Two amplifiers were located for the experiment. Two amplifiers is much better than one amplifier because then there is no need for a high-power splitter (which the lab does not own). Unfortunately, the two amplifiers were not quite matched. One could put out 150 W over the range 0.1–35 MHz and the other could put out 80 W over the range 0.25–105 MHz. Thus the range of operation with both amplifiers was limited to about 40 MHz. If one wanted to explore above these frequencies, then one was limited to the single 80 W amplifier. When using the single amplifier, an alternative to using the power splitter was to use a simple “T” and then place further stub tuners to correct the impedance mismatch introduced by the “T”. This is the approach that was carried out for the single amplifier at 60 MHz. The results of using method (2) to test this configuration is shown in figure 2-12.

However, it turned out that the tuning stub positions and lengths at 60 MHz also, by fortunate coincidence, produced good tuning at 36.14 MHz. For example, with the above tunings at 60 MHz, the tuning at 36.14 MHz was $42+2.8i \Omega$ for antenna A and $38+6.8i \Omega$ for antenna B. Therefore one could operate at either frequency without the inconvenience of retuning. To run at 60 MHz, one attaches the two lines in parallel with the “T” connector, and then attaches a stub to tune the parallel combination of the two antennas. If one wants to run at 36.14 MHz using both amplifiers, one removes the parallel-tuning stub and simply plugs the antennas into the amplifiers.

On the input side of the amplifiers, both amplifiers are fed from a single oscillator. The RF signal passes through a power splitter, and one half travels to the small amplifier and the other half travels through a set of attenuators before travelling into the large amplifier. The attenuators are needed to balance the amplitude of the output signals, as the larger amplifier has a larger gain than the smaller amplifier. There is also one additional problem that needs to be addressed here. The antennas

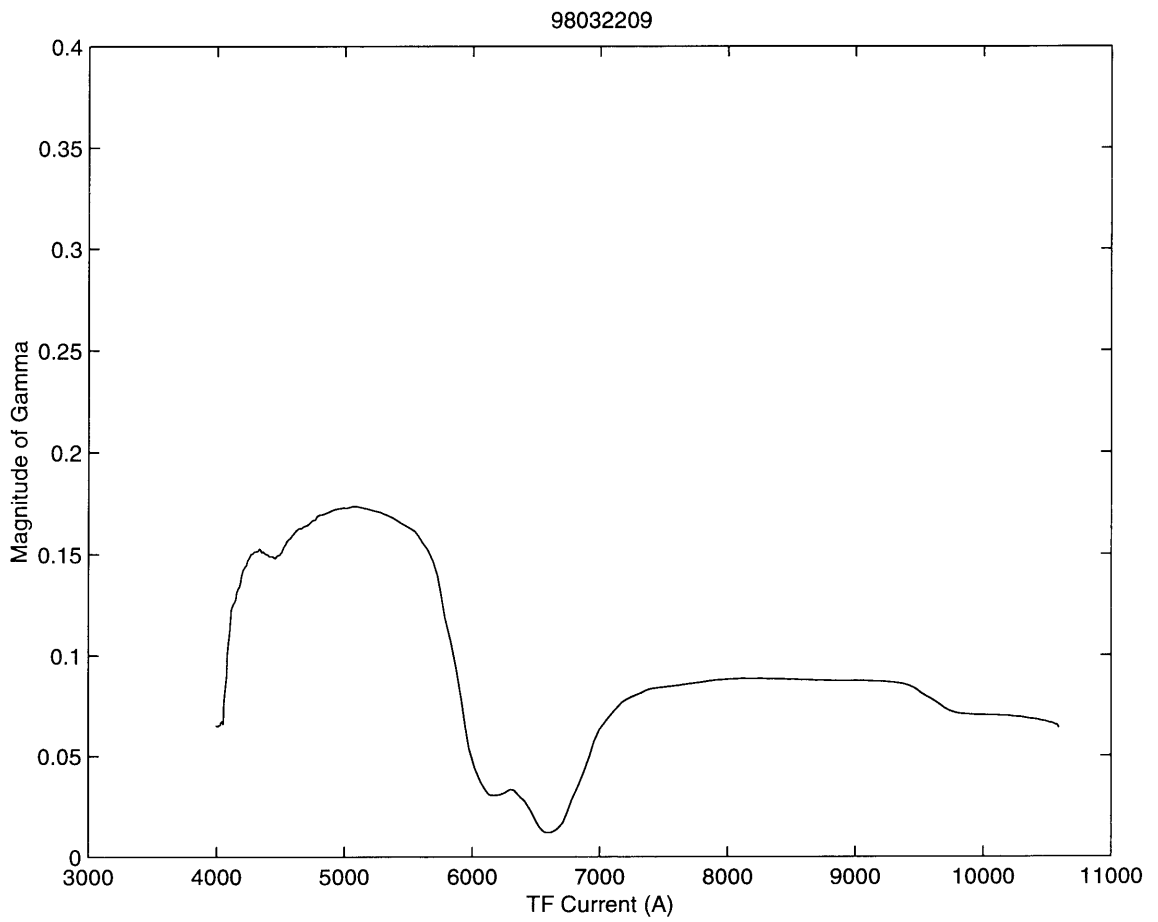


Figure 2-12: Magnitude of gamma of parallel combination of antennas A and B, as a function of toroidal field strength.

needed to be phased 90 degrees apart in order to launch a wave into the whistler mode (right-hand circularly polarized). Therefore a 90 degree delay cable had to be added at some point.

In the case of operation with two amplifiers at 36.14 MHz, the delay cable would be added at the point where the signal to the delayed antenna (antenna A) enters the RF amplifier. Since there are attenuators on this amplifier (the larger of the two), measurements had to be made to ensure that the combination of a delay cable and the attenuators led to a phase delay of 90 degrees.

Alternatively, when using a single amplifier at 60 MHz, the 90 degrees phasing would have to be incorporated on the high power side, after the power split is made. One must remember to do this *before* creating the stub tuner that will tune the parallel combination of the two antennas.

In the end, both procedures were tried. The higher frequency tended to favor operation in the electrom beam-generated plasma, because of the values of ω_{lh} involved (30–60 MHz). The lower frequency favored operation in ECRH plasmas, with its characteristically lower value of ω_{lh} (15-30 MHz).

This completes the transmitter section of the hardware assembly.

2.3 Diagnostic

One of the luxuries of lab experiments is the ability of the experimentalist to separate temporal and spatial components of the wavefields of interest. In the lab experiments, temporal variations can be adequately observed by a single point data source whereas spatial variation observations require at least two point data sources. These point data sources can be any observable that bears the wavefield structure of interest. These typically are scalar measurements of density or voltage fluctuations.

There were two basic diagnostic design goals. The first was to select a probe design that would be able to measure RF wavefields in the frequency range of interest (20-80 MHz). The second was to determine a deployment of probe pairs that would allow one to measure the three-dimensional structure of the wavefields in an efficient

manner.

2.3.1 Probe characteristic

Typically, metal plasma probes are used in one of two modes. In the first mode, the DC probe current is fixed (usually at zero) and the voltage is allowed to vary. This is called the “floating” probe mode, because the DC probe voltage floats to the so-called floating potential of the plasma. In this mode, RF plasma voltage fluctuations couple to probe voltage fluctuations. At this operating point, it can be shown that the probe voltage fluctuations are proportional to the RF plasma voltage fluctuations.

In the second mode, the DC probe voltage is fixed (usually at a large negative voltage) and the probe current is allowed to vary. This is called the “biased” probe mode. In this mode, RF plasma *density* fluctuations couple to probe current fluctuations. At this operating point, the probe current fluctuations are proportional to plasma density variations.

Let us examine both of the methods in more detail, because both will be tried for the experiments.

The floating probe

The probe in question is a floating potential device. Therefore it accepts zero DC current from the plasma and a linearized small-signal analysis of the probe can start directly with the incremental circuit model of the probe. Kirchhoff’s voltage law for this circuit is

$$v_r + v_c = -i_p R - \frac{1}{C} \int i_p dt = v_{pp} + v_p \quad (2.7)$$

where v_r is the incremental voltage across the sense resistor, v_c is the incremental voltage across the DC block, i_p is the incremental current leaving the probe, R is the resistance of the sense resistor, C is the capacitance of the DC block, v_{pp} is the incremental probe to plasma voltage, and v_p is the plasma potential fluctuation. Let us assume that the frequency of the incremental current is sufficiently large to render the integral term zero (but small enough to ensure that the I-V characteristic

is time-invariant—generally less than ω_{pi}). Then

$$-i_p R = v_{pp} + v_p. \quad (2.8)$$

The constitutive relation for the probe is [Hutchinson, 1987]

$$i_P = B \exp\left(\frac{eV_{PP}}{KT_e}\right) - i_S \quad (2.9)$$

where i_P is the probe current, B is an inconsequential parameter, v_{PP} is the total probe to plasma potential, K is Boltzmann's constant, T_e is the electron temperature, and i_S is the so-called ion saturation current. The linearized incremental probe current is therefore

$$i_p = v_{pp} \left[\frac{di_P}{dV_{PP}} \right]_{V_{PP}} = v_{pp} \frac{eB}{KT_e} \exp\left(\frac{eV_{PP}}{KT_e}\right) \quad (2.10)$$

where V_{PP} is the probe to plasma operating point voltage. If we assume that $i_s \ll I_S$ (i.e., the fluctuations in i_S can be ignored in the linearization) then V_{PP} can be found to be $\frac{KT_e}{e} \log \frac{I_s}{B}$ from the constitutive relation. Therefore

$$i_p = v_{pp} \frac{eI_s}{KT_e} = (-i_p R - v_p) \frac{eI_s}{KT_e}, \quad (2.11)$$

so we have

$$i_p = -\frac{\frac{eI_s}{KT_e}}{1 + \frac{eI_s R}{KT_e}} v_p. \quad (2.12)$$

Since $v_r = -i_p R$, we finally find that

$$v_p = \frac{1 + \frac{eI_s R}{KT_e}}{\frac{eI_s R}{KT_e}} v_r \quad (2.13)$$

This means that $v_r \propto v_p$, or in other words, the probe voltage fluctuations are proportional to the plasma voltage fluctuations. We say that the plasma has a source impedance of

$$R_p = \frac{KT_e}{eI_s} \quad (2.14)$$

because (2.13) suggests v_p being divided by a voltage divider consisting of R_p and R .

The biased probe

Again, the constitutive relation for the probe is

$$i_P = B \exp\left(\frac{e v_{PP}}{K T_e}\right) - i_S. \quad (2.15)$$

In the limit that the probe is biased negatively, $v_{PP} \ll -\frac{K T_e}{e}$, the probe characteristic is simply

$$i_P = -i_S \quad (2.16)$$

so that the probe tip looks like a current source of size i_S . i_S involves the saturation current due to the background plasma density N and the RF plasma density fluctuation n . This is expressed in the usual formula for the saturation current [Hutchinson, 1987],

$$i_S = 0.6(N + n)e v_S A \quad (2.17)$$

where e is the electron charge, v_S is the sound speed ($\sqrt{T_e/m_i}$) and A is the total probe area. Therefore $-i_p = i_s \propto n$, or in other words, the probe current fluctuations are proportional to the plasma density fluctuations. Circuit-speaking, we would say that the plasma has infinite source impedance, because the current i_p does not depend on the size of the sense resistor R .

Testing the probe response

While the biased mode offers infinite plasma source impedance, the floating mode has only finite plasma source impedance R_p and therefore offers a quantity that can be used to check the validity of the above formulation.

Experiments were performed with a metal probe and a spectrum analyzer tuned to 30 KHz. Two different types of connections were made to the analyzer. First, the signals were simply sent through a DC-block capacitor, so the input impedance at 30 KHz was $R=50 \Omega$. Second, the signals were sent into an operational amplifier with a large ($R > 100 \text{ k}\Omega$) input impedance at 30 KHz. Then the plasma density was swept out by varying the beam current in an electron beam-produced plasma.

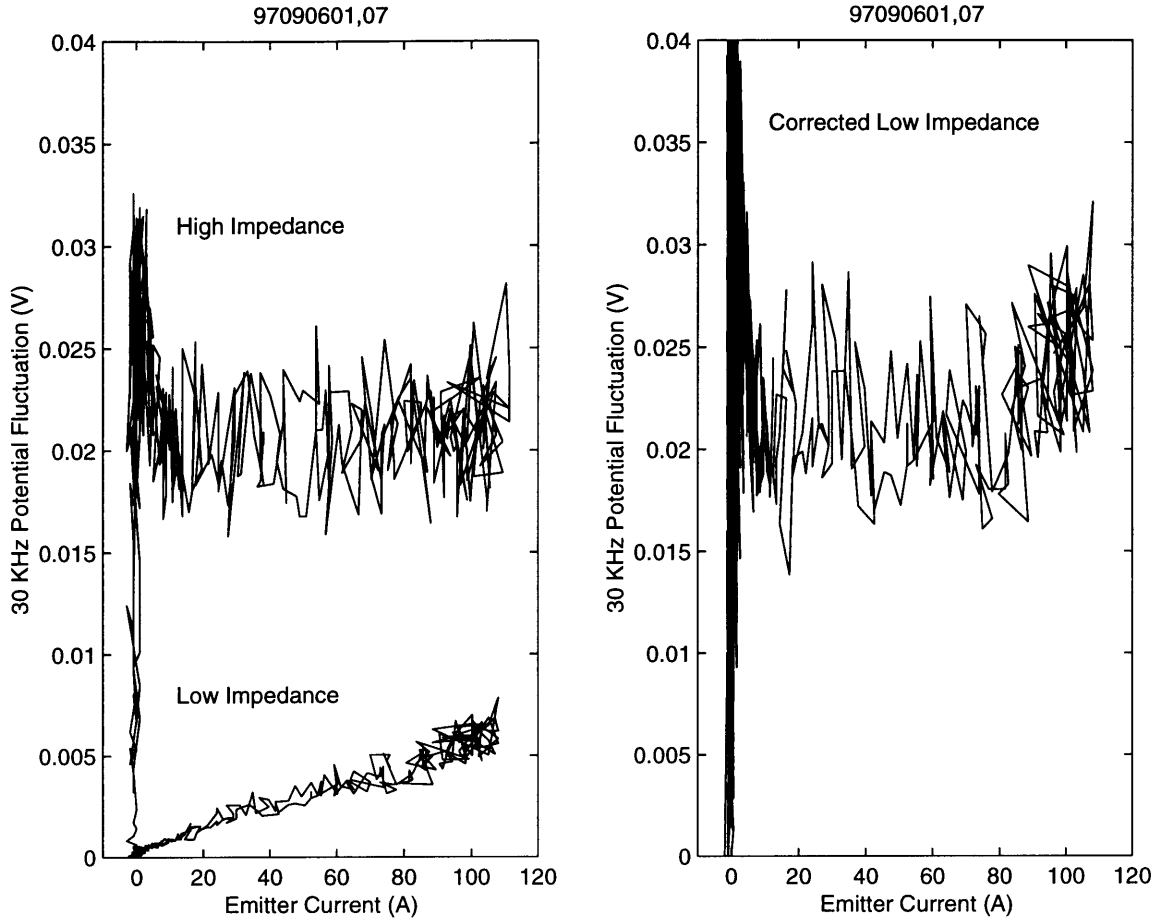


Figure 2-13: Power received at high and low input impedance. Third trace on right shows low impedance trace corrected for plasma impedance effects.

Since the signals going into the analyzer are simply a voltage division of the plasma impedance and the input impedance of the analyzer, one would expect the analyzer signal to vary in the case of the 50Ω input, where $R \sim R_p$, but to stay steady in the case of the high impedance input, where $R \gg R_p$. This is exactly the observations shown in figure 2-13. The 30 KHz power level is shown on the left for the cases of $R=50 \Omega$ and $R=100 \text{ k}\Omega$ input impedances, and on the right for the case where the 50Ω trace has been corrected according to (2.13) with measurements of the plasma density using the biased mode of the probe. Notice that the high impedance signal can be recovered from the low impedance signal using this correction, lending support to the validity of the above formulation.

2.3.2 Decisions on probe deployment

Since there is interest in both the temporal and spatial variation of the wavefields under study, it is necessary to deploy at least two probes to sample the plasma at multiple points in space. Since the spatial co-ordinates are three-dimensional, one must decide what the important directions are. In the laboratory experiment, there is a large plasma parameter variation in the radial direction. Therefore plasma waves propagating in the radial direction do not see uniform plasma parameters, and are therefore not governed by the simple homogeneous plasma dispersion relations discussed in chapter 1. However, the toroidal and the vertical directions feature fairly uniform parameters, and therefore may host wave modes which can be checked against the theoretical wave dispersion relations. Thus if one were to deploy a probe pair, it would be desirable to deploy them such that they are separated within a plane normal to the radial direction.

The next decision concerns what degrees of freedom to give the probes within this plane. The decision ultimately depends on how one wants to estimate the wavenumber-frequency power spectrum from the information available from the point samples of the plasma.

To allow arbitrary methods to be available, it was decided that the probe heads should have two degrees of freedom in the plane normal to the radial direction of the machine. In addition, it was decided that it would be good to be able to move the probe during a plasma pulse in at least one dimension, if not two. While automated movements in both degrees of freedom would be desirable, it was decided that the hardware requirements for such movement would take too long to build.

Most of the waves under investigation were assumed to propagate in the direction perpendicular to the magnetic field. Therefore, if one has to choose the single direction in which a probe can be scanned during a plasma shot, it makes sense to choose the direction across the magnetic field, so that the wavefields of the perpendicular-propagating waves can be traversed. In a toroidal device, this means scanning the probe in a vertical direction during a plasma, given that one wants to stay within

the plane normal to the radial direction. So the first component of the probe system would be a vertical scanning probe.

It was then desirable to install a second probe that could be deployed at an arbitrary position with respect to the vertical scanning probe to allow maximum flexibility in choosing the estimation scheme. It was decided that the easiest way to do this would be to construct a so-called window-wiper probe—basically a radially inserted probe, rotatable around its axis, with a 45-degree angle arm extension on the end that would allow a probe tip on the end of the arm to be moved in a circle in a plane normal to the radial direction. The vertical probe would be aligned so that it would intersect this circle at at least one point. This would allow the probes to indeed be placed at arbitrary displacement vectors (relative positions).

With the maneuverability of the probes decided upon, one could proceed with building the probes.

2.3.3 Hardware construction

The vertical automated-scanning probe was built first, because it was the more complex of the two probes.

Vertical scanning probe

The vertical scanning probe requires some sort of automatic drive mechanism to move the probe during a plasma shot. There are basically two ways to drive a probe in and out. One way is to mount a gear on a motor and thread the gear with a chain which is directly connected to the probe. Typically, one can avoid having to gear down the motor if one uses a stepper motor, which can be started and stopped very accurately. This sort of procedure is being used for the radially scannable Langmuir probe. Without gearing the motor down, one can obtain scanning speeds of around 20 cm per second. The other method is to mount a threaded rod on the axis of the motor's rotation and have this rod tug on a plate with a threaded hole.

It was decided to pursue the latter of the two approaches because it could be

built with parts that were already available around the lab, and could be controlled more accurately. A 3200 RPM induction motor was found which could drive the probe. The motor was in fact part of an earlier vertical scanning probe. The output speed was too fast to drive a screw shaft directly, so a gear box was cannibalized from a hand drill. The gear box from the hand drill was removed from the drill and was to be mounted on the front of the motor. Please refer to figure 2-14 for the following discussion. It shows a schematic of the top probe, whose construction will be described below.

An aluminum plate was machined that could be secured to the front of the motor (item 3 in figure 2-14). Holes were drilled out for the drive shaft, and two threaded studs on front of the motor. Two nuts threaded onto these nuts held the plate in place. Three round aluminum posts were then machined on a lathe and mounted on the top of this plate via recessed capscrews. Then the gear box was attached to these three aluminum posts. The drive shaft of the motor was coupled to the input shaft of the gear box via a section of G-10 tubing. The inside of the G-10 tubing was carved out so that it would sit snug on the fluted shaft of the gear box input. On the motor shaft end, a hole was cut across a diameter of the G-10 tubing through which a 2-56 bolt was inserted. This bolt was then lowered into the slot on the motor shaft. The G-10 tubing was cut to such a length that the 2-56 bolt would rest comfortably inside the shaft when the gear box was screwed down flush to the three aluminum posts on the plate covering the front of the motor.

During the above construction, the welded studs on the motor were accidentally sheared off, so it was necessary to hold the front motor plate on in some other manner. The solution was to machine two additional plates that would fit over the plate on the front of the motor and the over the back of the motor (items 22 and 28 in figure 2-14). These two plates could be squeezed together by tightening down on two threaded rods connecting the plates, effectively holding the gearbox steady with respect to the motor. Care had to be taken to not tighten these plates too much as it would prevent the motor from turning properly.

This motor/gearbox assembly was then mounted on two upside-down U-shaped

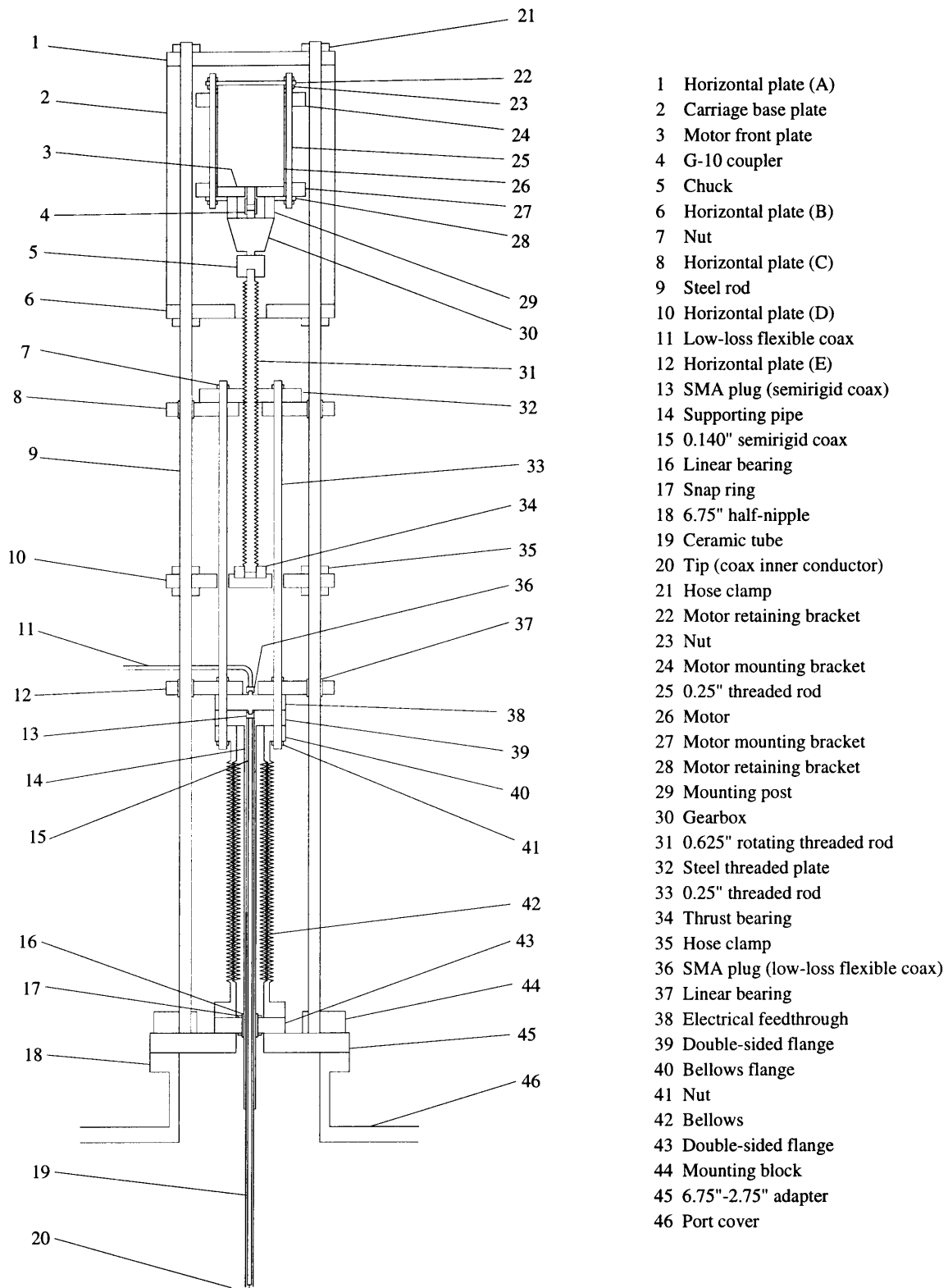


Figure 2-14: Schematic of top probe.

brackets (items 24 and 27). The legs of these brackets were then screwed into a large aluminum plate, which would form the bottom of the motor carriage. One of the two brackets was located underneath the plate on the front of the motor. It was intended to support the front of the motor, and the gear box assembly. This bracket was screwed into the aluminum plate on the front of the motor via a couple cap screws. Another bracket was located at the rear of the motor, to support the weight of the armature and windings. It was not possible to attach this bracket to the motor in any way, so it was decided to thread a large hose clamp (not shown) around the motor and carriage base plate, effectively sandwiching the bracket in between the motor and the plate. Front and rear vertical aluminum plates were then screwed on to the horizontal plate to form the front and rear of the motor carriage. A hole was cut in the front plate in order to allow the motor shaft to extend out the front of the carriage.

With the carriage complete, it was necessary to devise a track on which one could mount the motor carriage, and ultimately, the sliding probe parts. The track would be attached on one end to the port cover and have the motor carriage sitting on its other end. The sliding probe components would sit in the space in between these two.

It was decided that the track should consist of three 4' steel rods arranged in a triangular pattern. To place the carriage on this track, all one had to do is drill three holes in the front and back plates of the carriage and slide on the carriage. However, it was a little trickier to attach three rods to the port cover. The solution was to use an existing port cover with a 6.75" half-nipple mounted on it. On the half-nipple, a 6.75" flange to 2.75" flange adapter was mounted. The 2.75" bolt circle provided a platform onto which to mount the probe bellows and the annular region between the 6.75" bolt circle and the 2.75" bolt circle served as a platform on which to mount the triangle pattern of steel rods. Mounting blocks were machined so that the steel rods in this annulus could be secured by the 6.75" bolt circle.

With the track in place, and the carriage able to slide onto the end of the track, it was now necessary to design the other components of probe—the sliding plates onto which the probe would be mounted, and the probe itself. In figure 2-14 are shown a

total of 5 horizontal plates that were built: items 1, 6, 8, 10 and 12, which will be referred to as plates (A) through (E), respectively.

(A) and (B) hold the motor carriage. (C) has been tapped so it can slide on a 1' long, 0.625" diameter threaded rod which is held in the chuck of the gear box output shaft. This threaded rod extends through the middle of (C) and down to plate (D), where it rests on a thrust bearing. The bearing serves to keep the threaded rod secure on both ends. Plate (E) secures the rear of the probe proper. It contains a bolt circle matched to the bolt circle of the 2.75" flange, so that the flange can be held centered on the track. This plate is pushed and pulled using two 0.25" threaded rods (item 33) which extend up to the plate (C) via 2 holes cut in the plate (D) containing the thrust bearing.

It should be noted that with this arrangement plate (C) can slide all the way from the inner side of the carriage, plate (B), to the plate containing the thrust bearing, plate (D). This arrangement allows for about 25 cm of travel, depending on the location of stop switches for the motor. To assure smooth movement, plates (C) and (E) were outfitted with holes through which were mounted linear bearings for the three steel rods. The linear bearings feature ball bearings that run on a circular track that lies in a plane parallel to the axis of the rods. Another detail to note is that plate (C) had to be outfitted with a small attachment of stainless steel (item 32) which was tapped for the rotating 0.625" threaded rod. The aluminum plate itself could not be used because it would degrade under repeated use.

Now we turn our attention to the in-vacuum components of the probe. First, we start with an electrical feedthrough, which was mounted flush with plate (E). Modifications were made to plate (E) to allow connections of external cables to this feedthrough. Inside the vacuum, a long section of stainless steel 0.140" semirigid coax was connected to the inside of the electrical feedthrough, using standard SMA solder-on connectors. The connectors proved difficult to solder on to the stainless steel, so they were spotwelded.

Placed over the semirigid coax was a double-sided flange welded to a 0.5" support pipe, which would serve as the backbone for the in-vacuum parts. Over the pipe

was placed a long section of bellows, so that the bellows, double-sided flange, and electrical feedthrough could be held as one sandwich attached to plate (E).

The metal bellows were then attached to the half nipple on the port cover and the motor was tried out. It was discovered that the supporting pipe would oscillate laterally within the inner diameter of the 6.75" to 2.75" adapter. To remedy this problem it was decided to stick a linear bearing in a double-sided flange and place the flange between the machine end of the bellows and the 6.75" to 2.75" adapter. A 0.875" hole was bored out of the flange and a bearing was held in the hole via two snap rings. The bearing was vacuum tested and was deemed acceptable.

Approximately 1' of the 0.5" pipe extended out the end of the bellows. A small 4-40 hole was drilled and tapped in this part of the pipe, about 8" from the end, in order to allow a set screw to be placed to hold a ceramic tube in place, as described in the next paragraph.

A long 4' section of 0.375" ceramic tube (item 19 in figure 2-14) was inserted inside the pipe, over the coax, so that about 2' of ceramic remained sticking out of the 0.5" metal supporting pipe, and a few inches of coax were left hanging out of the end of the ceramic tube. The required length of ceramic was measured precisely, and a position was marked where the ceramic was to be notched. It was then notched so that a set screw in the metal supporting pipe could be screwed in to hold the ceramic tube in place.

Attention was then turned to the tip of the probe. The outer conductor of the coax was trimmed back until it was about 2 mm inside the end of the ceramic tube. The inner conductor was left about 1" longer than the outer conductor, so that it stuck out of the end of ceramic. This inner conductor would serve as the sensor for the plasma parameter fluctuations.

The motor carriage plates (A) and (B) and plate containing the thrust bearing, plate (D), were then fixed in the appropriate locations along the steel rod track using hose clamps, completing the construction of the probe.

For the purposes of controlling the motor motion, it was necessary to mount stop switches on plates (B) and (D). The switches were mounted in such a way that they

could be depressed by two metal tabs bolted on to plate (C). In addition, potentiometers were mounted on plates (B) and (D). These potentiometers were outfitted with gears which allowed a loop of timing cable to be run around the gears. This loop was gripped at one point by a metal tab mounted on the plate (C). Note that to sense the position, only one potentiometer is needed. However, the second potentiometer served as a good platform onto which to mount a gear.

Wires for the motor 120 VAC, the switches and the potentiometer were run from the probe (mounted on top of the VTF machine) down to a cabinet beside the machine. Inside the cabinet was placed a controller for the motor. The controller consisted of a metal panel with toggle switches to control the motion of the probe either manually or automatically during an experiment.

The drive signal for the probe consisted of a 24 V voltage which is either sent by the PLC in automatic mode or from a power supply switched on and off by a front panel switch in manual control mode. This 24 V signal throws a relay which switches 120 V on and off to the motor. The forwards and/or reverse leads for the motor can be selected using another switch, allowing one to specify the direction of the motor drive. The forward (in) limit switch is in series with the 120 V motor forward power lead and the reverse (out) limit switch is in series with the reverse power lead. The switches therefore cut power to the motor when they are depressed, but allow the motor to still be energized in the opposite direction.

The PLC signal is generated by a digital output module that is also used to provide control signals for the electron beam supplies. The digital output modules are controlled by a terminal in the control room. A field has been made in the GUI that allows the operator to set the on-off timing for the probe.

A photograph of the completed probe mounted on the machine is shown in figure 2-15.

Horizontal rotating probe

The horizontal probe was very different from the vertical probe in design because the primary motion was to be rotational, rather than linear. Since linear motion was

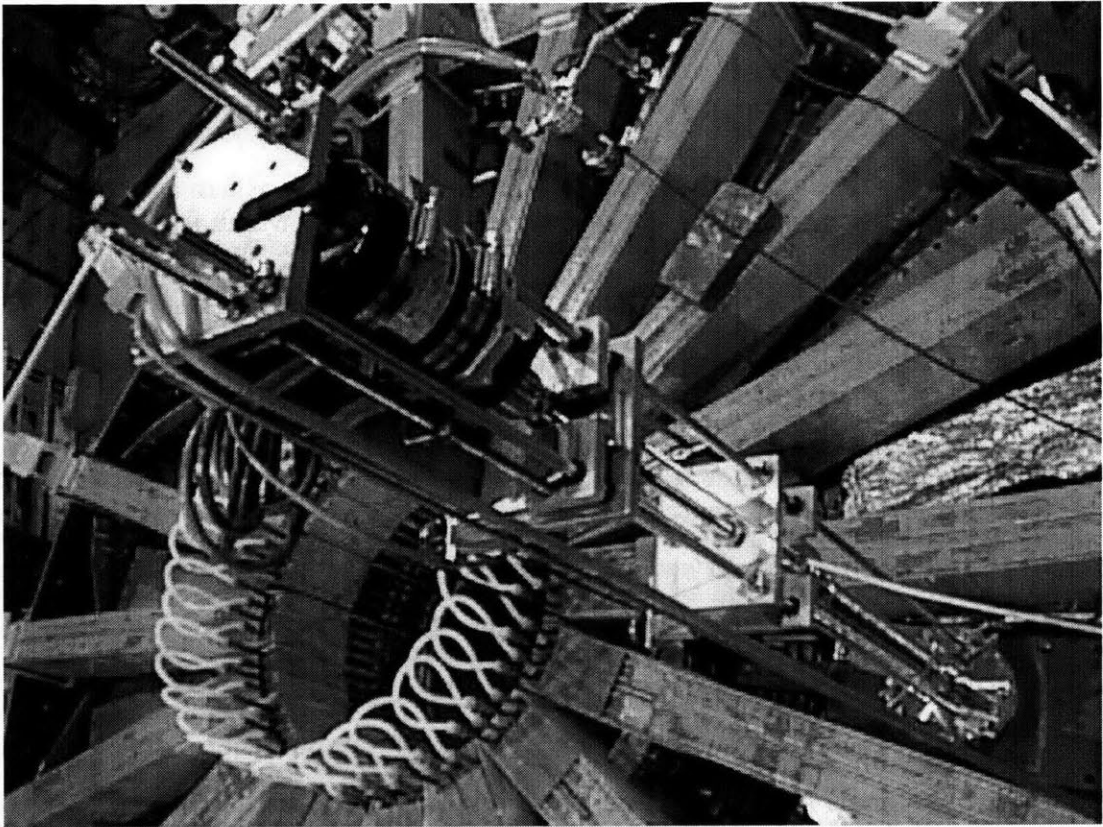
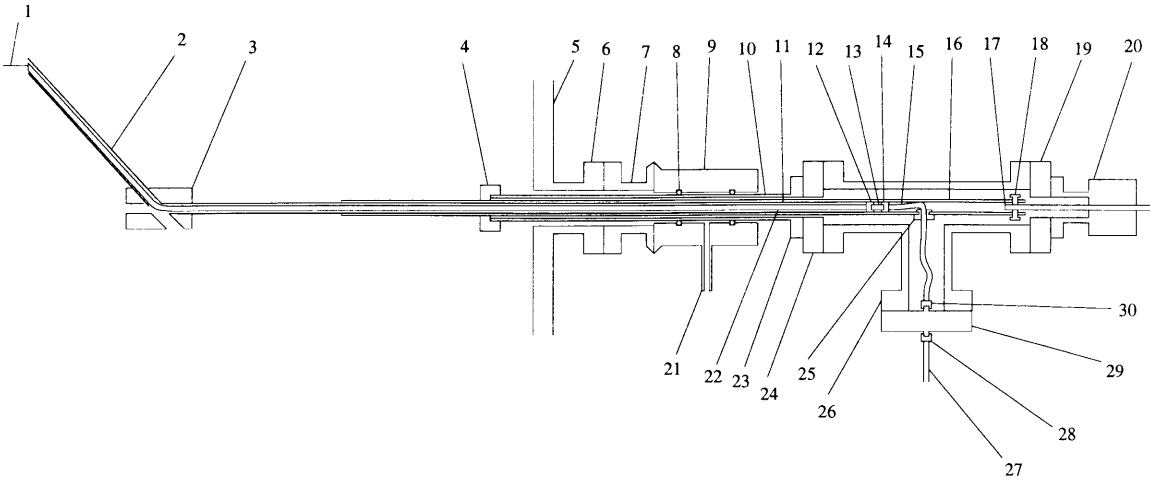


Figure 2-15: Top probe mounted on the machine.



- | | |
|---------------------------------|--------------------------------------|
| 1 Tip (inner coax conductor) | 16 0.5" supporting pipe |
| 2 Ceramic arm | 17 0.25" shaft |
| 3 Coupler box | 18 Capscrew |
| 4 Aluminum bearing | 19 2.75"-1.333" flange adapter |
| 5 Port cover | 20 Rotary feedthrough (simplified) |
| 6 Half-nipple | 21 Wilson seal pump port |
| 7 ConFlat to KwikFlange adapter | 22 0.140" semirigid coax |
| 8 O-ring | 23 1.333" flange |
| 9 Wilson seal | 24 2.75"-1.333" flange adapter |
| 10 0.75" supporting pipe | 25 Nylon button |
| 11 Ceramic tube | 26 "T"-section |
| 12 SMA plug (semirigid coax) | 27 Low-loss flexible coax |
| 13 Female-female SMA adapter | 28 SMA plug (low-loss flexible coax) |
| 14 SMA plug (flexible coax) | 29 SMA electrical feedthrough |
| 15 RG-174 flexible coax | 30 SMA plug (flexible coax) |

Figure 2-16: Schematic of side probe.

not important, it was possible to use a rigid Wilson seal device for the probe body as opposed to a flexible bellows mounted on a track. A VTF side port was selected which featured an array of half-nipples. A ConFlat to KwikFlange adapter was placed onto one of these half-nipples, allowing for the attachment of the Wilson seal.

A 2' long 0.75" pipe was located with a 1.333" flange welded on one end. This pipe was inserted into the Wilson seal. Then a 0.5" pipe was located and cut to a 4' length. This pipe was inserted into the 0.75" pipe so that it stuck out at either end. This pipe would serve as the rotating mechanical support for the in-vacuum parts of the probe. Please refer to the schematic in figure 2-16 for this discussion.

On the rear end of the 0.5" pipe, where it emerged from the 1.333" flange, a U-shaped slot was cut out of the inner 0.5" pipe along the length of the pipe, through which one could pass flexible coax from the inside of the pipe. The idea was that semirigid coax would run from the probe tip back to just inside the U-shaped slot.

Then the semirigid coax would be converted to flexible coax and the flexible coax would run out of the U-shaped slot in the pipe and to an electrical feedthrough away from the axis of the main probe. If one leaves a little bit of slack between where the flexible coax exits the supporting pipe and where it hooks on to the electrical feedthrough, then one should be able to rotate the pipe one revolution or so in each direction with the electrical feedthrough fixed in position. Unfortunately, there are two problems with this approach. First, there is nothing to prevent the semirigid coax from sliding back and forth inside the 0.5" metal pipe. Second, the braided outer conductor of the RG-174 tends to fray on the edges of the U-shaped slot, degrading the cable after repeated rotation cycles. To fix these problems, a nylon button-like device (item 25 in figure 2-16) was machined out of a nylon bolt and nut.

The nylon button consisted of a bolt of nylon drilled out on its central axis. The nut was screwed onto this bolt so as to leave about 1.5 mm between the head of the bolt and the nut. The two edges of the U-shaped slot then slid into this 1.5 mm gap. Small adjustments were made to the position of the nut until this nylon button was held quite firmly in place while inserted in the slot. The small flexible coax was threaded through this button, and then the button was pushed all the way to the base of the slot. With this button in place, flexible coax was forced to make a rather abrupt 90 degree turn before exiting the pipe. This turn prevented casual movement of the semirigid coax up and down the 0.5" supporting pipe. The nylon was also soft enough to prevent the coax from being damaged as the pipe rotated.

With about 1' of flexible coax protruding through the nylon button hole, the enclosure for the flexible coax section could be installed. A 1.333" to 2.75" adapter was attached to the end of the 0.75" outer pipe. Then a 2.75" "T"-section was attached to this adapter, enclosing the nylon button and U-shaped slot in the pipe. The coax was threaded out through the perpendicular port on the "T"-section. A rotary vacuum feedthrough was located. The feedthrough was mounted on the rear of the "T" flange so that the 0.25" shaft of the feedthrough protruded about one inch into the interior of the "T"-section. The plan was to mount the 0.5" supporting pipe directly onto the 0.25" rotary feedthrough shaft. This was accomplished by pulling

the 0.5" pipe a few cm out of the "T"-section and drilling and tapping the pipe with three holes about 1 cm from the end of the pipe, at approximately 120 degrees to each other. Small 4-40 cap screws were placed in these holes. These screws pointed inwards and were tightened down to grip the 0.25" rotary feedthrough shaft (see item 18 in figure 2-16).

The rotary feedthrough and 1.333" to 2.75" adapters were tightened down to the "T" vacuum section and the 0.75" pipe was tightened down to the 1.333" to 2.75" adapter. With the rotary feedthrough in place, the 0.5" supporting pipe was supported at its rear end, on-axis with the rest of the probe. However, this pipe was not supported at its other end, especially where it exited from the 0.75" pipe inserted into the Wilson seal. The solution was to machine a bearing device (see item 4) shaped like a lid for a glass jar. On the side wall of this device, three holes were drilled and tapped so that the device could be clamped (centered) onto the end of the 0.75" pipe. Then a centered 0.5" hole was drilled through the top of this device through which the 0.5" pipe could be inserted. The bearing provided a support for the 0.5" pipe, keeping it centered and steady within the 0.75" pipe.

An SMA electrical vacuum feedthrough flange was located. The fully flexible coax was screwed onto the inside of the feedthrough and the feedthrough was bolted on to the perpendicular arm of the "T"-section.

Returning to the front of the probe, a small hole was drilled and tapped in the 0.5" metal pipe a couple inches from the forward end. Then a long tube of ceramic was inserted inside the 0.5" supporting pipe, and around the semirigid coax. The ceramic tube was inserted to a depth of about 2' so that it would not interfere with the SMA semirigid to flexible coax connection. With the ceramic inserted, a pencil marked the position for a notch, which was then cut using a diamond saw. The ceramic was reinserted and fastened in place with a small 4-40 set screw. At this point, the ceramic stuck about 2' out of the metal pipe. This is the section of ceramic that would stick into the plasma, and on which the 45-degree arm (item 2) would be mounted. Approximately 18 inches of semirigid coax stuck out from the ceramic—enough to run the length of the 45-degree arm and form a probe tip.

The next step was to machine a small block which would serve as the coupler between the horizontal ceramic and the 45 degree arm. A small aluminum piece about 2" long, 1" high, and 0.75" high was cut out. A 0.375" hole was drilled lengthwise through the center axis. Then a second hole was drilled from top to bottom through the block, such that the axis of the second hole formed a 45-degree angle with the axis of the first hole. The idea was that the horizontal ceramic would slide half way into one end the first hole. A small slit was cut between the other end of the first hole and the top end of the hole cut from top to bottom. This slit was just wide enough to allow the semirigid coax to be bent from a horizontal angle to a 45 degree angle with the horizontal ceramic in place inside the block. Holes were tapped on one end of the horizontal hole, and the horizontal ceramic was notched with the diamond saw such that 6-32 set screws could be inserted into the block and hold it fixed with respect to the horizontal ceramic. A small 9" length of ceramic was cut, which would serve as the 45-degree angle extension for the probe. Note that the end of the ceramic was cut of at a 45-degree angle so that once the arm was in place, the end of the ceramic tubing would form a smooth plane normal to the radial direction (the direction of the rotation axis of the probe). In other words, it was cut such that the ceramic shield would not block the probe tip from a line of sight in the direction of \hat{z} as the probe was rotated. Next, holes were tapped on the top end of the top-bottom hole on the block, and the 9" section of ceramic was notched, such that 6-32 set screws could be inserted into the block to hold the 45-degree arm in place. With the horizontal ceramic in place, the semirigid coax was bent to a 45 degree angle, passing it through the slit that had been cut for this purpose. Then the 9" ceramic arm was fastened in place. The outer conductor of the coax was trimmed back until it was about 2 mm inside the end of the ceramic, as in the case of the vertical probe. Then the inner conductor was left trimmed about 1 inch longer than the outer conductor.

At this point, it was decided that the aluminum coupler box would stand a better chance of survival in the plasma if it was wrapped in a cover of steel sheet metal. A piece of 0.0625" sheet metal was cut and bent so that it could slide onto the coupler block lengthwise and cover the holes containing the 6-32 set screws. In order to fasten

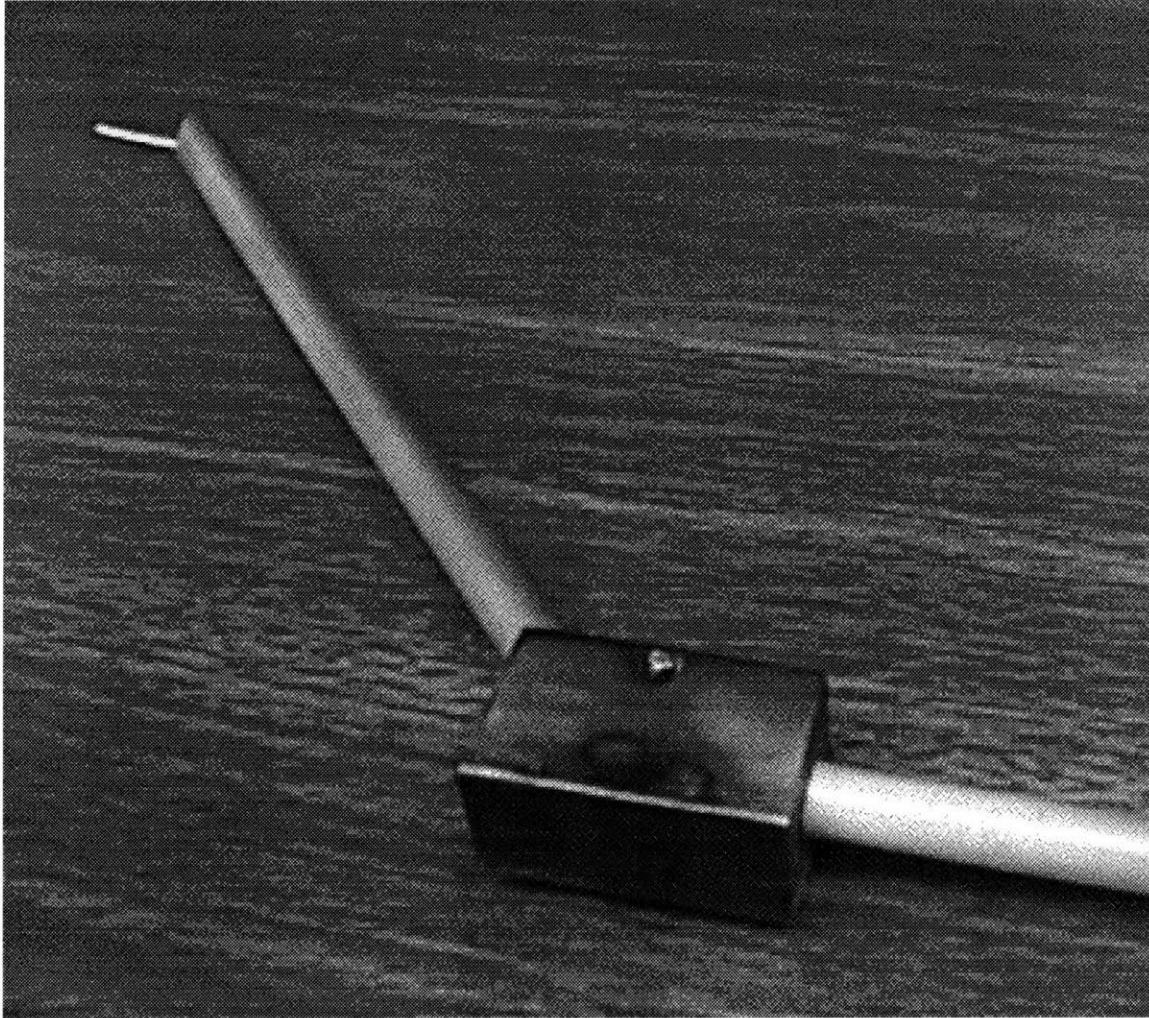


Figure 2-17: The rotating arm.

this shield in place, a small 2-56 hole was drilled straight through the width of the block and the sheet metal cover. A long 2-56 bolt and nut was inserted through these holes to hold the cover in place on the block. A photograph of the completed probe arm is shown in figure 2-17.

With the probe essentially complete, it was necessary to add a potentiometer to the rotary feedthrough in order to keep track of the position of the probe. A large gear was mounted on the outside of the vacuum-rotary feedthrough. Then a bracket was machined on which a potentiometer outfitted with a smaller gear was mounted, such that the gears would mesh. Three wires were run from this potentiometer out to the control cabinet.

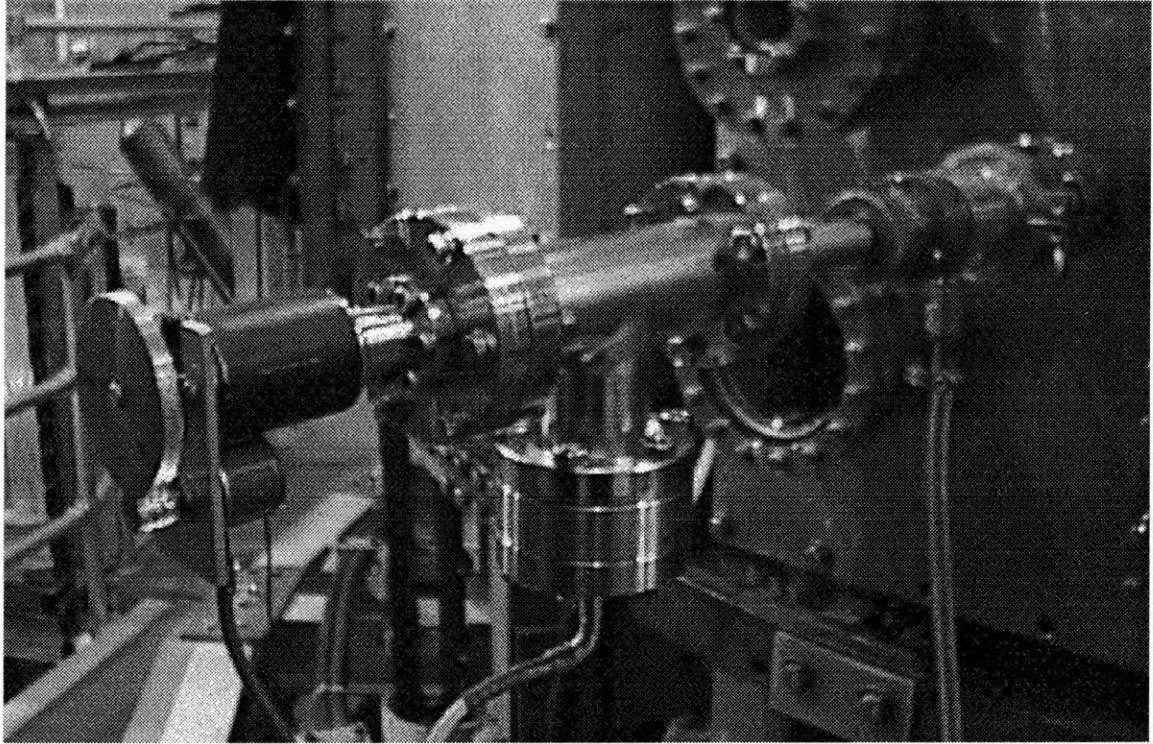


Figure 2-18: The side probe.

The side probe was mounted on the machine almost directly underneath the top probe, at 300 degrees. This meant that the probes were 80 degrees (about 1 m) away from the transmitting antenna. The reason for putting them at such a distance was to ensure that they were in the farfield zone around the antenna.

Finally, a hose was connected to the differential pump port of the Wilson seal and the hose was run to Swagelock hose barb "T"-connections so that the pumping duties could be shared with the antenna feedthroughs on the transmitter.

A photo of the side probe mounted on the machine is shown in figure 2-18. A family portrait of the two probes inside the machine is shown in figure 2-19.

This concludes discussion of the construction of the receiving apparatus. The external electrical connections to the probes are a function of the experiment, and will be described in chapter 3.

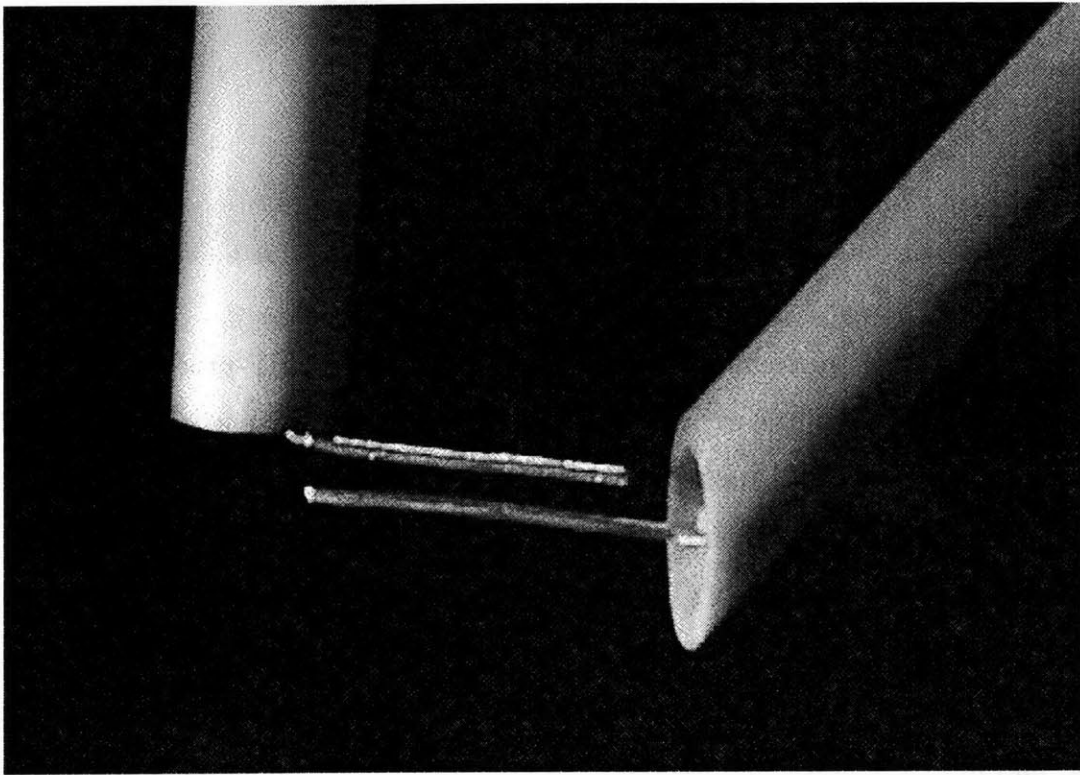


Figure 2-19: Deployment of the two probe tips.

Chapter 3

Diagnostic Measurements

This chapter discusses measurements of the plasma using the top and side probes described in the previous chapter. Methods of spectral estimation are described and implemented.

All measurements presented in this chapter were made on RF-produced plasmas. It was discovered during the experimental runs that the probes, particularly the side probe, were not able to withstand the electron beam plasma. This lack of survivability was especially pronounced when the emitters were biased at -720 volts, a modification that was described in chapter 2.

The problem was that the side probe would break off between the metal coupler box and supporting pipe. What appeared to happen is that the ceramic would first crack, and after the crack had exposed the grounded outer conductor of the coaxial transmission line, the beam would then have a tendency to arc to the line and melt it. A picture of the probe ceramic after an arc event is shown in a photograph in figure 3-1.

The author's response to the first instance of the probe breaking was to simply rebuild the probe and try again. No modifications were made because it was suspected that the cracks existed in the ceramic prior to installation. When the probe was immersed in plasma, it was assumed that the cracks worsened, and the ceramic snapped, allowing the beam to merrily arc to the outer conductor of the coax.

However, after being rebuilt, the probe then broke a second time in almost exactly

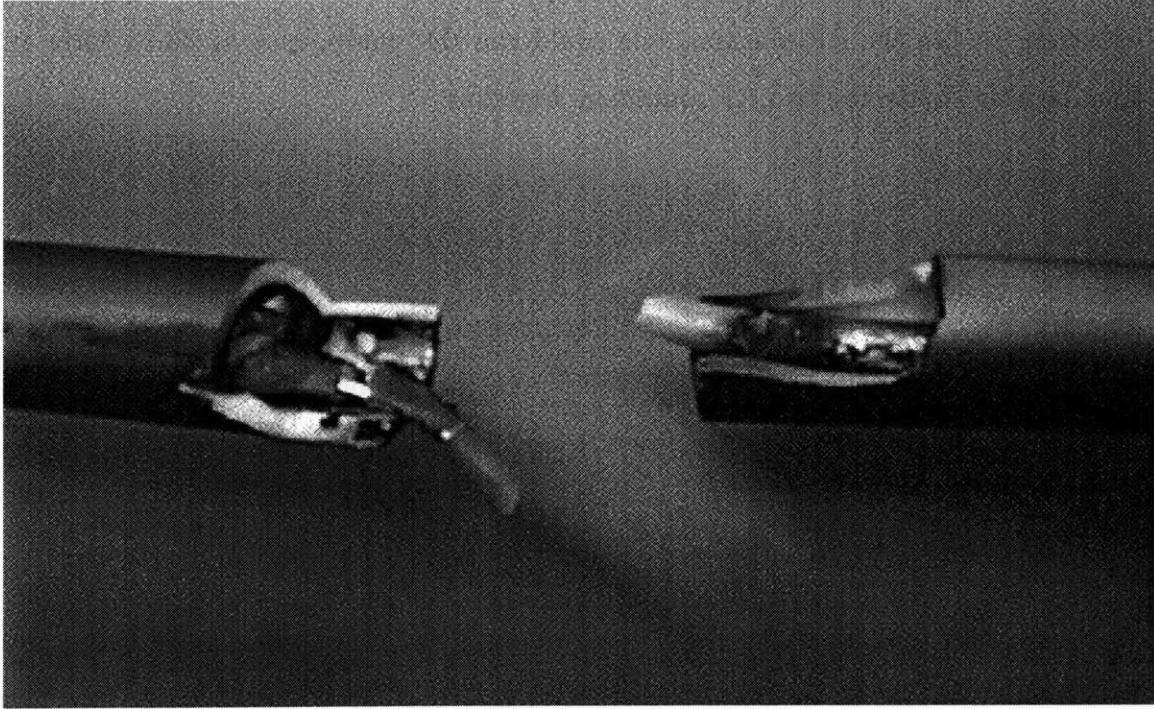


Figure 3-1: Damage to side probe ceramic after arc.

the same spot. Fortunately, the break was noticed almost immediately, and the experiments were stopped before an arc occurred to the coax. Inspection revealed that the ceramic had broken, but without any apparent heating of the break area. Normally, ceramic becomes blackened as it is repeatedly heated, but the location of the break showed no evidence of discoloration. Cracks already in the ceramic were ruled out as a possibility, because the problem had occurred twice in exactly the same spot. Furthermore, damage due to torques and vibration were also ruled out, because despite the axial rotational asymmetry of the arm and the fact that the probe can rotate quite easily, the probe was never pushed out of position during a shot. The cause of the problem remains unknown. However, whatever the nature of the destructive mechanism, it was clear that it was only present near the emitters in the lower half of the chamber, as the crossed-dipole antenna in the upper half of the chamber suffered no ill effects at any time.

For the third attempt, it was decided there was not enough time to redesign the probe in order to improve survivability. Thus it was decided to run the probes in the benign ECRH plasmas for the purpose of recording data for this thesis. As a result

of having to use the RF plasmas, one could run the pump wave at 36.14 MHz and thus be able to use the two RF amplifiers together.

3.1 Single-probe measurements

The first probe measurements that will be presented involve measurements made by a single probe. The single probe provides a point sample of the variations in a plasma parameter, such as the RF density or voltage fields.

3.1.1 Excitation of modes at the pump wave frequency

At the frequency of the pump wave, the best way to examine the frequency spectrum of the point-source is to use a spectrum analyzer. The dynamic range and large bandwidth of the analyzer make it the favorable choice over digital sampling when all that is required is a frequency spectrum. When more information is necessary (as in the case of the two-probe measurements), digital sampling methods will be used in combination with mixers which allow the frequency bands to be translated down in frequency.

For the single probe measurements of the pump wave spectrum, two analyzer traces will be presented here. First, the spectrum of plasma in the presence of a 36.14 MHz pump wave is shown in figure 3-2. Second, the spectrum of the plasma without the pump field is shown in figure 3-3. Clearly the central peak and the associated sidebands are due to influence of the pump wave, because there are no discernable modes in the background due to the ECRH heating. We see right away that the pump wave, which is less than 300 Hz wide at the noise floor of the spectrum analyzer, has been bandwidth-expanded into a structure that is more than 5 MHz wide. This is immediately a sign that the pump is interacting nonlinearly with the surrounding plasma to produce off-pumpwave frequency modes.

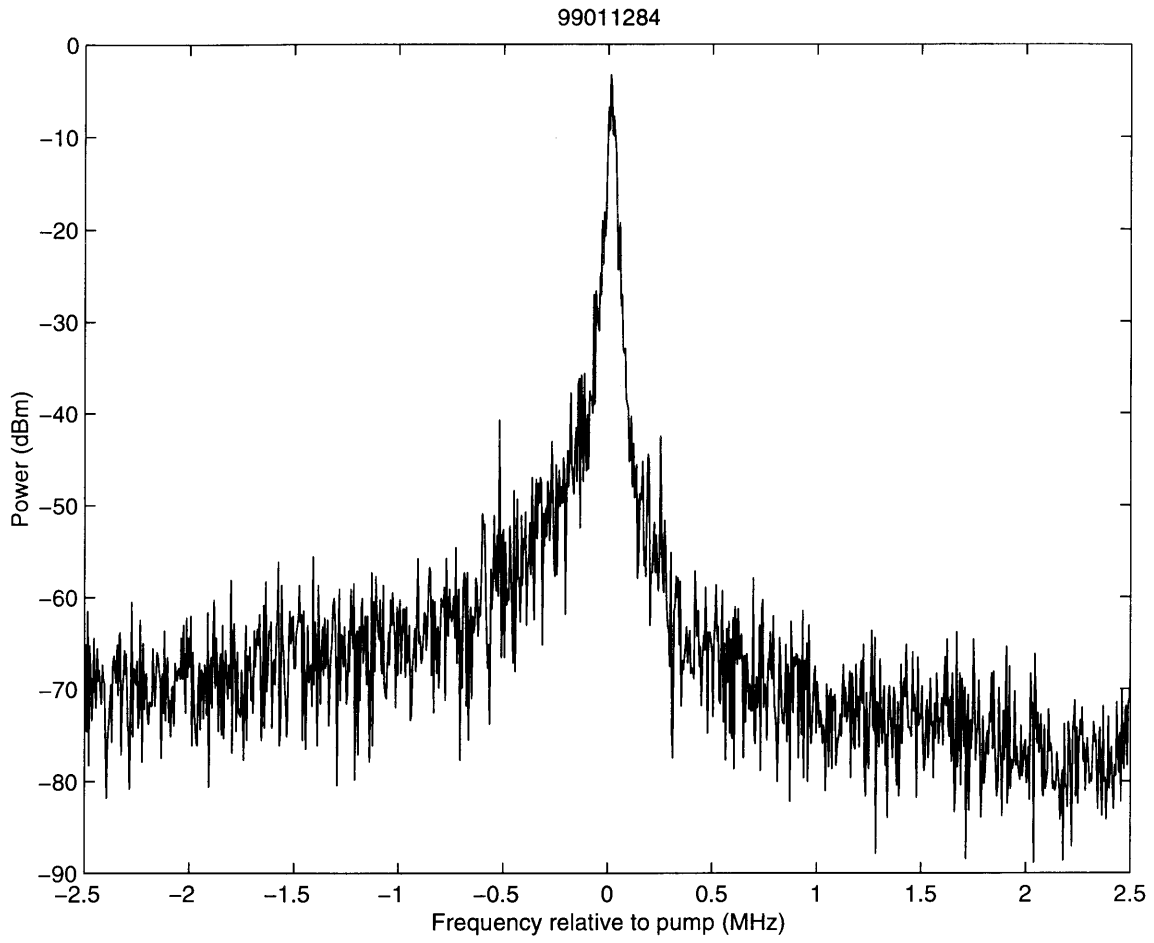


Figure 3-2: Spectrum of plasma voltage fluctuations around the pump wave frequency.

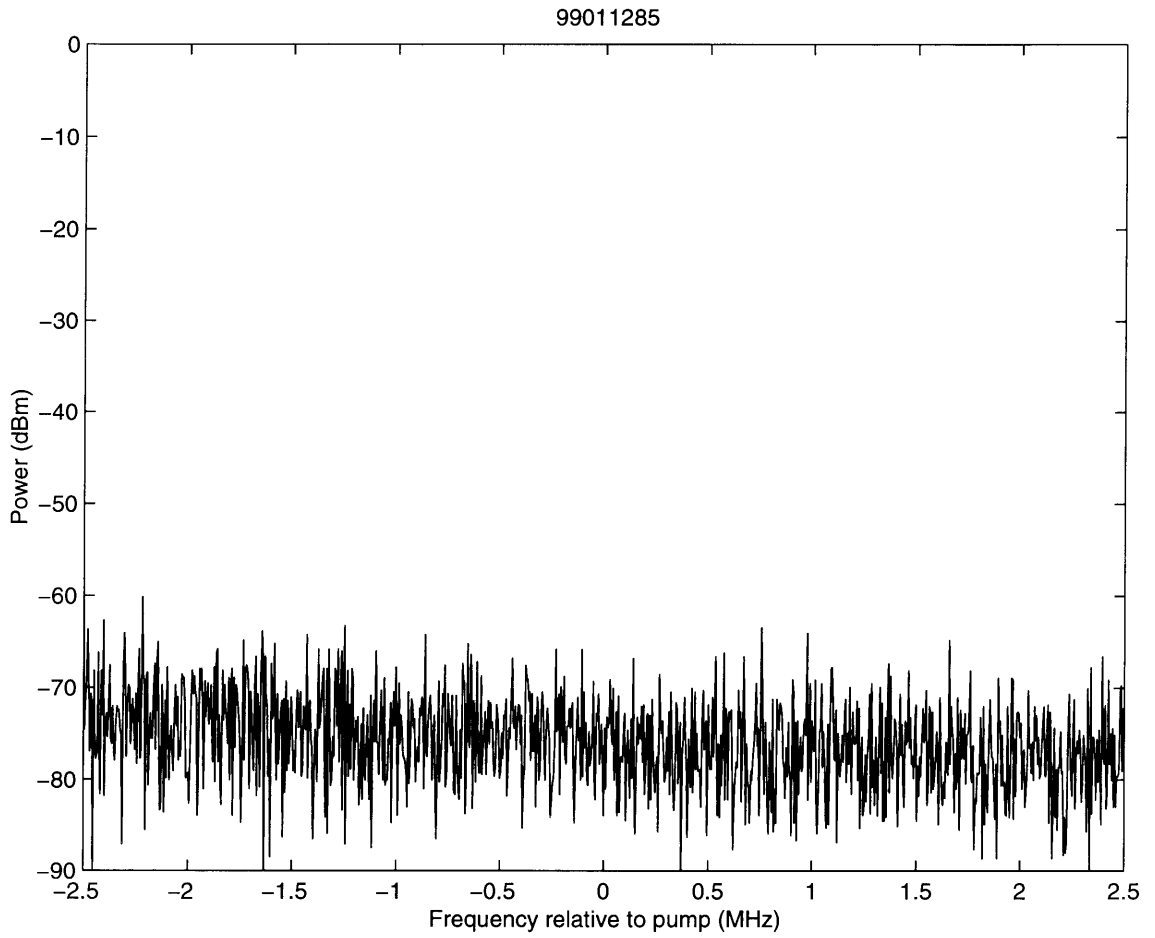


Figure 3-3: Spectrum of plasma voltage fluctuations around the pump wave frequency in the absence of the pump.

3.1.2 Excitation of modes at zero-frequency

There is also interest in the spectrum in the zero-frequency range. Realistically, if there are zero-frequency modes being generated by the pump wave, they would suffer doppler shifts due to crossfield drifts in the plasma, such as the diamagnetic drift, the curved B field drift and the gradient B drift. The sum of the effects of these drifts are on the order of between 100 and 1000 m/s, which can explain the doppler shifting of waves into the frequencies of tens of kHz. However, the drifts involve ions and electrons flowing opposite directions, which may have an effect on the nature of the purely growing mode.

Nevertheless, the spectrum in the kHz range is significantly affected by the presence of the pump wave. Two spectra are presented. They are both shown in figure 3-4 so that comparison of the two may be made. The top trace is the spectrum of the plasma in the presence of the RF pump field. The bottom trace shows the spectrum in the absence of the pump field. Filtering has been applied with a first order roll-off at 5 kHz (to block DC plasma floating potential) and a fifth order roll-off at 500 kHz (anti-aliasing). The spectrum in the presence of the pump is certainly far more excited than in its absence. This excitation can be verified by examining a time-series of data. Shown in figure 3-5 is a comparison of the raw voltage fluctuations as sensed by the probe alongside the pattern of 100 W of RF that was being pulsed on and off while the fluctuations were being recorded. Clearly the trace shows enhancements during the pulse. The enhancements in the voltage signals during the RF pulsing cannot be explained by change in the probe response, as put forth in the discussion surrounding figure 2-13. Neither a temperature effect nor a density effect on the plasma impedance due to the presence of the injected 100 W of RF would be sufficient to explain the change in the signal level.

3.2 Double-probe measurements

The purpose of the double-probe measurements is to recover information about the temporal *and* spatial variation of the plasma from two point sources of information.

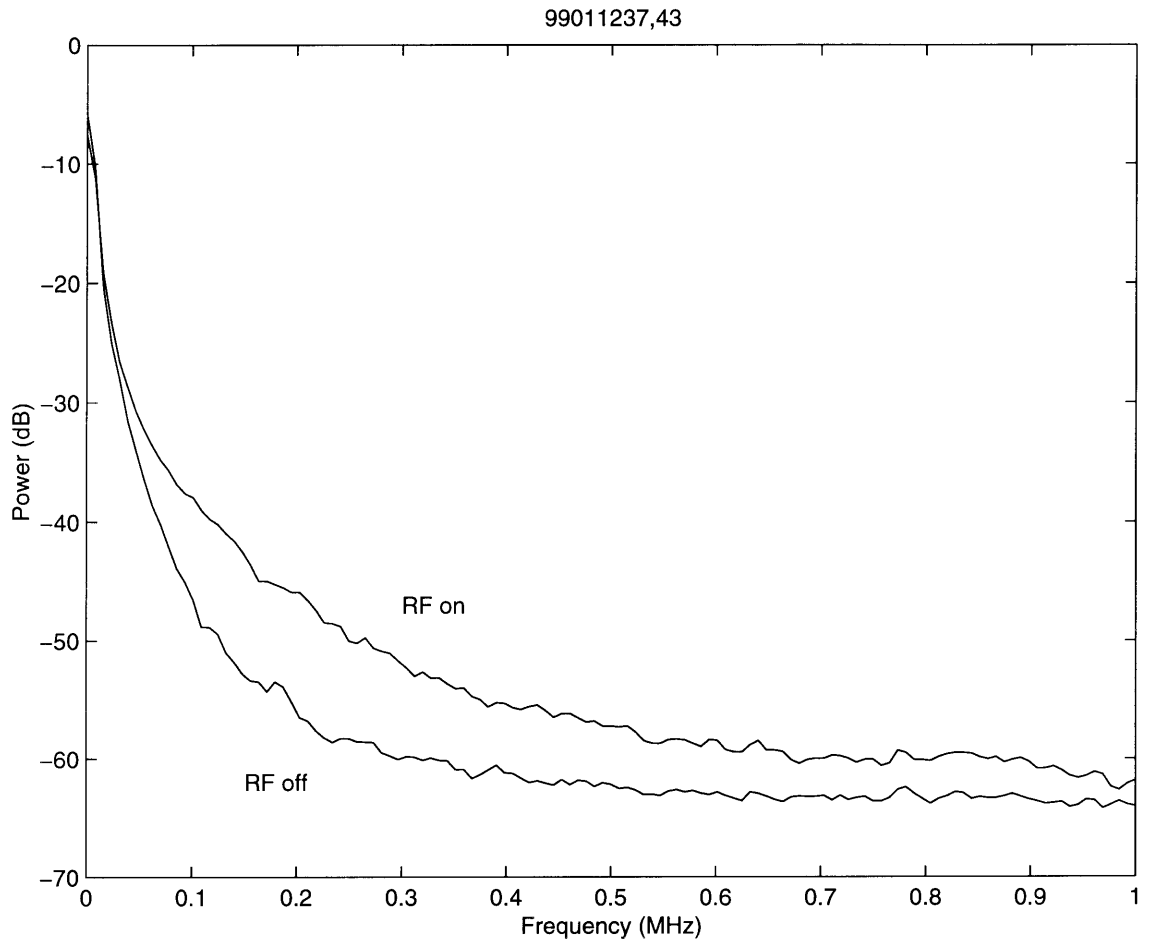


Figure 3-4: Spectrum of low frequency plasma voltage fluctuations with and without the presence of the pump wave.

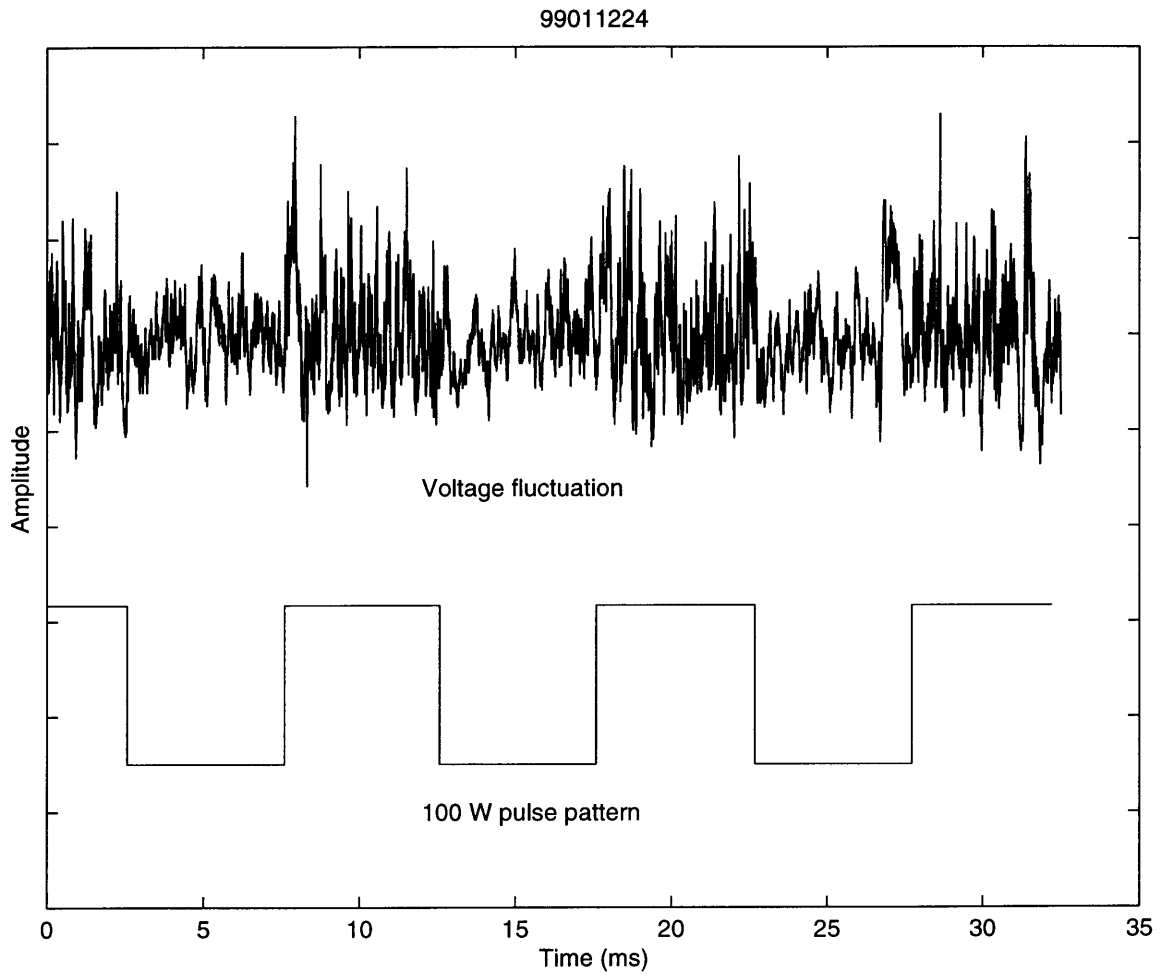


Figure 3-5: Time series of voltage fluctuations during RF pulsing.

In the absence of assumptions about the space-time coupling of the processes under observation (such as the presence of dispersion relations, plane waves, or dominant modes), the process unfolds as follows.

The point data series are best thought of as random processes. The random process is a basically a continuous interval of random variables, each of which has an associated probability density function, and a degree of correlation with its neighbors. The probability distributions at each point in time can be characterized, for example, by their moments, such as mean and variance. The correlation between pairs of random variables, say $x_1 = x(t_1)$ and $x_2 = x(t_2)$ can be described by the correlation function

$$R_x(t_1, t_2) = \int \int X_1 X_2 f_{x_1, x_2}(X_1, X_2) dX_1 dX_2 \quad (3.1)$$

where f_{x_1, x_2} is the joint probability distribution function of x_1 and x_2 . It is often the case that x forms a *wide sense stationary* process. This means that $R_x(t_1, t_2) = R_x(t_1 - t_2)$, or in other words, R_x only depends on how far apart in time the two random variables are. In the case of wide sense stationarity, we can set $\tau = t_1 - t_2$ and call the transform

$$S_x(f) = \int R_x(\tau) e^{-j2\pi f\tau} d\tau \quad (3.2)$$

the power spectral density (PSD). The PSD is a popular way to characterize a random time series, because it is a function which is uncorrelated across frequency, and has strong intuitive appeal.

The lack of correlation across frequency means that the magnitude of the PSD at one value of f does not determine in any way the values at neighbouring points. In other words, it forms a way to analyze a process into its components, hence the term spectral *analysis*. The strong intuitive appeal stems from the fact that the value of the PSD at any point gives one the flavor of “how much” of a certain frequency component exists in the random process $x(t)$.

The danger of this intuitive notion is that one tends to get carried away with the concept of frequency content and start equating the PSD with the Fourier transform of a time series. The two are not the same. The PSD is deterministic quantity that

is simply the transform of a two-dimensional moment. The transformed time series is an experimental outcome of the random process $x(t)$.

The experimentalist appeals to the intuitive notions of frequency content in the PSD to help analyze what frequencies (or modes) have been excited in a system. Unfortunately, the experimentalist does not have access to the probability density function f_{x_1, x_2} , but rather only has one (or more) experimental outcomes of the process. However, certain statistics of these experimental outcomes can be shown, under the assumption of stationarity and *ergodicity*, to asymptotically approach the true values of the PSD or autocorrelation functions. The frequency averaged periodogram and the correlogram are examples of PSD and autocorrelation estimators, respectively.

The idea of the autocorrelation function can be extended to represent a random process that proceeds in two dimensions, denoted by $x(t, r)$. Then we have that the autocorrelation of two random variables in that two-dimensional space is given by

$$R_x(t_1, t_2, r_1, r_2) = \int \int X_1 X_2 f_{x_1, x_2}(X_1, X_2) dX_1 dX_2. \quad (3.3)$$

Under assumptions of stationarity and *homogeneity*, we have that

$$R_x(t_1, t_2, r_1, r_2) = R_x(\tau, \Delta) \quad (3.4)$$

where $\tau = t_1 - t_2$ and $\Delta = r_1 - r_2$. In this case, the function can be transformed in time and space to arrive at a so-called wavenumber-frequency spectrum

$$S_x(f, \nu) = \int \int R_x(\tau, \Delta) e^{-j2\pi(f\tau - \nu\Delta)} d\tau d\Delta \quad (3.5)$$

This spectral density function contains an intuitive notion of both the wavenumber and frequency content of a random process. Methods of estimating this quantity, such as proposed by *Illić and Harker* [1975] demand that a lot of information be collected about the system—namely taking a long time series of data at each and every one of a large number of points.

The methods explored in this experiment represent an attempt to arrive at a

similar estimate to the wavenumber-frequency PSD by making key assumptions about the nature of the random process under observation.

3.2.1 Method of interferometry

Interferometry adopts the assumption that there is a dominant mode being measured.

The method of interferometry is an old idea: A sinusoidal signal of frequency ω and wavelength λ is sampled at two points in space. The time samples are multiplied together and low-pass filtered. The multiplication results in sum (2ω) and difference (zero) frequency products, and the filter removes the sum frequency product. The zero-frequency product is proportional to the sine of the wavenumber times the distance between the sample points. The spacing between the sampling is then varied to trace out the waveform of the process.

This method works very well when there is one dominant mode being measured. The wavelength structure is obvious when the distance between the point sources is changed. Furthermore, since the output of the interferometer is usually no more than a few hertz (for reasonably slow motions of the probes), the method is well-suited to techniques of synchronous detection, or lock-in amplification [Meade, 1983].

The implementation of the interferometer in the VTF machine is shown in figure 3-6.

Two long, flexible, coaxial cables were run from the electrical feedthroughs on the top and side probes into the diagnostic cabinet. These lines were sent through small boxes designed to allow for the tips to be biased. If biased, the DC bias current is basically pulled through the 470Ω resistor and is sunk by a -150 volt power supply. The RF current passes through the capacitor and travels on to a quadrature demodulator via 250 MHz passive low pass filters. Care was taken to make sure that the distances between the probe tips and the mixers in the quadrature demodulators were equal. Each signal, the top (A) and side (B) probe signals were sent into power splitters. One half of the A and B signals were mixed with a sine and one half mixed with a cosine. The outputs of the mixers were then sent through 500 Hz 1st-order low pass filters to eliminate the sum beat waves and then into some lock-in amplifiers.

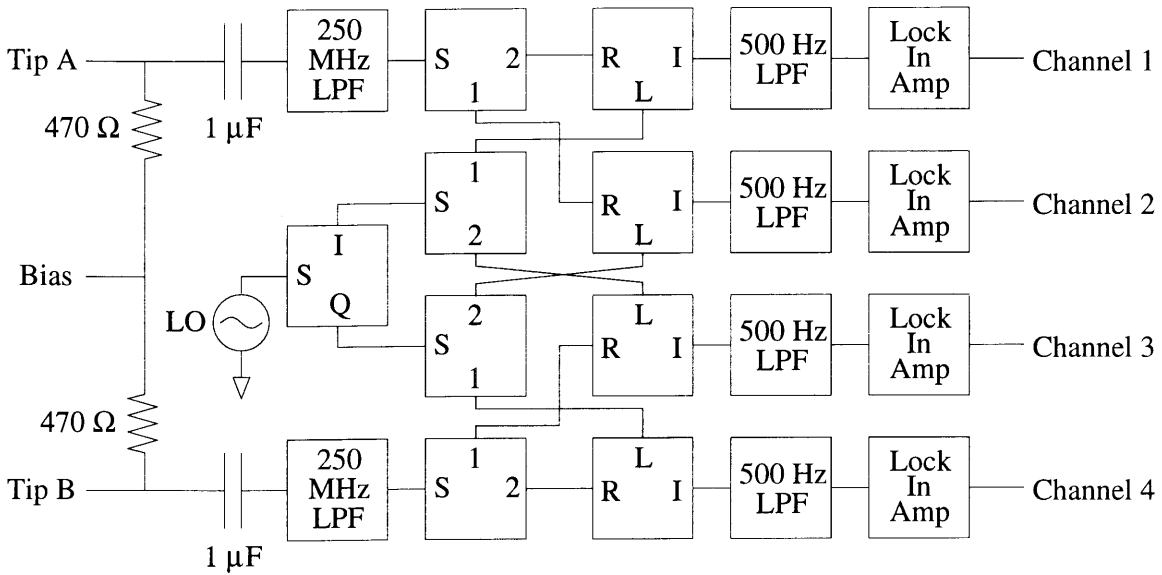


Figure 3-6: Interferometer setup in the VTF machine. “SIQ” is a power splitter featuring 0 and 90 degree outputs.

The need for the lock-in amplification is due to the low-level nature of the signals of interest. The effects that are being observed are the results of nonlinear interactions of the pump waves and the plasma. With the available power limited to about 100 W, these nonlinear effects were expected to be small. Therefore it was desirable to code the transmitted waves in some manner such that effects of the injected waves could be recognized above the background turbulence. The simplest way to do this is to turn the transmitter on and off at some low frequency, such as 500 Hz, which is a longer time scale than the growth time of the nonlinear effects under consideration. Therefore the pump wave-produced modes are square-wave modulated at 500 Hz. The lock-in amplification basically flips open and closed an RF switch connecting the probe signals to a wideband amplifier/low pass filter. Signals correlated with this switching rate are amplified and uncorrelated signals are not. One can think of this operation as mixing with a square wave, so that signals at ± 500 Hz, ± 1500 Hz, ± 2500 Hz, and so on, around the local oscillator frequency of the mixers are sent to baseband. Since first order filtering is applied to the incoming signal above 500 Hz, and the square wave harmonics in both the incoming signal and the switching waveform roll off as second order, the contributions to the baseband signals from the

harmonics will fall off as 5th order above the fundamental, so therefore phenomena at ± 500 Hz around the carrier frequency are recovered almost completely.

The output of the switching stage inside the lock-in amplifier is sent through a narrow (~ 20 Hz), high-order low pass filter to get rid of all non-baseband products of the incoming signal and the square switching modulation. Once the four signals are recorded by a digitizer, the multiplication can be performed in a computer and the wavelength pattern observed. In the absence of a dominant pump field, Fourier-analysis may recover the wavenumber spectrum.

This interferometer/lock-in method was tested in free space in the control room using microwave-range components (the freespace wavelength at 60 MHz is too long to measure in the control room). Basically, an RF source was set up to launch a 2.45 GHz microwave via a half-wave dipole antenna. A hand-held receiving dipole was attached to a quadrature demodulator, whose sine and cosine outputs were sent into lock-in amps. The local oscillators and RF inputs to the mixer were locked to the same carrier, so the demodulator performed the multiplication. The results were dramatic. With the lock-in amplification, volt-level wavelength-pattern measurements could be made by moving around the handheld dipole, as opposed to millivolt-level signals recorded without the lock-in.

In the plasma, the signals of interest are not necessarily phase-locked to the launching antenna, so two plasma probes are required to retrieve the signals to be multiplied.

The basic problem with this method is that the frequency window that is passed by the lock-in amps is finite width. Therefore signals up to ± 20 Hz around the carrier frequency will be digitized. If the signals in question are wideband, then when these signals are multiplied, the resultant data series will contain variations which are due both the wavelength patterns and the beating between the various frequencies in the ± 20 Hz window. This problem was examined long before experiments were carried out. The conclusion was that for a real-time scanning probe diagnostic, there is no simple way to reduce the frequency window to zero and still allow variations due to the wavelength pattern to pass through.

The only hope is that the variations due to the wavelength pattern are larger than

the variations due to the beating of the different frequencies within the frequency window.

After performing the experiments, the conclusion was that this hope is realized for the pump waves, but not so for the daughter waves. The pump wave is actually easy to pick out from the resulting multiplication (essentially the cross-spectral power density at the LO frequency). Consider figure 3-7. Two traces are shown. One trace is the output of the interferometer for the probes scanning apart vertically for a full 14 seconds (at about 1 cm/s). The second trace is the output in the case that the probes scan apart vertically for 6 seconds and are then stopped. Clearly, what is seen in these graphs is the wavefront pattern of the pump wave, because (1) the trace obviously stops varying when the probe motion stops and (2) the observed wavelength is very long—we only see perhaps a third of a wavelength here. This is because the wavefronts in the pump wave are nearly perpendicular to the direction of the probe scan.

In the case of the daughter waves, the wavelength pattern is broadband, and can in principle be recovered by performing Fourier analysis of the cross-power spectral density (CSD) $H(\omega, x)$ (the quantities shown in figure 3-7) to arrive at $S(\omega, k)$. Fourier transforms were made of data sets taken with and without the probes scanning. The hope is that if the pump wave excites significant short-scale perpendicular-propagating waves, then data sets taken with the probes scanning through those wavefields should have more low-frequency power in their $H(\omega, x)$ function than those taken without scanning. However, time-mixing of the broadband daughter wave signals within the receiver window were expected to obscure the patterns of the spatial wavefields.

This is confirmed in figure 3-8. The moving probe case should feature more low frequency power because the wavefronts are being traversed, but this is not seen. The conclusion therefore is that if there exist short-scale modes, their wavelength cannot be recovered from this procedure, because of the mixing (beating) of time-varying modes that fall into the range of the receiver window.

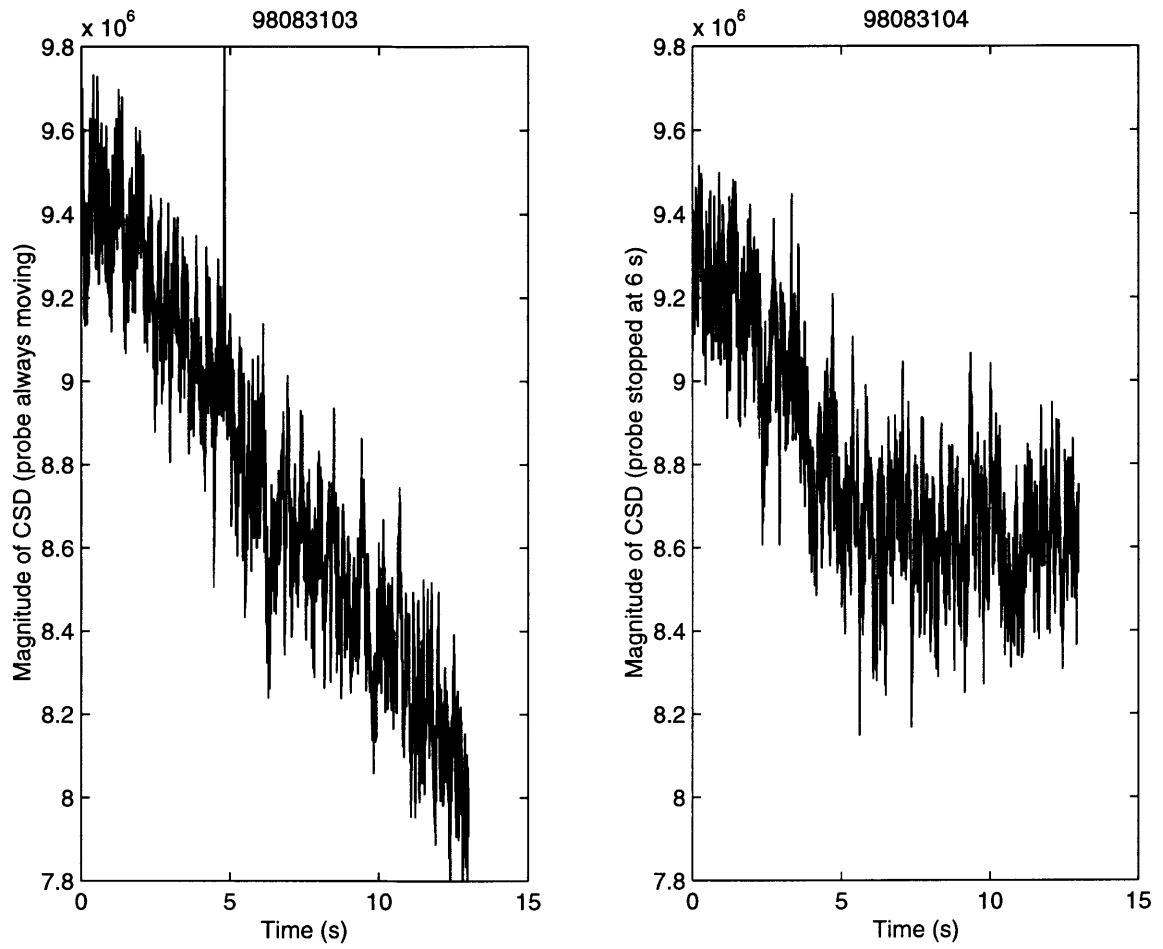


Figure 3-7: Pump wave patterns. On the left, the probes scan for 14 seconds. On the right, the scanning is stopped after 6 seconds.

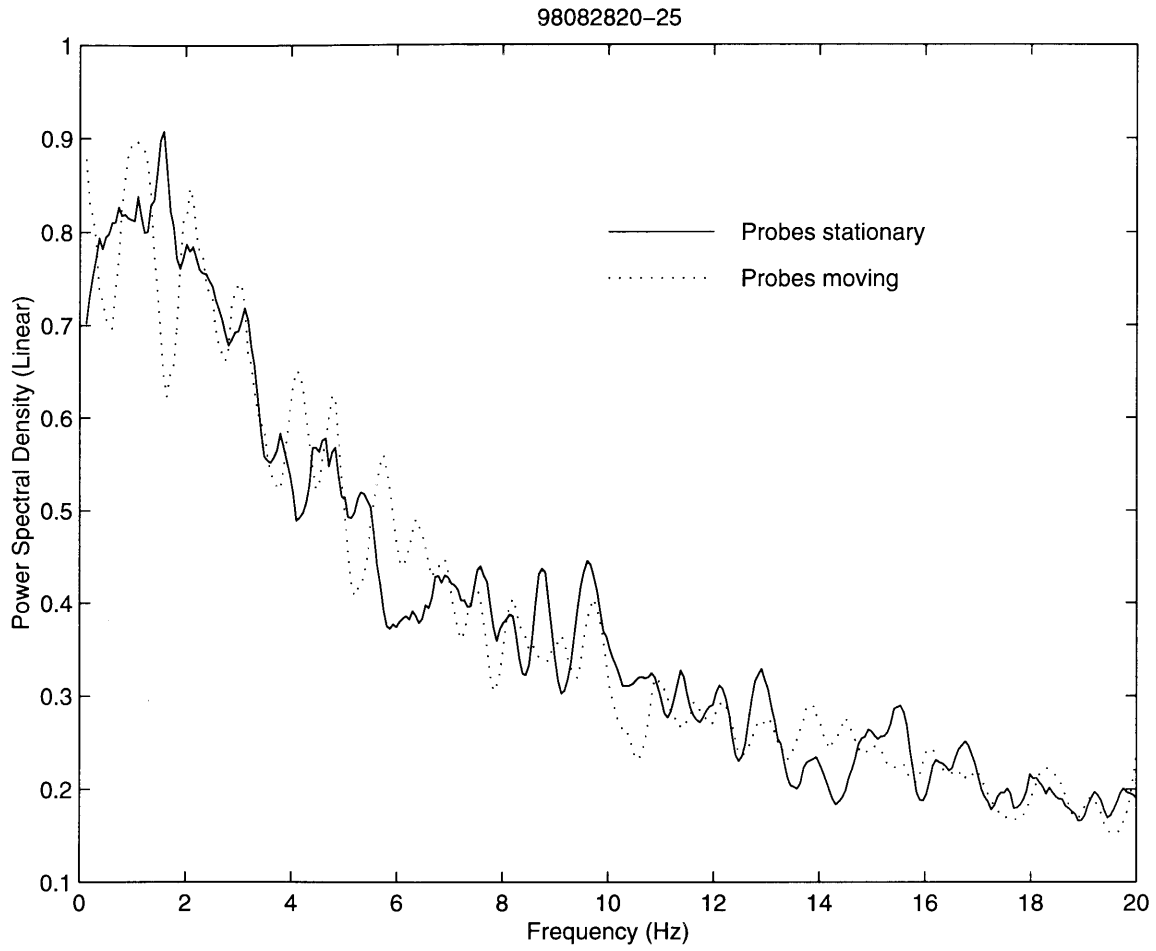


Figure 3-8: Comparison of low frequency power spectra for moving and stationary probes.

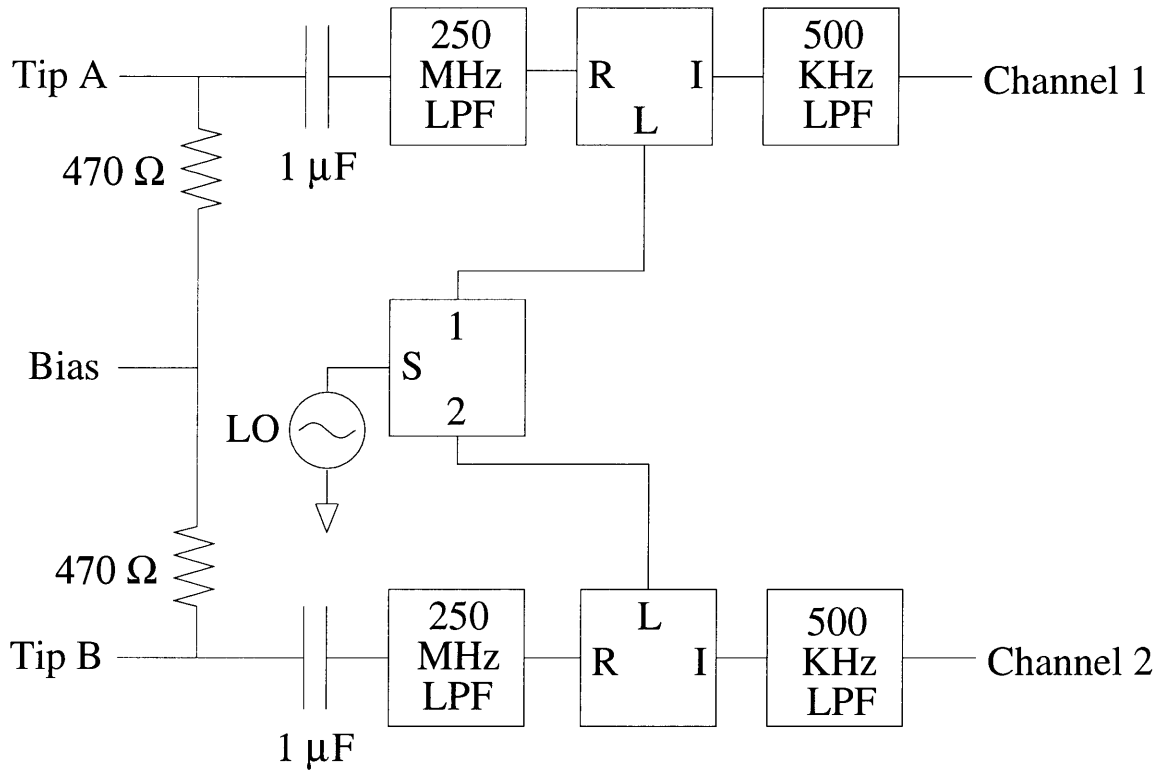


Figure 3-9: Phase lag measurement setup.

3.2.2 Statistical phase-lag measurements

Statistical phase-lag measurements assume that the temporal and spatial structure of the plasma has the form of plane waves, so that the wavenumber can be recovered from knowing a phase-lag and a frequency. The key idea here, however, is that this phase lag is statistical in nature and the shape of the wavenumber distribution can be recovered from a histogram of measured phase lags.

Measurements of phase lag statistics were made, following the procedures of *Beall et al.* [1982]. The experimental setup is shown in figure 3-9. The setup is similar to the setup for the interferometry, except that the signals are intercepted at the output of the mixers. The two cosine signals are sent through a 5th order low pass filter with 500 kHz rolloff and then sampled by a 2 MHz digitizer with 64k of memory for each channel. If the LO frequency for the mixer is chosen to be about 250 kHz below the pump wave frequency, then the pump wave and ± 250 kHz of sidebands are digitized. Since the pump frequency is set at a finite frequency there is only need

to digitize the cosine outputs of the mixer. In other words, the positive and negative images of the pumpwave and its sidebands do not significantly overlap, and therefore there is no need to digitize the even and odd parts of the baseband signal in order to recover the original signal. The overlapping which does occur between the positive and negative images is down by several orders of magnitude, according to the frequency spectra shown in the single probe measurements.

The phase lag statistics method basically breaks the time series into a large number of bins, and an FFT is performed on each bin. The phase at each frequency for the two signals is drawn from the FFT for each bin. The phase lag of the two signals is calculated and converted to a wavenumber, given the frequency, and then a weighted histogram of the phase lags is compiled for all the bins. Note that this is a weighted histogram, so that contributions to the histogram are weighted by their power in the FFT of a particular bin. The final histogram is referred to as the local spectral density $S_l(\mathbf{k}, \omega)$ and is shown by *Beall et al.* [1982] to converge to the true wavenumber-frequency spectrum $S(\mathbf{k}, \omega)$.

Please note that the 5th order low-pass filters, a program for controlling the two 2 MHz digitizers, and a program for compiling the phase lag statistics were provided by Nathan Dalrymple.

Unfortunately, the phase lag statistical method basically detects the most powerful modes of the system. For example, if there is a small signal with one phase lag from probe to probe riding on top of a large signal with a different phase lag from probe to probe, the angle measurements will obviously respond to the large amplitude waves. Therefore, one cannot make measurements, for example, of short-scale perpendicular modes at the pump wave frequency. Furthermore, the pump wave itself is spread slightly in frequency by the plasma, and therefore the observed phase lag from one probe to the other tends to wander very slowly, violating the ergodicity requirements of the method. For these two reasons, the local spectral density is not a good estimator around the frequencies of strong tones in the plasma.

With these considerations in mind, six data sets will be presented. Please refer to figures 3-10 through 3-15. The low (near-zero) frequency spectra will be introduced

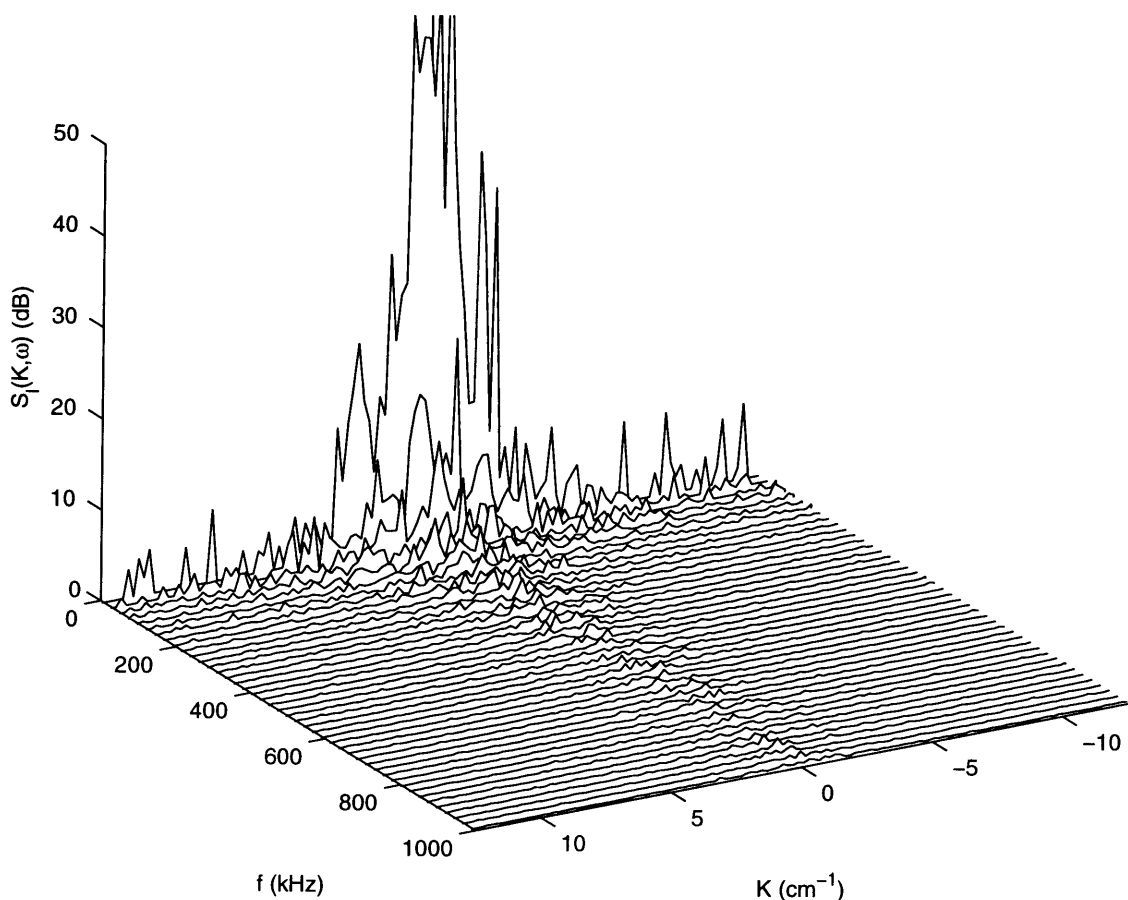


Figure 3-10: Low frequency spectrum, probes spaced perpendicular to the field, in presence of pump wave. Frequency axis is true frequency.

first, as they are better behaved than the spectra at the pump frequency, and provide a better introduction to the data.

Figures 3-10 and 3-11 show the perpendicular low-frequency modes with and without the pump wave on. Clearly, modes are seen to be excited by the addition of the pump field.

Figures 3-12 and 3-13 show the parallel low-frequency modes with and without the pump wave on. Notice that the excitation of parallel modes away from 0 Hz by the pump wave is weaker than the excitation of perpendicular modes away from 0 Hz as seen in figure 3-10. Although it takes an optimistic eye to see this distinction, the author believes that this difference is significant, and can be better demonstrated with further experiments.

99011249

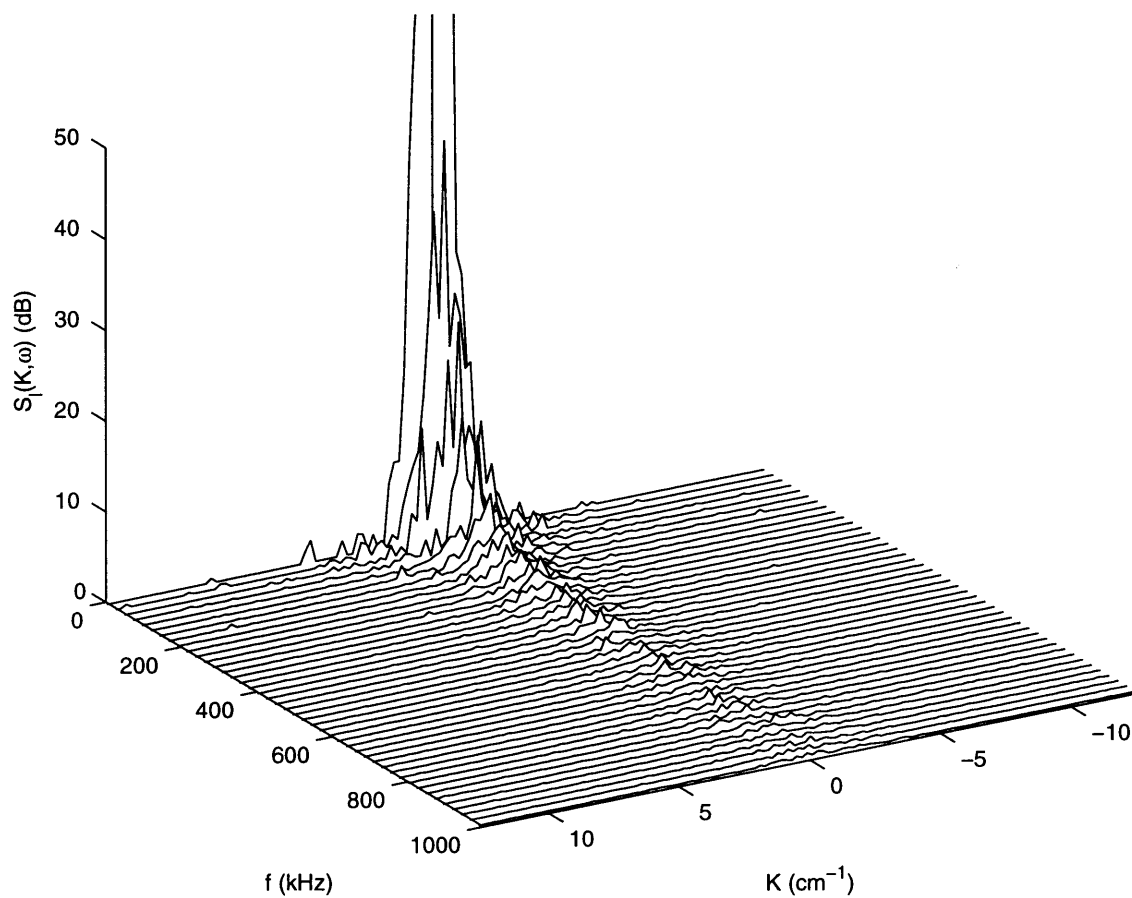


Figure 3-11: Low frequency spectrum, probes spaced perpendicular to the field, with no pump wave. Frequency axis is true frequency.

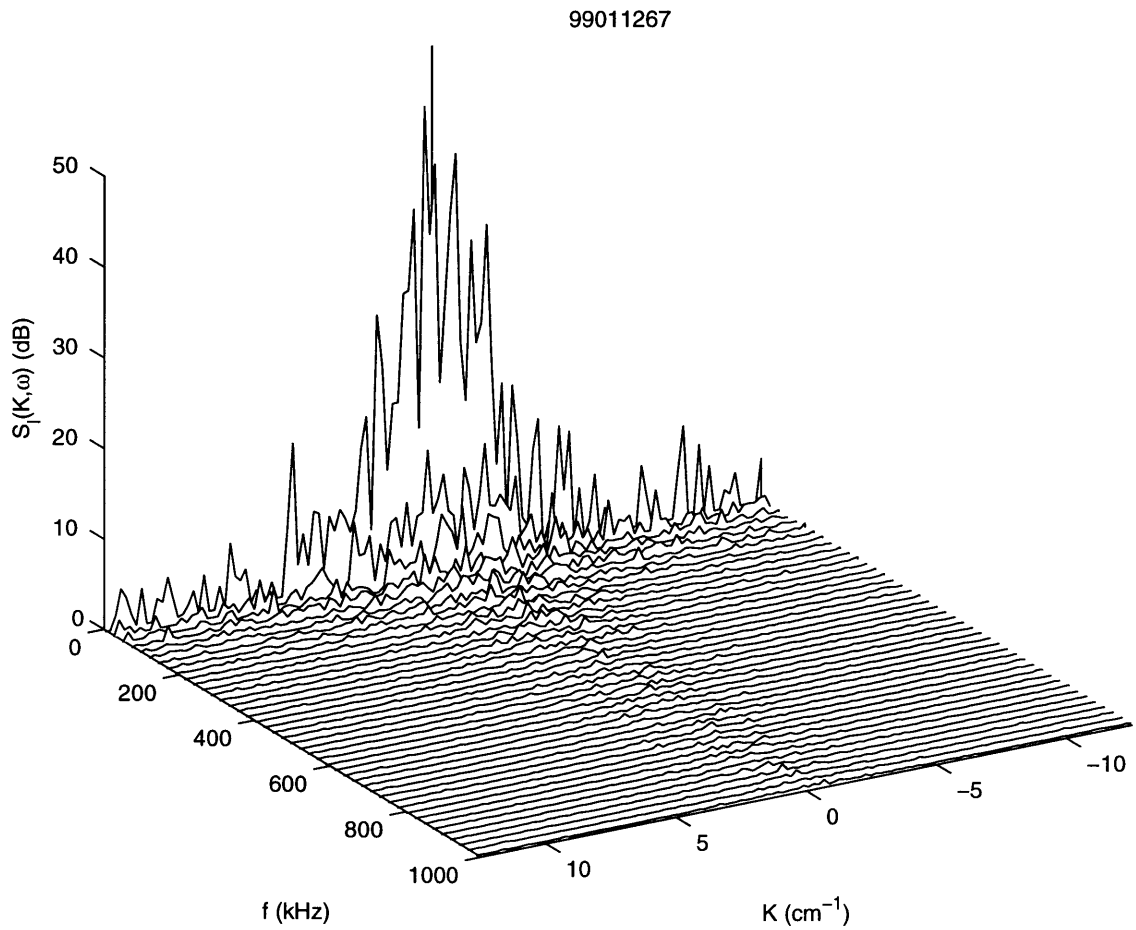


Figure 3-12: Low frequency spectrum, probes spaced parallel to the field, in presence of pump wave. Frequency axis is true frequency.

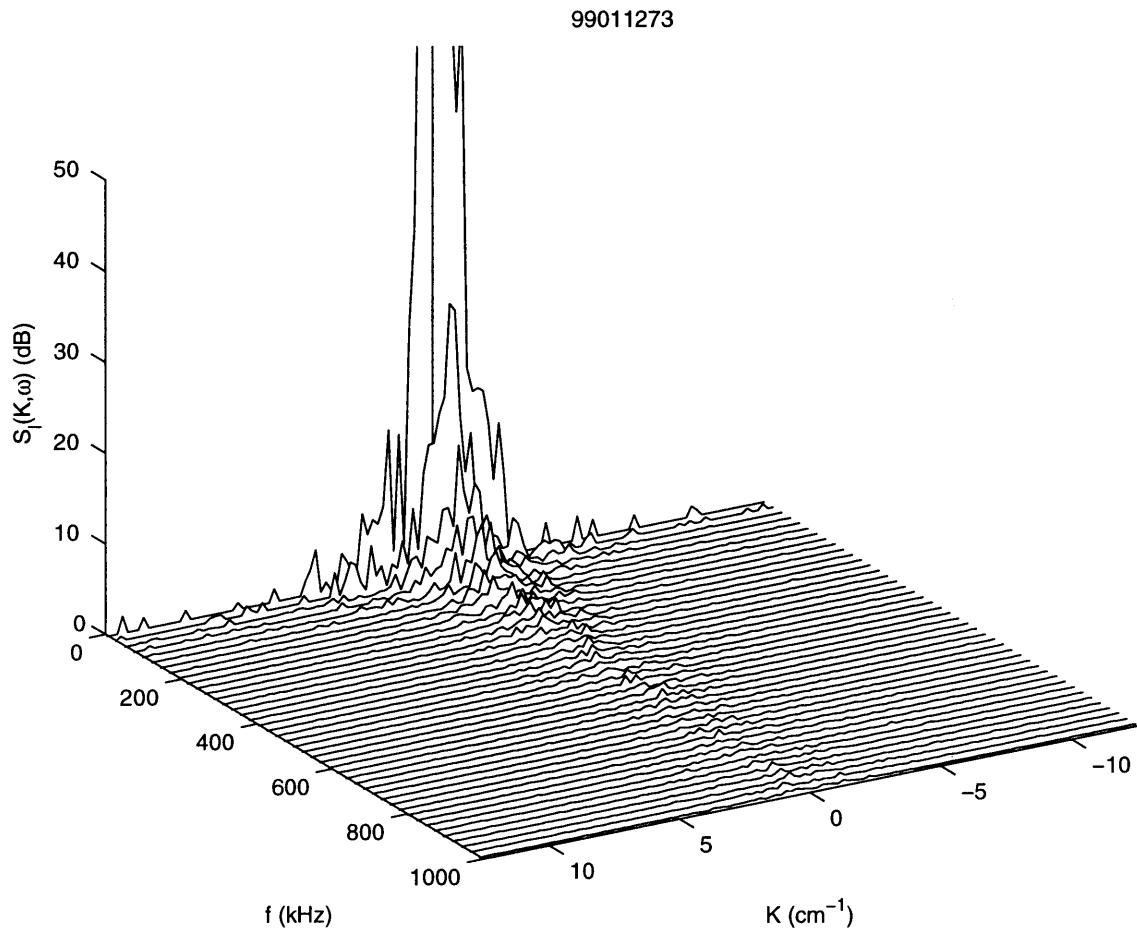


Figure 3-13: Low frequency spectrum, probes spaced parallel to the field, with no pump wave. Frequency axis is true frequency.

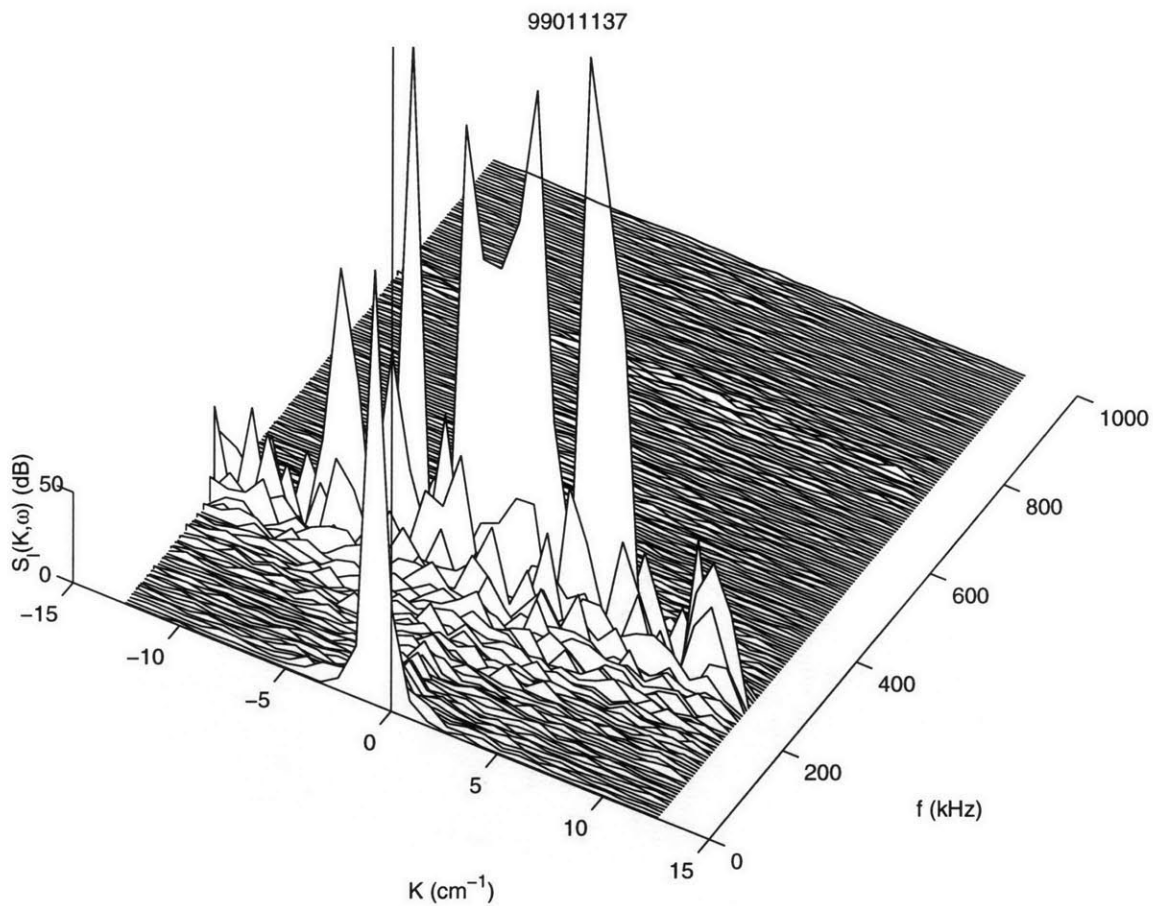


Figure 3-14: Spectrum around pump wave, probes spaced perpendicular to the field. Frequency axis 0-1 MHz corresponds to frequency range 35.89 MHz to 36.89 MHz before mixing, so that pump is at 250 KHz. Graph has been turned to show downshifted spectrum.

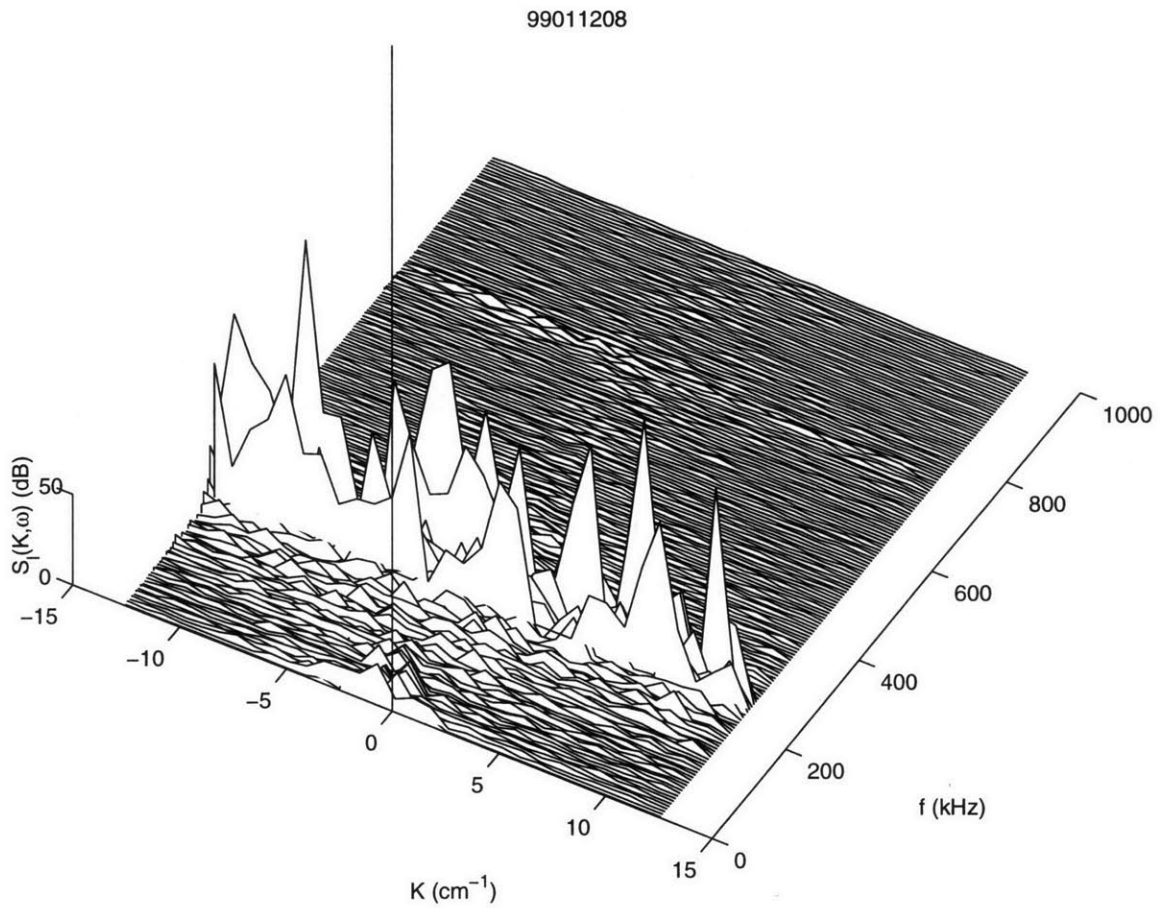


Figure 3-15: Spectrum around pump wave, probes spaced parallel to the field. Frequency axis 0-1 MHz corresponds to frequency range 35.89 MHz to 36.89 MHz before mixing, so that pump is at 250 KHz. Graph has been turned to show downshifted spectrum.

Finally, figures 3-14 and 3-15 have been oriented to show the intense frequency spectrum downshifted from the pump wave frequency. It is very clear from these pictures that these downshifted modes are perpendicular rather than parallel, as the modes are basically not visible in the parallel spectrum. Note that the pump wave is not well-represented, presumably due to the ergodicity concerns raised earlier.

These exciting results, in conjunction with the single probe measurements, are evidence to suggest the simultaneous production of perpendicular-propagating lower hybrid waves with zero-frequency modes, as was predicted by *Lee et al.* [1984].

It is the author's opinion that it is worth pursuing the statistical phase lag measurement technique further before turning to the methods of *Illić and Harker* [1975]. The phase lag technique will certainly find application in the study of field-aligned modes giving rise to the mechanism of *Groves et al.* [1988] in the beam plasma. These field-aligned modes are expected from the instability arguments given in Appendix A.

Chapter 4

Conclusions

The experiments provided information about the daughter waves generated during pump wave injection near the lower hybrid frequency. A single-point frequency spectrum certainly provided evidence of nonlinear interactions in terms of a very broadened spectrum around the pump wave. There was also the generation of low-frequency modes during the transient measurements which cannot be accounted for in terms of probe sensitivity alone, and therefore must be due to wave-plasma interactions, possibly the mechanism of *Lee et al.* [1984].

The interferometry (scanning probe) method failed to observe field structure at any frequency except for the pump wave. The reason appears to be that the mixing of the wideband time signals over the finite bandwidth of the receiving apparatus obscures the low frequency signals due to the spatial variation of the wavefields being swept out over time. The method of interferometry is therefore not useful for nonlinear processes producing wideband emissions. The successful interferometry of *Chang et al.* [1969] and *Bellan et al.* [1976] were performed on narrowband processes.

Measurements of the wavenumber-frequency spectra were made for the off-pump wave frequency modes and for the low-frequency modes, using the method of statistical phase lags [*Beall et al.*, 1982]. Predictions of *Lee et al.* [1984] were suggested by the data. The method failed to measure any wavemodes beside the pump at the pump wave frequency because the angle measurement is not sensitive to the small-scale daughter waves riding on top of the pump field signals. Furthermore, the pump

signal in the plasma failed to produce meaningful wavenumber information because it violated the ergodicity requirement of the method. This method may also be put to use in analyzing the off-pump frequency wavefields generated, for example, in the microwave range in the VTF, to help understand the wavenumber-frequency characteristics of the parametric decay instability and the production of anti-Stokes waves. In fact, this study is being pursued by another graduate student, Nathan Dalrymple.

To complete the above study, an important direction is to attempt to obtain long time series of data at many discrete points in the plasma following the method of *Illić and Harker* [1975]. This allows one to estimate the space-time autocorrelation function, without making assumptions about the processes, other than stationarity and ergodicity. This method was in fact done in the VTF plasma previously [*Zimmerman et al.*, 1993] albeit at only ten discrete positions spaced about 1 cm apart and at kHz-range frequencies. To adequately sample the region of the nonlinear interactions, the author proposes 50 or 100 measurements at discrete locations, spread by perhaps 0.5 mm. Since the major reason this was not carried out was the slop in the motor drive mechanism, the motor would not be used. Rather, the motor shaft would be turned by hand and the position could be set accurately in terms of incrementing the screw drive by a certain number of degrees after every shot. It is certainly a time-consuming job, but the author has opportunity to complete the task before an upcoming conference in August, 1999.

Other ideas are good for future work. First, the side probe could be redesigned to be studier, and therefore allow one to run the experiment in the beam plasma, where it is presumed that there are field-aligned structures generated by the current. Operation in beam plasmas will allow predictions of *Groves et al.* [1988] to be tested. This work may have to wait until a high-frequency (greater than 40 MHz) amplifier arrives in the lab, as the one currently being used for that range had to be returned to the rental company. Alternatively, one can use the background bremsstrahlung whistler emissions to study this mechanism [*Lee et al.*, 1998]. The zero-frequency modes needed by *Groves et al.* [1988] have not been measured in a conclusive way [*Moriarty*, 1996], so the two-probe apparatus could be put to work for that job.

The effects of changing the pump frequency have not been studied. By changing the pump frequency, one may be able to sweep over enough frequency to verify the dispersion relation of the daughter waves. The problem here is in the tuning apparatus. An efficient manner would have to be devised for retuning the antenna. The current method of acquiring a network analyzer and stub tuning with various lengths of cables is not efficient. The author suggests buying permanent trombone-line sections and stubs and setting up the crude network analyzer of power splitters and mixers given in chapter 2 on a permanent basis.

Other possible measurements include making an accurate study of the electric field strengths at the target. A calibrated receiver such as a balanced dipole, or even a loop probe would be able to deduce this field. These measurements would be particularly useful so that one could determine where they stand in relation to the threshold electric fields for instabilities to be excited. If it becomes clear that one is indeed near the threshold of instability in these cases, it may be worthwhile to redesign the probes so that they could be located in a position where they would see a stronger pump field. Alternatively, larger RF power amplifiers may be used. The current antenna system could easily be run in pulsed mode up to several hundred watts.

Appendix A

Source mechanism of field-aligned irregularities

This chapter outlines a way that field-aligned irregularities can be produced in the VTF machine. The VTF plasma contains cross-field density gradients that can become destabilized by charge flow in the plasma. This treatment follows *Riddolls* [1997a].

A.1 Steady-state drifts

Let us first examine the particle drifts which are responsible for destabilizing the plasma density gradient.

A.1.1 Ion Pedersen drift

Consider a plasma in a Cartesian co-ordinate system. Let us suppose there is a magnetic field in the z -direction and an electric field in the x -direction. Let us also assume that the plasma is weakly ionized with collisions occurring between the neutral and ionized particles. The equation of motion of a particle in steady-state is

$$0 = q(\mathbf{E} + \mathbf{v} \times \mathbf{B}) - m\nu\mathbf{v} \tag{A.1}$$

where ν is the collision frequency between the ionized and neutral particles. The above expression can be written

$$\mathbf{v} - \frac{\Omega}{\nu} \mathbf{v} \times \hat{\mathbf{z}} = \frac{q}{m\nu} \mathbf{E} \quad (\text{A.2})$$

where Ω is the gyrofrequency.

In the limit $\frac{\Omega}{\nu} \ll 1$, the above equation predicts that the particle will drift in the direction of the background electric field. This is known as Pedersen drift. In the limit $\frac{\Omega}{\nu} \gg 1$, the resulting motion is Hall drift. This drift is perpendicular to both fields

$$\mathbf{v} = \frac{\mathbf{E} \times \hat{\mathbf{z}}}{B}. \quad (\text{A.3})$$

In general, a species in the plasma will drift at an angle somewhere between the direction of \mathbf{E} and the direction of $\mathbf{E} \times \mathbf{B}$. Both the F-region ionosphere and the VTF plasma have the feature $\frac{\nu_e}{\Omega_e} \ll \frac{\nu_i}{\Omega_i}$. As a result, there is a stronger tendency for ions than electrons to drift in the direction of the electric field. These drifts have a profound consequence on non-uniform plasmas because they can cause polarization, leading to instability.

A.1.2 Field-aligned current

When plasma is being formed in the VTF there is a small component of \mathbf{E} along the magnetic field of the machine which drives the electrons along the field. To represent this drift of electrons, we will add a steady-state drift $v_{e0} \hat{\mathbf{z}}$ into our calculations.

Field-aligned current can also occur in the auroral ionosphere as a result of electron precipitation from the magnetosphere. The triggering of these precipitation events are an active area of research.

A.1.3 Gravity and equivalent gravity drifts

In the equatorial ionosphere, the plasma suffers a drift due to the effects of gravity. This motion is known as the $\mathbf{g} \times \mathbf{B}$ drift

$$\mathbf{v}_g = \frac{m \mathbf{g} \times \mathbf{B}}{q B^2}. \quad (\text{A.4})$$

Note that ions and electrons drift opposite directions in this motion.

While the effect of gravity is negligible in the VTF machine, there is a different mechanism which can produce a plasma drift very similar to the ionospheric $\mathbf{g} \times \mathbf{B}$ drift. The fact that the field lines in the VTF machine are curved and vary spatially in strength results in the curved vacuum field drift

$$\mathbf{v}_c = \frac{m}{q} \left(v_{\parallel}^2 + \frac{1}{2} v_{\perp}^2 \right) \frac{\mathbf{R}_c \times \mathbf{B}}{R_c^2 B^2}, \quad (\text{A.5})$$

where \mathbf{R}_c is the major radius of the curved field line. As a result, the VTF plasma drifts as if a gravitational force was being applied in the radial direction, hence the name “equivalent gravity”.

A.2 Consequences of a plasma density gradient

A.2.1 Analysis of instability

Plasmas with a density gradient can easily become unstable in the presence of steady-state plasma drifts such as those described above. The goal of this section is to arrive at a description of the turbulence that is generated by these instabilities. Specifically, we will find the dispersion relation of waves generated by the instability during its linear stage of growth. Consider the geometry shown in figure A-1.

As before, a magnetic field is in the z-direction, and an electric field is in the x-direction. Let us add a density gradient in the negative y-direction, an ion Pedersen drift in the x-direction, and field-aligned current in the z-direction.

The instability begins when there is a small fluctuation in the density gradient.

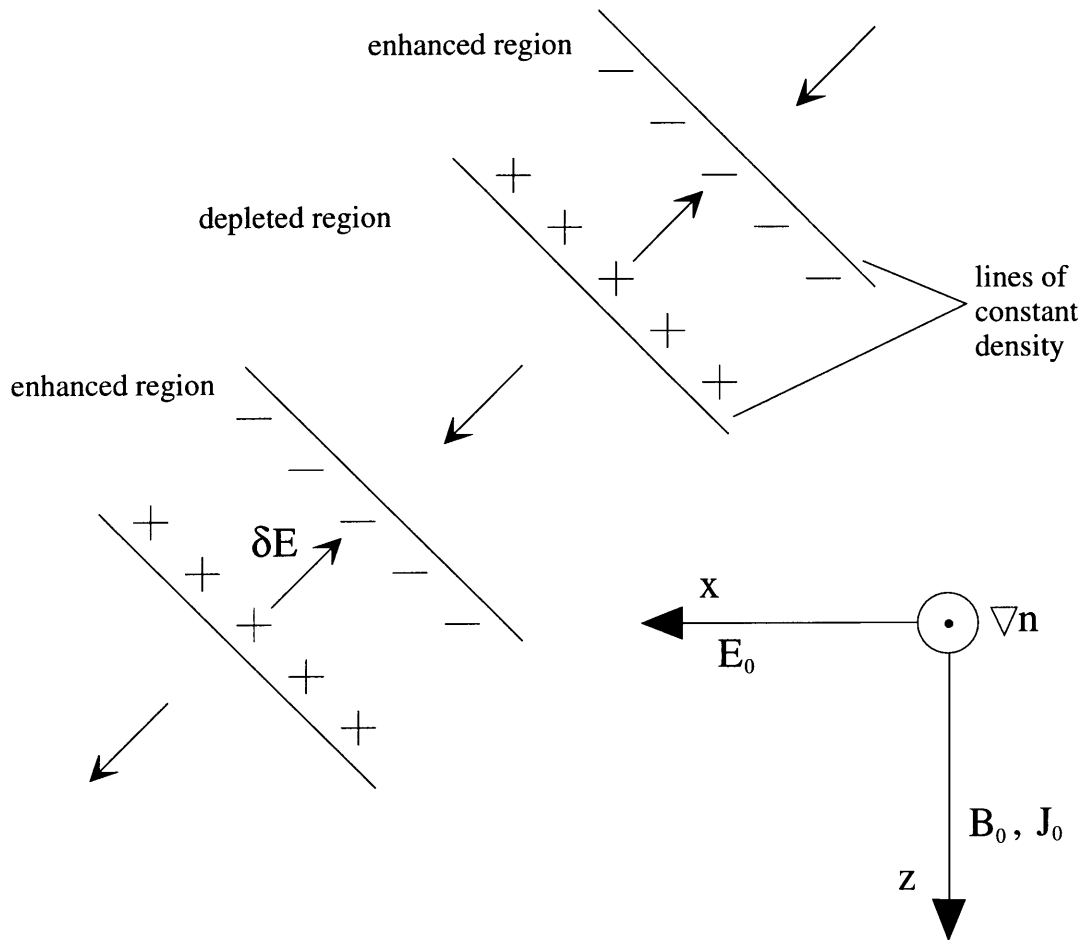


Figure A-1: Instability Mechanism

For purposes of discussion, let us consider a sinusoidal perturbation in the x-z plane. In the diagram I have shown the lines of constant density, with the regions of enhancement and depletion marked.

Within the region of enhancement, there is a component of ion drift along the background electric field \mathbf{E}_0 . Similarly, there is current consisting of electrons drifting along the background magnetic field, denoted by J_0 in the figure. The ions and electrons accumulate at the edges of the enhancement and are depleted at the opposite edges. This polarization leads to small electric fields $\delta\mathbf{E}$. Since these electric fields are at an angle to the background magnetic field, they cause the plasma in the enhancement to drift in the direction of $\delta\mathbf{E} \times \mathbf{B}$

$$\delta\mathbf{v}_E = \frac{\delta\mathbf{E} \times \mathbf{B}}{B^2}. \quad (\text{A.6})$$

This drift is against the density gradient, thus the perturbation is unstable.

The mathematical description of this instability uses the fluid equations. We will consider a singly charged ion species in the rest frame of neutrals

$$\frac{\partial n_\alpha}{\partial t} + \nabla \cdot (n_\alpha \mathbf{v}_\alpha) = 0 \quad (\text{A.7})$$

$$m_\alpha n_\alpha \left[\frac{\partial \mathbf{v}_\alpha}{\partial t} + (\mathbf{v}_\alpha \cdot \nabla) \mathbf{v}_\alpha \right] = -\nabla p_\alpha + q_\alpha n_\alpha (\mathbf{E} + \mathbf{v}_\alpha \times \mathbf{B}) - n_\alpha m_\alpha \nu_{\alpha n} \mathbf{v}_\alpha - \mathbf{R}_\alpha \quad (\text{A.8})$$

$$\nabla \cdot \mathbf{E} = \frac{q}{\epsilon_0} (n_i - n_e). \quad (\text{A.9})$$

I have used the subscript α to denote that the equation applies both for electron and ions. \mathbf{R}_α represents the momentum transfer due to unlike-species collisions. We will linearize these expressions in the following manner: the density will be expressed as $n_\alpha = n_0 + \delta n_\alpha$, where n_0 is invariant in time and δn_α is a small time- and space-varying perturbation. The fluid element velocity will be expressed in a similar way, $\mathbf{v}_\alpha = \mathbf{v}_{\alpha 0} + \delta \mathbf{v}_\alpha$, except that now, $\mathbf{v}_{\alpha 0}$ is assumed to be uniform in space and time.

Under these assumptions, the continuity equation for the perturbations is

$$\frac{\partial}{\partial t} \delta n_\alpha + \mathbf{v}_{\alpha 0} \cdot \nabla \delta n_\alpha + \delta \mathbf{v}_\alpha \cdot \nabla n_0 + n_0 \nabla \cdot \delta \mathbf{v}_\alpha = 0. \quad (\text{A.10})$$

Assuming the perturbations are proportional to $e^{i(\mathbf{k} \cdot \mathbf{r} - \omega t)}$ and that the wavelength is short compared to the density gradient, the continuity equation can be transformed in the usual way

$$-i\omega \delta n_\alpha + \mathbf{v}_{\alpha 0} \cdot i\mathbf{k} \delta n_\alpha + \delta \mathbf{v}_\alpha \cdot \nabla n_0 + n_0 i\mathbf{k} \cdot \delta \mathbf{v}_\alpha = 0. \quad (\text{A.11})$$

Solving for the density perturbation yields

$$\delta n_\alpha = \frac{\delta \mathbf{v}_\alpha \cdot (\nabla n_0 + n_0 i\mathbf{k})}{i\omega - \mathbf{v}_{\alpha 0} \cdot i\mathbf{k}}. \quad (\text{A.12})$$

Next, we will examine the momentum equation. It will be solved in two stages: first, for the ambient quantities, and second, for the perturbation quantities. For the ambient quantities, the linearized momentum equation is

$$\mathbf{v}_{\alpha 0} \times \mathbf{B}_0 = \frac{m_\alpha \nu_\alpha}{q_\alpha} \mathbf{v}_{\alpha 0} - \mathbf{E}_0. \quad (\text{A.13})$$

The pressure term has been neglected for simplicity, the effect of electron-ion collisions has been lumped into an effective electron collision frequency $\nu_e \simeq \nu_{ei} + \nu_{en}$ and ion-electron collisions have been neglected ($\nu_i \simeq \nu_{in}$). To eliminate the cross product, let us cross both sides with \mathbf{B}_0

$$(\mathbf{v}_{\alpha 0} \times \mathbf{B}_0) \times \mathbf{B}_0 = \frac{m_\alpha \nu_\alpha}{q_\alpha} \mathbf{v}_{\alpha 0} \times \mathbf{B}_0 - \mathbf{E}_0 \times \mathbf{B}_0 \quad (\text{A.14})$$

and substitute for $\mathbf{v}_{\alpha 0} \times \mathbf{B}_0$. Note that $(\mathbf{v}_{\alpha 0} \times \mathbf{B}_0) \times \mathbf{B}_0 = -B_0^2 \mathbf{v}_{\alpha 0 \perp}$. We are left with

$$-B_0^2 \mathbf{v}_{\alpha 0 \perp} = \frac{m_\alpha \nu_\alpha}{q_\alpha} \left(\frac{m_\alpha \nu_\alpha}{q_\alpha} \mathbf{v}_{\alpha 0} - \mathbf{E}_0 \right) - \mathbf{E}_0 \times \mathbf{B}_0. \quad (\text{A.15})$$

Considering components of the above equation, the total drift is

$$\mathbf{v}_{\alpha 0} = \mathbf{v}_{\alpha 0 \perp} + \mathbf{v}_{\alpha 0 \parallel} = \frac{q_{\alpha} m_{\alpha} \nu_{\alpha} \mathbf{E}_{0 \perp} + q_{\alpha}^2 B_0 \mathbf{E}_{0 \perp} \times \hat{\mathbf{z}}}{m_{\alpha}^2 \nu_{\alpha}^2 + q_{\alpha}^2 B_0^2} + \frac{q_{\alpha} \mathbf{E}_{0 \parallel}}{m_{\alpha} \nu_{\alpha}}. \quad (\text{A.16})$$

However, $q_{\alpha}^2 B_0^2 \gg m_{\alpha}^2 \nu_{\alpha}^2$, therefore

$$\mathbf{v}_{\alpha 0} = \frac{1}{B_0} \mathbf{E}_{0 \perp} \times \hat{\mathbf{z}} + \frac{\nu_{\alpha}}{B_0 \Omega_{\alpha}} \mathbf{E}_{0 \perp} + \frac{\Omega_{\alpha}}{B_0 \nu_{\alpha}} \mathbf{E}_{0 \parallel}. \quad (\text{A.17})$$

Note that Ω_e is a negative quantity. Let us consider an ambient electric field in the x-direction: $\mathbf{E}_0 = E_0 \hat{\mathbf{x}}$. We will also consider an additional small electric field in the z-direction, although the high conductivity of the plasma along the magnetic field makes it more practical to express $\frac{\Omega_{\alpha}}{\nu_{\alpha} B_0} \mathbf{E}_{0 \parallel}$ as simply $v_{\alpha 0 z} \hat{\mathbf{z}}$. Under these assumptions, the ambient drift is

$$\mathbf{v}_{\alpha 0} = \frac{\nu_{\alpha} E_0}{\Omega_{\alpha} B_0} \hat{\mathbf{x}} - \frac{E_0}{B_0} \hat{\mathbf{y}} + v_{\alpha 0 z} \hat{\mathbf{z}}. \quad (\text{A.18})$$

Now let us analyze the momentum equation for the perturbations. Assuming that the perturbations are proportional to $e^{i(\mathbf{k} \cdot \mathbf{r} - \omega t)}$, the equation transforms to

$$[-i\omega + (\mathbf{v}_{\alpha 0} \cdot i\mathbf{k})] \delta \mathbf{v}_{\alpha} = \frac{q_{\alpha}}{m_{\alpha}} (\delta \mathbf{E} + \delta \mathbf{v}_{\alpha} \times \mathbf{B}_0) - \nu_{\alpha} \delta \mathbf{v}_{\alpha}. \quad (\text{A.19})$$

With the help of the definition

$$\nu'_{\alpha} = -i\omega + \mathbf{v}_{\alpha 0} \cdot i\mathbf{k} + \nu_{\alpha}, \quad (\text{A.20})$$

we can write the momentum equation as

$$\delta \mathbf{v}_{\alpha} \times \mathbf{B}_0 = \frac{m_{\alpha} \nu'_{\alpha}}{q_{\alpha}} \delta \mathbf{v}_{\alpha} - \delta \mathbf{E}. \quad (\text{A.21})$$

This is identical to the expression for $\mathbf{v}_{\alpha 0} \times \mathbf{B}_0$, except that $\mathbf{v}_{\alpha 0} \rightarrow \delta \mathbf{v}_{\alpha}$, $\mathbf{E}_0 \rightarrow \delta \mathbf{E}$ and $\nu \rightarrow \nu'$. If we switch the symbols, we can move directly to the expression for the drift

$$\delta \mathbf{v}_{\alpha} = \frac{1}{B_0} \delta \mathbf{E}_{\perp} \times \hat{\mathbf{z}} + \frac{\nu'_{\alpha}}{B_0 \Omega_{\alpha}} \delta \mathbf{E}_{\perp} + \frac{\Omega_{\alpha}}{B_0 \nu'_{\alpha}} \delta \mathbf{E}_{\parallel}. \quad (\text{A.22})$$

Assuming that the perturbation E-fields are in the x-z plane ($\delta\mathbf{E} = \delta E_x \hat{\mathbf{x}} + \delta E_z \hat{\mathbf{z}}$) as per the physical picture of figure A-1, we find that

$$\delta\mathbf{v}_\alpha = \frac{\nu'_\alpha \delta E_x}{\Omega_\alpha B_0} \hat{\mathbf{x}} - \frac{\delta E_x}{B_0} \hat{\mathbf{y}} + \frac{\Omega_\alpha \delta E_z}{\nu'_\alpha B_0} \hat{\mathbf{z}}. \quad (\text{A.23})$$

Now we can substitute the ambient and perturbation quantities into our expression for perturbation density δn_α . For electrostatic waves, \mathbf{k} is parallel to $\delta\mathbf{E}$, so we find that

$$\delta n_\alpha = \frac{\left(\frac{\nu'_\alpha \delta E_x}{\Omega_\alpha B_0} \hat{\mathbf{x}} - \frac{\delta E_x}{B_0} \hat{\mathbf{y}} + \frac{\Omega_\alpha \delta E_z}{\nu'_\alpha B_0} \hat{\mathbf{z}} \right) \cdot (\nabla n_0 + n_0 i(k_x \hat{\mathbf{x}} + k_z \hat{\mathbf{z}}))}{i\omega - \left(\frac{\nu_\alpha E_0}{\Omega_\alpha B_0} \hat{\mathbf{x}} - \frac{E_0}{B_0} \hat{\mathbf{y}} + v_{\alpha 0z} \hat{\mathbf{z}} \right) \cdot i(k_x \hat{\mathbf{x}} + k_z \hat{\mathbf{z}})} \quad (\text{A.24})$$

$$= \frac{\frac{\nu'_\alpha k_x^2 n_0 \delta E}{\Omega_\alpha B_0 k} + \frac{\Omega_\alpha k_z^2 n_0 \delta E}{\nu'_\alpha B_0 k} + \frac{ik_x \delta E}{kB_0} \frac{\partial n_0}{\partial y}}{\omega - \frac{\nu_\alpha E_0 k_x}{\Omega_\alpha B_0} - v_{\alpha 0z} k_z}. \quad (\text{A.25})$$

Note that we have assumed $\nabla n_0 = \frac{\partial n_0}{\partial y} \hat{\mathbf{y}}$. Now let us define the susceptibility χ

$$\chi_\alpha = \frac{iq_\alpha \delta n_\alpha}{k\epsilon_0 \delta E}. \quad (\text{A.26})$$

Substituting the expression for δn_α yields

$$\chi_\alpha = \frac{in_0 q_\alpha}{\epsilon_0 B_0} \left[\frac{\frac{\nu'_\alpha k_x^2}{\Omega_\alpha k^2} + \frac{\Omega_\alpha k_z^2}{\nu'_\alpha k^2} + \frac{ik_x}{k^2 n_0} \frac{\partial n_0}{\partial y}}{\omega - \frac{\nu_\alpha E_0 k_x}{\Omega_\alpha B_0} - v_{\alpha 0z} k_z} \right]. \quad (\text{A.27})$$

For electrostatic waves, Poisson's equation is

$$1 + \chi_i + \chi_e = 0. \quad (\text{A.28})$$

The susceptibilities turn out to be much greater than unity, so Poisson's equation reduces to $\delta n_i \simeq \delta n_e$. Under the low frequency approximation $\nu'_\alpha \simeq \nu_\alpha$, we can set $\delta n_i = \delta n_e$ and solve for ω to get the dispersion relation

$$\Re(\omega) = \frac{\left(\frac{\nu_i |\Omega_e|}{\nu_e \Omega_i} - \frac{\nu_e \Omega_i}{\nu_i |\Omega_e|} \right) \frac{E_0 k_z^2}{B_0 k_x} + \left(\frac{\nu_i}{\Omega_i} + \frac{\Omega_i k_z^2}{\nu_i k_x^2} \right) k_z v_{e0z} + \left(\frac{\nu_e}{|\Omega_e|} + \frac{|\Omega_e| k_z^2}{\nu_e k_x^2} \right) k_z v_{i0z}}{\left(\frac{\Omega_i}{\nu_i} + \frac{|\Omega_e|}{\nu_e} \right) \frac{k_z^2}{k_x^2} + \frac{\nu_i}{\Omega_i} + \frac{\nu_e}{|\Omega_e|}} \quad (\text{A.29})$$

$$\Im(\omega) = \frac{\frac{-1}{n_0} \frac{\partial n_0}{\partial y} \left[(v_{i0z} - v_{e0z}) \frac{k_x}{k_z} + \left(\frac{\nu_e}{|\Omega_e|} + \frac{\nu_i}{\Omega_i} \right) \frac{E_0}{B_0} \right]}{\left(\frac{\Omega_i}{\nu_i} + \frac{|\Omega_e|}{\nu_e} \right) \frac{k_x^2}{k_z^2} + \frac{\nu_i}{\Omega_i} + \frac{\nu_e}{|\Omega_e|}}. \quad (\text{A.30})$$

If we approximate $\frac{\nu_i}{\Omega_i} + \frac{\nu_e}{|\Omega_e|} \simeq \frac{\nu_i}{\Omega_i}$, and ignore the second and fifth terms in the numerator of the real frequency expression, then we have the dispersion relation of the so-called current-convective instability [Ossakow, 1979].

$$\omega = k_z v_{e0z} + \frac{\left(\frac{-i}{n_0} \frac{\partial n_0}{\partial y} + \frac{k_x^2 |\Omega_e|}{k_x \nu_e} \right) \left[(v_{i0z} - v_{e0z}) \frac{k_x}{k_z} + \frac{\nu_i E_0}{\Omega_i B_0} \right]}{\left(\frac{\Omega_i}{\nu_i} + \frac{|\Omega_e|}{\nu_e} \right) \frac{k_x^2}{k_z^2} + \frac{\nu_i}{\Omega_i}}. \quad (\text{A.31})$$

The model of the current-convective instability was originally developed to explain how a stable plasma geometry in the auroral topside ionosphere could be unstabilized by the addition of field-aligned current. In the VTF machine, both the background fields and the field-aligned current are always present, so one is unable to observe the explicit transition from stability to instability in the laboratory experiments. For this reason I have included the effects of field-aligned current from the very beginning of the derivation given above.

Let us find out for what ratio $\frac{k_x}{k_z}$ the growth rate is maximized. This ratio will specify in what direction the excited modes will be the most intense. Let us approximate $|(v_{i0z} - v_{e0z}) \frac{k_x}{k_z}| \gg \left| \frac{\nu_i E_0}{\Omega_i B_0} \right|$ and then differentiate the growth rate expression with respect to $\frac{k_x}{k_z}$ to find the angle of maximum growth θ_{max} . The result

$$\tan \theta_{max} = \sqrt{\frac{\Omega_i |\Omega_e|}{\nu_i \nu_e}}. \quad (\text{A.32})$$

Note that θ_{max} is nearly 90 degrees for the VTF parameters $\nu_i = 2.5 \times 10^4$, $\nu_e = 2.0 \times 10^6$, $\Omega_i = 8.4 \times 10^6$, and $|\Omega_e| = 1.4 \times 10^{10}$.

Among other approximations, the above treatment has ignored the effects of inertia and equivalent gravity drifts. A proper treatment of those cases is beyond the scope of this discussion, although the process is in principle fairly straightforward. One merely needs to make the following substitutions in the previous theory:

$$\nu_\alpha \rightarrow -i\omega + \mathbf{v}_{\alpha 0} \cdot i\mathbf{k} + \nu_\alpha \quad (\text{A.33})$$

to account for momentum effects, and

$$\mathbf{v}_{\alpha 0} \rightarrow \mathbf{v}_{\alpha 0} + \mathbf{v}_c \quad (\text{A.34})$$

to account for equivalent gravity effects.

Appendix B

Whistler Ducting

This appendix is an argument that large-scaled plasma structure oriented with wavefronts along the magnetic field can trap whistlers. This treatment follows *Riddolls* [1997b]. A point of notation: we will use μ to denote index of refraction and n to denote plasma density.

B.1 Theory

Consider a plasma with field-aligned irregularities. We will concern ourselves here with “crest” irregularities, namely field-aligned enhancements of plasma density. It has been suggested that whistler waves can become trapped in these structures. The trapping relies on the ability of the structure to guide the ray path associated with the wave packet by bending the ray path towards the enhancement whenever the wave packet attempts to leave. Exactly what conditions are necessary for the enhancement to exhibit this guiding influence?

A theoretical treatment of the problem involves orienting the background magnetic field along \hat{z} , letting the plasma density vary along \hat{y} , and assuming uniformity along the \hat{x} and \hat{z} . In this model, the problem of ray tracing reduces to the repeated application of Snell’s law as the wave packet drifts in \hat{y} . The Snell’s law construction [*Smith et al.*, 1961] provides a tool for predicting the evolution of the ray path angle in an inhomogeneous medium. Since the refractive index surface in the construction

is a surface of revolution around the direction of the background magnetic field, it is sufficient to consider only the intersection of this surface and the x-y plane. Let us denote this line of intersection as $f(y)$, where $x = \mu \cos \theta$ and $y = \mu \sin \theta$. *Ducting will occur if and only if $\frac{\partial f}{\partial n} > 0$ in some finite neighborhood of a local maximum of f , or $\frac{\partial f}{\partial n} < 0$ in some finite neighborhood of a local minimum of f .* We will adopt the procedure of identifying critical points on the refractive index line $f(y)$, and then compute the sign of $\frac{\partial f}{\partial n}$ if necessary. Critical points can be found by requiring that the derivative of $f(y)$ vanish

$$\frac{df}{dy} = \frac{d(\mu \cos \theta)}{d(\mu \sin \theta)} = 0. \quad (\text{B.1})$$

A little manipulation shows that this is equivalent to

$$\frac{\frac{d\mu}{d\theta} - \mu \tan \theta}{\frac{d\mu}{d\theta} \tan \theta + \mu} = 0. \quad (\text{B.2})$$

Excluding resonance, solutions of (B.2) will involve the numerator equaling zero. To proceed, let us look at the form of the index of refraction μ for whistler modes in plasma media. It is

$$\mu^2 = 1 - \frac{X}{1 - \frac{\frac{1}{2}Y^2 \sin^2 \theta}{1-X} + \frac{1}{1-X} \sqrt{\frac{1}{4}Y^4 \sin^4 \theta + Y^2 \cos^2 \theta (1-X)^2}} \quad (\text{B.3})$$

where we have adopted the notation $X = \frac{\omega_{pe}^2}{\omega^2}$ and $Y = \frac{\omega_{ce}}{\omega}$. For our purposes, it will be more useful to normalize to the electron gyrofrequency than the wave frequency. Thus μ^2 can be written as

$$\mu^2 = 1 - \frac{2B^2(\Lambda^2 - B^2)}{2\Lambda^2(\Lambda^2 - B^2) - \Lambda^2 \sin^2 \theta + \sqrt{\Lambda^4 \sin^4 \theta + 4\Lambda^2 \cos^2 \theta (\Lambda^2 - B^2)^2}} \quad (\text{B.4})$$

where $B = \frac{\omega_{pe}}{\omega_{ce}}$ and $\Lambda = \frac{\omega}{\omega_{ce}}$. To ease the algebra, we will write the index as

$$\mu = \sqrt{1 - \frac{P}{Q}}. \quad (\text{B.5})$$

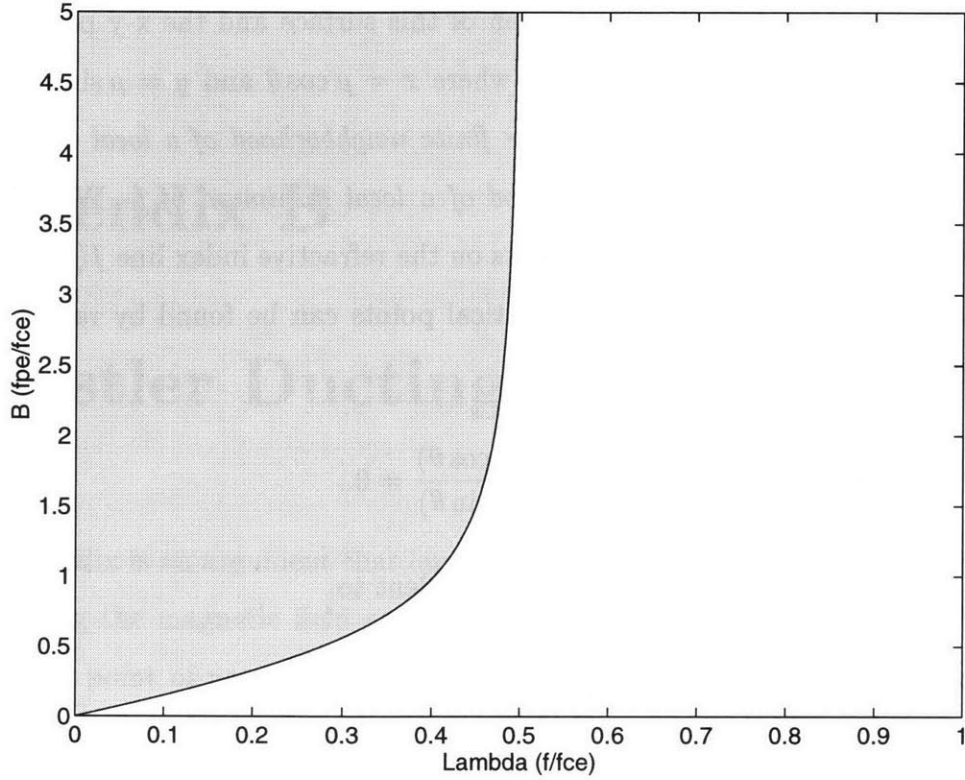


Figure B-1: Region where one solution exists

With this parameterization, we have that

$$\frac{d\mu}{d\theta} = \frac{P \frac{dQ}{d\theta}}{2Q\sqrt{Q^2 - QP}} \quad (\text{B.6})$$

where

$$\frac{dQ}{d\theta} = 2\Lambda^2 \sin \theta \cos \theta \left(\frac{\Lambda^2 \sin^2 \theta - 2(\Lambda^2 - B^2)^2}{\sqrt{\Lambda^4 \sin^4 \theta + 4\Lambda^2 \cos^2 \theta (\Lambda^2 - B^2)^2}} - 1 \right). \quad (\text{B.7})$$

We substitute (B.6) into (B.2) and find the zeros of the numerator. First let us consider solutions for $\theta \neq 0$. Solving (B.2) numerically reveals that there is a maximum of one solution for $0 < \theta < \pi/2$. The region of parameter space where one finds a single solution is shown in fig. B-1. Outside this region, there are zero solutions. It can be shown that solutions for $\theta \neq 0$ approach $\theta = 0$ as one approaches the edge of the shaded region. Thus we can find the equation of the boundary by taking the

limit of (B.2) as θ approaches zero. The result is

$$B^2 = \frac{4\Lambda^3 - 5\Lambda^2 + \Lambda + \sqrt{(-4\Lambda^3 + 5\Lambda^2 - \Lambda)^2 - 4(2\Lambda - 1)(2\Lambda^5 - 4\Lambda^4 + 2\Lambda^3)}}{2(2\Lambda - 1)} \quad (\text{B.8})$$

Since the goal of this analysis was to find if ray optics theory could predict trapped modes above $\Lambda = 0.5$, we will not proceed with the analysis of the critical points represented by the shaded region of figure B-1.

Let us now examine solutions at $\theta = 0$. (B.2) is identically zero, so solutions will exist at all points in parameter space. Let us first check the sign of $\frac{\partial f}{\partial n}$. In terms of P and Q, this derivative is

$$\frac{\partial f}{\partial n} = \frac{P \frac{\partial Q}{\partial n} - Q \frac{\partial P}{\partial n}}{2Q\sqrt{Q^2 - QP}} \cos \theta \quad (\text{B.9})$$

where

$$\frac{\partial P}{\partial n} = \frac{2B^2(\Lambda^2 - 2B^2)}{n} \quad (\text{B.10})$$

$$\frac{\partial Q}{\partial n} = -\frac{2\Lambda^2 B^2}{n} \left(1 + \frac{2 \cos^2 \theta (\Lambda^2 - B^2)}{\sqrt{\Lambda^4 \sin^4 \theta + 4\Lambda^2 \cos^2 \theta (\Lambda^2 - B^2)^2}} \right). \quad (\text{B.11})$$

Since $B > \Lambda$ for the whistler mode, P is negative. Furthermore, the index of refraction is always greater than one, so Q will be positive. Therefore the condition that $\frac{\partial f}{\partial n}$ is greater than zero will be given by

$$P \frac{\partial Q}{\partial n} > Q \frac{\partial P}{\partial n} \quad (\text{B.12})$$

which simplifies to

$$\Lambda < 1. \quad (\text{B.13})$$

This is identically true for all whistler waves, so the task of identifying ducted modes reduces to locating the region within parameter space where maxima occur. However, it is clear that this region is the same region as shown in figure B-1. The reason is that we know that for large enough θ , μ for the whistler mode will become infinitely

large (when Q vanishes). A simple calculation shows that this occurs when

$$\theta = \cos^{-1} \sqrt{\frac{\Lambda^2}{B^2}(1 - \Lambda^2) + \Lambda^2}. \quad (\text{B.14})$$

$f(y)$ therefore approaches an asymptote at this angle of θ . However, figure B-1 revealed exactly how many critical points $f(y)$ passed through before reaching this asymptote. If the number of critical points is zero, then it follows that at $\theta = 0$ there is a minimum. If the number of critical points is one, then at $\theta = 0$ there is a maximum. Thus all points within the shaded region of figure B-1 correspond to locations where the refractive index surface is at a maximum at $\theta = 0$ and will supporting ducting modes. Points outside the region correspond to locations of a refractive index surface minimum where ducting cannot occur due to the sign of $\frac{\partial f}{\partial n}$. Thus for solutions at $\theta = 0$, the ray theory does not predict trapping above $\Lambda = 0.5$.

B.2 Experimental observations

It has been mentioned in earlier chapters that the electron beam-produced plasmas feature whistler emissions, presumably due to bremsstrahlung. These emissions have been observed to have an upper cutoff, although not quite as predicted by figure B-1. The cutoffs are more on the order of 85% of the cyclotron frequency rather than 50% as predicted by the theory. Data are presented by *Rowlands* [1998], shown in figure B-2. *Rowlands* [1998] speculates that the laboratory plasma in which the whistlers are generated has more structure than simply a single “crest”. It is argued that the paths between the beams trajectories can play host to so-called “trough” ducting, a mechanism which works up to the cyclotron frequency [*Helliwell*, 1965].

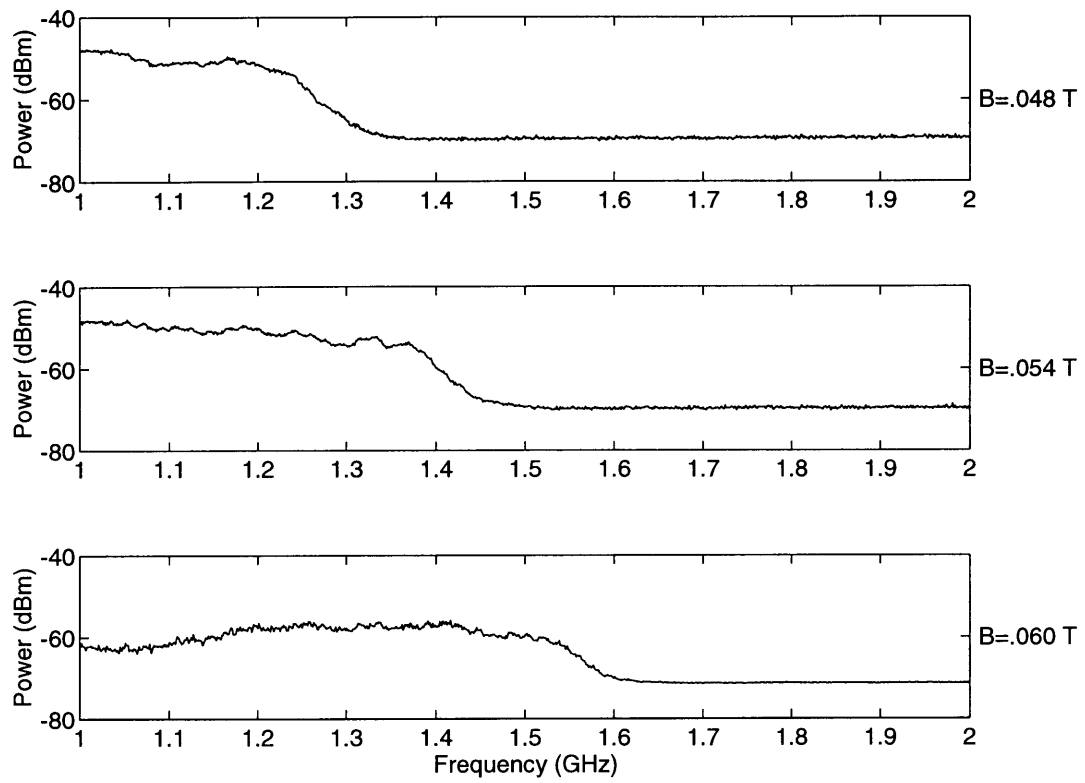


Figure B-2: Probe observations of whistler wave cutoff in the VTF machine.

Bibliography

- [1] H. Ahmed and A. N. Broers. Lanthanum hexaboride electron emitter. *Journal of Applied Physics*, 43:2185, 1972.
- [2] S. N. Antani and D. J. Kaup. Whistler scattering from density fluctuations in magnetized plasmas. *Physics of Fluids*, 27:1169, 1984.
- [3] K. G. Balmain. The impedance of a short dipole antenna in a magnetoplasma. *IEEE Transactions on Antennas and Propagation*, AP-12:605, 1964.
- [4] K. G. Balmain. Dipole admittance for magnetoplasma diagnostics. *IEEE Transactions on Antennas and Propagation*, AP-17:389, 1969.
- [5] J. F. Bamber, W. Gekelman, and J. E. Maggs. Whistler wave mode conversion to lower hybrid waves at a density striation. *Physical Review Letters*, 73:2990, 1994.
- [6] J. M. Beall, Y. C. Kim, and E. J. Powers. Estimation of wavenumber and frequency spectra using fixed probe pairs. *Journal of Applied Physics*, 53:3933, 1982.
- [7] T. F. Bell, H. G. James, U. S. Inan, and J. P. Katsufraakis. The apparent spectral broadening of VLF transmitter signals during transionospheric propagation. *Journal of Geophysical Research*, 88:4813, 1983.
- [8] T. F. Bell and H. D. Ngo. Electrostatic waves stimulated by coherent VLF signals propagating in and near the inner radiation belt. *Journal of Geophysical Research*, 93:2599, 1988.

- [9] T. F. Bell and H. D. Ngo. Electrostatic lower hybrid waves excited by electromagnetic whistler mode waves scattering from planar magnetic-field-aligned plasma density irregularities. *Journal of Geophysical Research*, 95:149, 1990.
- [10] P. M. Bellan and M. Porkolab. Experimental studies of lower hybrid wave propagation. *The Physics of Fluids*, 19:995, 1976.
- [11] B. Bhat and B. R. Rao. Experimental investigations on the impedance behavior of a cylindrical antenna in a collisional magnetoplasma. *IEEE Transactions on Antennas and Propagation*, AP-21:70, 1973.
- [12] M. Bitter, C. Hollenstein, P. J. Paris, and C. Rizzo. A cross-power spectrum analyzer. Internal report 80, Centre de Recherches en Physique des Plasmas, Ecole Polytechnique Federale de Lausanne, 1977.
- [13] K. G. Budden. *The propagation of radio waves: The theory of radio waves of low power in the ionosphere and magnetosphere*. Cambridge University Press, Cambridge, 1985.
- [14] R. P. H. Chang and M. Porkolab. Backward-scattering instability of cyclotron harmonic waves in nonlinear decay processes. *The Physics of Fluids*, 13:2766, 1970.
- [15] F. F. Chen. *Introduction to Plasma Physics and Controlled Fusion*, volume 1. Plenum, New York, second edition, 1984.
- [16] V. M. Chmyrev, M. M. Mogilevsky, O. A. Molchanov, Y. P. Sobolev, E. E. Titova, T. A. Yakhina, R. N. Suncheleev, V. A. Gladyshev, N. V. Baranets, N. V. Dzhordzhio, Y. I. Galperin, and A. V. Streltsov. Parametric excitation of ELF waves and acceleration of ions during the injection of strong VLF waves into the ionosphere. *Soviet Physics Space Research*, 27:249, 1989.
- [17] V. M. Chmyrev, V. K. Roldugin, I. A. Zhulin, M. M. Mogilevskii, V. I. Di, V. K. Koshelevskii, V. A. Bushmarin, and O. M. Raspopov. Artificial injection of very

- low frequency (VLF) waves into the ionosphere and the magnetosphere of the earth. *JETP letters*, 23:409, 1976.
- [18] Y. R. Dalkir, M. C. Lee, K. M. Groves, and S. P. Kuo. A mechanism responsible for the observation of symmetric lower hybrid sidebands and a low frequency mode in the upper ionosphere. *Journal of Geophysical Research*, 97:17195, 1992.
- [19] B. G. Fejer and M. C. Kelley. Ionospheric irregularities. *Review of Geophysics*, 18:401, 1980.
- [20] D. W. Forslund, J. M. Kindel, and E. L. Lindman. Parametric excitation of electromagnetic waves. *Physical Review Letters*, 29:249, 1972.
- [21] K. M. Groves. *Nonlinear ionospheric propagation effects on UHF and VLF radio signals*. Ph.D. dissertation, Massachusetts Institute of Technology, 1991.
- [22] K. M. Groves, M. C. Lee, and S. P. Kuo. Spectral broadening of VLF radio signals traversing the ionosphere. *Journal of Geophysical Research*, 93:14683, 1988.
- [23] R. A. Helliwell. *Whistlers and Related Ionospheric Phenomena*. Stanford University Press, Stanford, 1965.
- [24] I. H. Hutchinson. *Principles of Plasma Diagnostics*. Cambridge University Press, Cambridge, 1987.
- [25] D. B. Illić and K. J. Harker. Evaluation of plasma-wave spectral density from cross-power spectra. *The Review of Scientific Instruments*, 46:1197, 1975.
- [26] S. M. Kay and S. L. Marple. Spectrum analysis—a modern perspective. *Proceedings of the IEEE*, 69:1380, 1981.
- [27] S. P. Kuo and M. C. Lee. Stimulated scattering instability of lower hybrid waves. *The Physics of Fluids*, 29:1024, 1986.

- [28] S. P. Kuo and M. C. Lee. A source mechanism producing HF-induced plasma lines (HFPLs) with up-shifted frequencies. *Geophysical Research Letters*, 19:249, 1992.
- [29] M. C. Lee and S. P. Kuo. Production of lower hybrid waves and field-aligned plasma density striations by whistlers. *Journal of Geophysical Research*, 89:10873, 1984.
- [30] M. C. Lee, R. J. Riddolls, and D. T. Moriarty. Laboratory study of some lightning-induced effects in the ionospheric plasma. *Journal of Atmospheric and Solar-Terrestrial Physics*, 60:965, 1998.
- [31] M. C. Lee, R. J. Riddolls, K. D. Vilece, N. E. Dalrymple, M. J. Rowlands, D. T. Moriarty, K. M. Groves, M. P. Sulzer, and S. P. Kuo. Laboratory reproduction of Arecibo experimental results: HF wave-enhanced Langmuir waves. *Geophysical Research Letters*, 24:115, 1997.
- [32] S. J. Levinson, S. B. Kim, T. Koh, and E. J. Powers. Plasma fluctuation diagnostics via maximum entropy spectral estimation. *The Review of Scientific Instruments*, 59:1754, 1988.
- [33] D. J. McEwen and R. E. Barrington. Some characteristics of the lower hybrid resonance noise bands observed by the Alouette I satellite. *Canadian Journal of Physics*, 45:13, 1967.
- [34] M. L. Meade. *Lock-in amplifiers: principles and applications*. P. Peregrinus, London, 1983.
- [35] S. L. Meredith. Construction of a gridded energy analyzer for measurements of ion energy distribution in the Versatile Toroidal Facility. M.S. thesis, Massachusetts Institute of Technology, 1998.
- [36] D. T. Moriarty. *Laboratory Studies of Ionospheric Plasma Processes with the Versatile Toroidal Facility (VTF)*. Sc.D. dissertation, Massachusetts Institute of Technology, 1996.

- [37] S. L. Ossakow and P. K. Chaturvedi. Current convective instability in the diffuse aurora. *Geophysical Research Letters*, 6:332, 1979.
- [38] J. P. Perotti. Notes sur la realisation d'un cross-correlateur. Internal report 85, Centre de Recherches en Physique des Plasmas, Ecole Polytechnique Federale de Lausanne, 1977. In French.
- [39] M. Porkolab. Parametric instabilities in a magnetic field and possible applications to heating of plasmas. *Nuclear Fusion*, 12:329, 1972.
- [40] R. J. Riddolls. Measurements of plasma wave propagation direction. Report for 6.100 Independent Laboratory, Department of Electrical Engineering and Computer Science, Massachusetts Institute of Technology, 1997.
- [41] R. J. Riddolls. Whistler ducting. Internal report, Plasma Science and Fusion Center, Massachusetts Institute of Technology, 1997.
- [42] D. Riggin and M. C. Kelley. The possible production of lower hybrid parametric instabilities by VLF ground transmitters and by natural emissions. *Journal of Geophysical Research*, 87:2545, 1982.
- [43] J. R. Roth. Paired comparison tests of the relative signal detected by capacitive and floating Langmuir probes in turbulent plasma from 0.2 to 10 MHz. *The Review of Scientific Instruments*, 42:589, 1971.
- [44] M. J. Rowlands. Electromagnetic wave propagation in a magnetized laboratory plasma. M.Eng. thesis, Massachusetts Institute of Technology, 1998.
- [45] R. L. Smith. Propagation characteristics of whistlers trapped in field-aligned columns of enhanced radiation. *Journal of Geophysical Research*, 66:3699, 1961.
- [46] V. I. Sotnikov, V. Fiala, F. Lefevre, and D. Lagoutte. Excitation of sidebands due to non-linear coupling between a VLF transmitter signal and a natural ELF emission. *Journal of Geophysical Research*, 96:11363, 1991.

- [47] J. C. Sprott. High frequency representation of a plasma sheath. Internal report 61, Thermonuclear Plasma Studies, University of Wisconsin, 1966.
- [48] D. H. Staelin, A. W. Morgenthaler, and J. A. Kong. *Electromagnetic Waves*. Prentice Hall, Englewood Cliffs, New Jersey, 1994.
- [49] T. H. Stix. *Waves in Plasmas*. American Institute of Physics, New York, 1992.
- [50] Y. Tanaka, D. Lagoutte, H. Hayakawa, F. Lefeuvre, and S. Tajima. Spectral broadening of VLF transmitter signal and sideband structure observed on AUREOL-3 satellite at middle latitudes. *Journal of Geophysical Research*, 92:7551, 1987.
- [51] S. Torvén, H. Gunell, and N. Brenning. A high frequency probe for absolute measurements of electric fields in plasmas. *Journal of Physics D: Applied Physics*, 28:595, 1995.
- [52] K. D. Vilece. Experimental study of anti-Stokes Langmuir modes and particle precipitation produced by RF heating of ionospheric plasmas. M.S. thesis, Massachusetts Institute of Technology, 1992.
- [53] E. S. Weibel. Measurement of the cross correlation function of two signals. Internal report 63, Centre de Recherches en Physique des Plasmas, Ecole Polytechnique Federale de Lausanne, 1975.
- [54] E. D. Zimmerman and S. C. Luckhardt. Measurement of the correlation spectrum of electrostatic potential fluctuations in an ECRH helimak plasma. *Journal of Fusion Energy*, 12:289, 1993.